REPORT DOCUMENTATION PAGE

Form Approved
OMB NO. 0704-0188

1. AGENCY USE ONLY (Leave Blank)	2. REPORT DATE	3. REPORT TYPE AND DATES COVERED
	August 30, 2003	Final report 6/1/1999-5/31/2003

4. TITLE AND SUBTITLE
Final Report: Quantum coherent electron-phonon nanolaboratories

5. FUNDING NUMBERS
DAAD19-99-1-0226

6. AUTHOR(S)
Dr. A.N. Cleland

7. PERFORMING ORGANIZATION NAME(S) AND ADDRESS(ES)
Regent s of the University of California
Office of Research
UC Santa Barbara Santa Barbara CA 93106

8. PERFORMING ORGANIZATION REPORT NUMBER

9. SPONSORING / MONITORING AGENCY NAME(S) AND ADDRESS(ES)
U. S. Army Research Office
P.O. Box 12211
Research Triangle Park, NC 27709-2211

10. SPONSORING / MONITORING AGENCY REPORT NUMBER
39998.1-PH

11. SUPPLEMENTARY NOTES
The views, opinions and/or findings contained in this report are those of the author(s) and should not be construed as an official Department of the Army position, policy or decision, unless so designated by other documentation.

12 a. DISTRIBUTION / AVAILABILITY STATEMENT
Approved for public release; distribution unlimited.

12 b. DISTRIBUTION CODE

13. ABSTRACT (Maximum 200 words)
This project was aimed at creating mechanically suspended nanostructures that include active electronic devices, with the goal of achieving coherence between electrons and vibrational phonons. We pursued separately the use of metal tunnel junctions (SIS tunnel junctions and single-electron transistors, SETs), and electrostatically defined double quantum dots, as the electronic system. We performed cryogenic measurements with varying degrees of success. Due to unanticipated difficulties, the focus shifted direction several times. Our most successful implementation was the use of an SET coupled to the vibrational motion of a doubly-clamped 100 MHz flexural resonator, with which we achieved a displacement sensitivity roughly 100 times the quantum limit of motion. A ten times higher frequency resonator, at 1 GHz, could be detected at 10 times the quantum limit. We believe further improvement in the sensitivity and noise of the displacement sensor is possible. Other areas of research, such as using double-quantum dots, did not prove as illuminating or useful; direct, resonant coupling as observed by dc current-voltage measurements did not reveal the hoped-for signatures of resonant coupling. There are a number of reasons as to why this may be, and further work might further elucidate the physics.

14. SUBJECT TERMS
Suspended nanostructures; superconducting tunnel junctions; lateral quantum dots

15. NUMBER OF PAGES
85

16. PRICE CODE

17. SECURITY CLASSIFICATION OR REPORT	18. SECURITY CLASSIFICATION ON THIS PAGE	19. SECURITY CLASSIFICATION OF ABSTRACT	20. LIMITATION OF ABSTRACT
UNCLASSIFIED	**UNCLASSIFIED**	**UNCLASSIFIED**	**UL**

Final Report

Quantum Coherent Electron-Phonon Nanolaboratories

Dr. A. N. Cleland
Department of Physics
UC Santa Barbara
Santa Barbara CA 93106

Table of Contents

Summary

Statement of problem studied

This research effort was a multi-pronged effort to develop integrated nanomechanical and nanoelectronic devices, to explore what new types of physics could be investigated using the integrated devices. The main goal was to create a coupling between the electronic and the mechanical degrees of freedom (phonons), that could be detected either by its effect on the dc transport properties of the electronic device, or by direct detection at the resonant frequency of the mechanical structure.

Our efforts were therefore directed at a number of different areas: fabrication of mechanical devices using materials with strong piezoelectric effects (GaAs and AlN); fabrication of electronic devices with potentially strong coupling to phonons, either through the piezoelectric effect or through deformation potential coupling (quantum dots and Josephson junctions), and fabrication of electronic devices with strong coupling to the charge (single electron transistors, SETs). The various electronic devices were integrated in a number of different ways with mechanically suspended structures. In addition to the experimental effort, we also spent some effort developing theoretical models and approaches for understanding and predicting some of the behavior in these types of structures.

Summary of important results

Over the course of this project we have developed a large number of experimental and theoretical concepts in a number of different areas. We have developed two major materials systems for applications in nanomechanical/nanoelectronic systems (AlN and GaAs). We have implemented a number of electronic devices integrated with nanomechanical structures (quantum point contacts, quantum single and double dot structures, Josephson tunnel junctions, single electron transistors). We have developed and measured the phonon conductance and electron phonon coupling using a variety of SIN tunnel junction structures, both at quasi-dc and at radio frequencies, the latter allowing us to probe the time dynamics of the electron-phonon coupling. We have theoretically developed concepts relating to phononic band gaps analogous to photonic band gaps, an architecture for coupling Josephson phase qubits with nanomechanical resonators for phase-coherent communication and phase state storage, and a piezoelectric coupling scheme for SETs coupled to a piezoelectric beam of GaAs.

Significant accomplishments included the development of a quantum-point contact displacement sensor, demonstrated at 4.2 K but in principle operable at room temperature; quasi-dc and radiofrequency thermometry allowing us to measure the static and dynamic temperature in a mechanically suspended structure, as well as the phonon conductance through highly transmissive supporting beams.

One of the more notable successes was in strongly coupling a SET to a doubly clamped mechanical resonator, with detection through the capacitive coupling of the resonator to

the gate of the SET. With this approach, we were able to detect displacements of the resonator with as small as 23 fm amplitude, and the displacement noise we achieved was about $2x10^{-15}$ m/$Hz^{1/2}$, only a factor of 100 above the quantum noise limit for that beam, with a resonance frequency of 116 MHz. A 1 GHz beam would have a bit more than three times the displacement noise and therefore its quantum noise would be only roughly one-twentieth that of our displacement detector. This result was published in the journal *Nature*, and had significant impact in the media, with articles in the New York Times and various on-line technical newsletters. The future direction for this work would be to attempt the same measurement with a higher frequency resonator, improve the coupling to reduce the effect of the noise, and to then attempt squeezing both in the thermal and quantum regimes.

Overall under this program we published one *Nature* article, six *Applied Physics Letters*, one *Physical Review B* brief communication, one *Journal of Applied Physics* article, and have one manuscript submitted to *Phys. Rev. Lett.* In addition we have one manuscript in preparation for *Phys. Rev. Lett.*, and two in preparation for *Phys. Rev. B.*

We now turn to a summary of the various areas we worked on over this program. I will only describe the more interesting areas of development; I have attached copies of all the publications and manuscripts, which can be referred to for more information about areas not discussed, and of course for more detail on the areas that are described here.

Materials development

We focused here on two materials systems, aluminum nitride (AlN) and gallium arsenide (GaAs).

Aluminum nitride resonators

AlN is an interesting material because it has a strong piezoelectric coefficient and is also quite stiff and quite light, making it an ideal material for high frequency mechanical resonators. The strong piezoelectric coefficient makes it potentially useful for coupling to electronic devices through the induced polarization when a mechanical element is under strain.

Experimentally, we investigated the use of single-crystal AlN as a resonator material; this work was published as "Single-crystal aluminum nitride nanomechanical resonators", A.N. Cleland, M. Pophristic and I. Ferguson, *Appl. Phys. Lett.* **79**, 2070 (2001). The AlN was grown by MOCVD on single crystal silicon, a simple materials system that lends itself well to nanofabrication using fairly standard techniques. AlN can be grown *c*-axis oriented on <111> oriented Si, without too many defects (most of the defects are threading dislocations due to the lattice mismatch). We grew 0.17 μm thick films on bulk (350 μm thick) Si wafers. These were then patterned using a single layer of electron beam lithography: A pattern of wire bond pads and single wire (Au) electrodes were patterned in PMMA, and a metal trilayer of Ti adhesion (3 nm thick), a 35 nm Au film, and a 60 nm Ni film; the Ni served as an etch mask for the anisotropic reactive ion etch of the AlN. Beam lengths ranged from 3.6 to 5.9 μm, with 0.2 μm widths. The ends of the beams were defined by a step increase in the width to 2.4 μm. The electrode pattern was transferred to the AlN film using anisotropic Cl_2 based reactive ion etching (RIE). The AlN etch rate was approximately 150 nm/min, with very vertical sidewalls. The etch rate for the Si substrate and the Ni mask was negligible in these conditions.

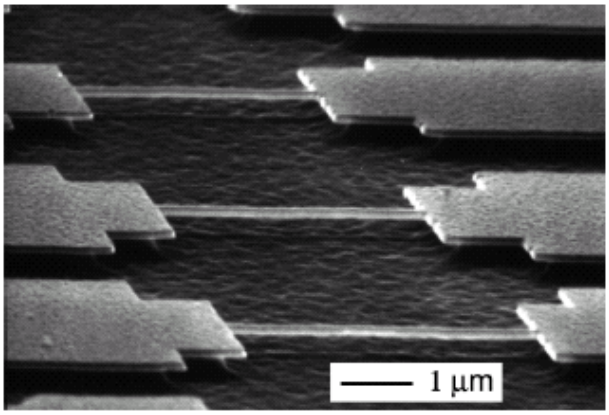

Figure 1. Series of four AlN beams, with the undercut lengths ranging from 3.9 to 5.6 μm. The beams are 0.17 μm thick, and the widths are 0.2 μm, increasing to widths of 2.4 μm at either end.

The Ni was then removed using a commercial Ni etchant, and the structures released by etching the Si substrate with an isotropic wet etchant. A 15 second etch was sufficient to mechanically free the resonators; the structures were rinsed in methanol, and dried in air. An electron micrograph of a set of completed beams is shown in Figure 1.

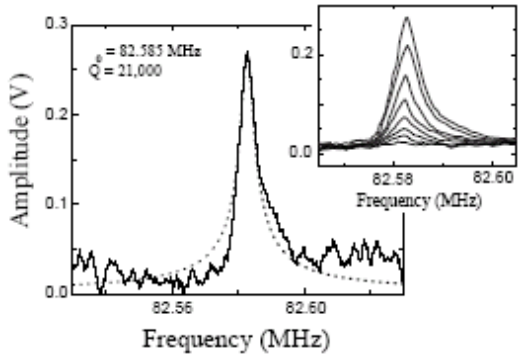

Figure 2. Measured resonance of a 3.9 μm long beam, measured at 4.2 K in a transverse magnetic field of 8 T. Applied rf power was -85 dBm. *Inset:* Measured resonance for a constant rf power of -75 dBm, while varying the magnetic field through integer values from 1 T (smallest peak) to 8 T (largest peak).

Electrical contacts to the completed resonators were made with Au wire bonds, and the structures were placed in a vacuum can, which was evacuated and then submerged in liquid helium, in the bore of an 8 Tesla magnet. The resonators were oriented with the plane of the sample parallel to the magnetic field, allowing a magnetomotive measurement of the beam resonance frequency and quality factor. A typical measurement is shown in for a 3.3 μm long beam, displaying a clear resonance at 82 MHz with a quality factor $Q = 2.1 \times 10^4$. Varying the magnetic field for a fixed rf drive power shows the expected quadratic dependence on magnetic field, shown inset in the figure.

These resonators can be made with resonance frequencies in the range from a few MHz up to well over 1 GHz. Displacement was measured using the magnetomotive technique, as described above. However, the strong piezoelectric signal affords the possibility of sensing motion using a polarization sensitive device, such as a field effect transistor, a quantum point contact or a SET.

Gallium Arsenide resonators

We have fabricated a number of quite different structures from GaAs, ranging from simple beams, to beams with integrated quantum point contacts and double quantum dots. The latter structures included, in a heterostructure, a two-dimensional electron gas that was etched and suspended along with the underlying and overlying GaAs, such as shown in Figure 3. These structures were fabricated with a combination of optical and electron beam lithography, metal deposition and Ohmic contact annealing, and anisotropic etch mask definition followed by etch.

The structure was etched from a single-crystal GaAs heterostructure grown by molecular beam epitaxy, comprising a bulk <100> GaAs wafer, 700 nm of $Al_{0.7}Ga_{0.3}As$ (the sacrificial layer), 600 nm of GaAs, 40 nm of $Al_{0.3}Ga_{0.7}As$, a Si delta-doped layer, 70 nm of $Al_{0.3}Ga_{0.7}As$, and a 10 nm GaAs capping layer. The suspended mechanical structure includes all layers above the sacrificial layer (see below). The two-dimensional electron gas (2DEG) in which the QPC or quantum dot is formed is at the lower GaAs-$Al_{0.3}Ga_{0.7}As$ interface, where similar samples had a carrier density of $1.4 \times 10^{15}/m^2$, and a

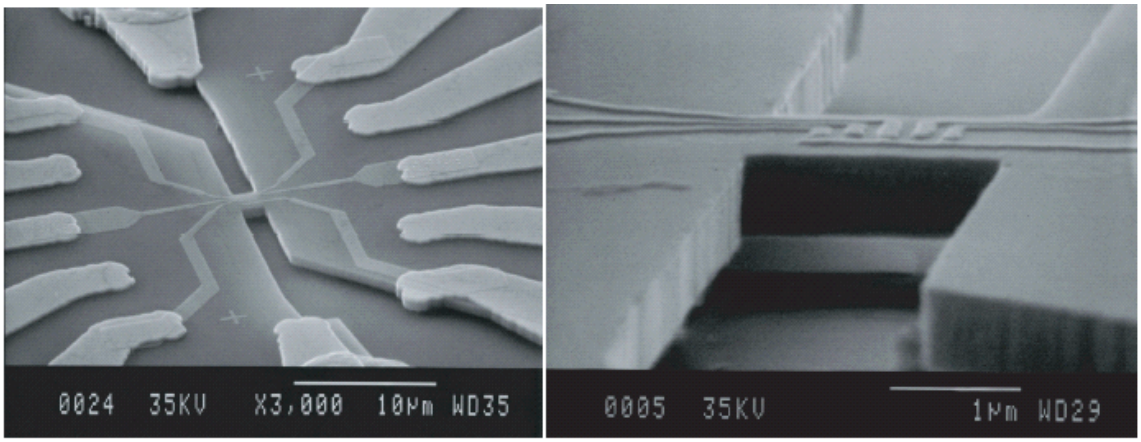

Figure 3. Double quantum dots patterned in a mechanically suspended GaAs beam resonator. Left shows large-scale view with bond pads, right shows close up of suspended section.

mobility of 40 m^2/V-s at 4.2 K. In our device, the 2DEG mobility was significantly degraded by processing.

We used photolithography to define a set of NiAuGe ohmic contacts to the 2DEG. Next electron-beam lithography was used to define Ti/Au (5 nm/40 nm) electrodes for the top gates, as well as for actuation of the mechanical structure. A second photolithography step defined Ti/Au (5 nm/110 nm) wire-bond pads to make contact with the metal electrodes and ohmic contacts. A second electron beam lithography step then defined the structural masking layer. The unmasked area of the heterostructure was etched using $SiCl_4$-based reactive ion etching, etching to a depth of about 800 nm, almost through the sacrificial layer. The sacrificial layer was then etched using a timed submersion in concentrated hydrochloric acid, followed by a 10% solution of hydrofluoric acid. This resulted in a structure with a suspended thickness of 0.72 μm.

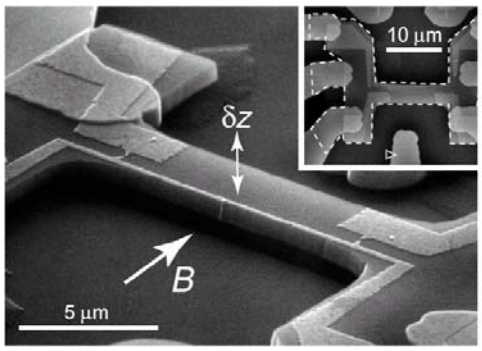

Figure 4. SEM micrograph of the QPC electrodes defined on the surface of a suspended beam. The magnetic field is used for magnetomotive actuation is indicated, as is the direction of flexure Δz. *Inset:* Larger scale image of the structure, with the dotted line outlining the suspended area.

Resonator frequencies similar to those for the AlN resonators are easily achieved. In addition we hoped to observe thickness (dilatational) resonances in the quantum dot structures shown in Figure 3, but were not successful in that attempt (see below). We were successful in coupling a QPC to a resonator's piezoelectric signal, where the flexural motion of the resonator would modulate the QPC conductance. This approach is nominally capable of achieving the quantum limit of detection. This work was published as "Nanomechanical displacement sensing using a

quantum point contact", A.N. Cleland, J.S. Aldridge, D.C. Driscoll and A.C. Gossard, *Appl. Phys. Lett.* **81**, 1699 (2002).

In Figure 4 we show a successful QPC integrated with a 10 MHz mechanical resonator; the entire structure in the dotted outline is suspended. QPC's can be formed at either end of the resonator by applying negative voltages to the appropriate top-surface electrodes.

One difficulty is that a QPC cannot easily be used to read out at high frequencies, due to its intrinsic high electrical resistance. We therefore employed the QPC as a mixer, using the nonlinearity of the intrinsically fast device to mix the output signal down to acoustic frequencies with a local oscillator signal. In Figure 5 we show the circuit schematic used to accomplish this, along with a series of resonance curves for the response of the QPC when the beam was driven using the magnetomotive effect.

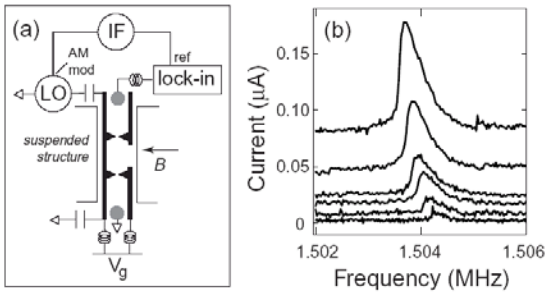

Figure 5. (a) Measurement schematic for electrostatic drive and detection using the QPC. The LO drive signal is capacitively coupled to electrode 1, and is amplitude modulated at the IF frequency of 13.7 Hz. The QPC current is lock-in detected with the IF signal as a reference. (b) IF current through the QPC for a range of applied LO powers. The remnant magnetic field is estimated from magnetomotive measurements to be less than 0.01 T.

We can estimate the displacement sensitivity of the QPC from our measurements; using the magnetomotive reflectance measurements, we can calculate the midpoint displacement Δz of the structure, and from the corresponding magnitude of the IF current, we find the responsivity of about 28 Δz nA/μm. Our current detection is limited by the voltage noise in the IF preamplifier, and corresponds to a noise of 3×10^{-12} m/Hz$^{1/2}$, better than what is achieved with optical interferometry. The corresponding force noise is about 0.3 nN/Hz$^{1/2}$. The sensitivity improves with reduction in size scale, due to the increase in strain for a given displacement. Our device geometry allows for significantly smaller structures, with correspondingly higher frequencies, potentially approaching 1 GHz. The delicate sensitivity of the QPC can therefore potentially be employed as a quantum-limited displacement sensor, and allow the entanglement of a phase-coherent electron transmission sensor with a mechanical resonator.

Strongly coupled electronic devices

We worked on a number of different approaches to achieve strong coupling between electrons and phonons in these systems. Our approaches included superconductor-insulator-superconductor (SIS) Josephson junctions, superconductor-insulator-normal metal (SIN) tunnel junctions, quantum point contacts, single- and double-quantum dots, and single electron transistors (SETs). We used a number of different diagnostics to try and observe electron-phonon coupling and thereby quantify the coupling. The main two

approaches were to look for effects in dc transport, such as features due to opening a new channel for energy loss, or understanding the detailed behavior in terms of thermal transport between the electron and phonon systems, and measuring effects at radio frequencies, using the electronic device as a direct detector of a signal from a high *Q* mechanical resonator vibrating on resonance.

Quantum point contacts.
We described the quantum point contact experiment above, in the section on GaAs materials-based resonators. This work was published as "Nanomechanical displacement sensing using a quantum point contact", A.N. Cleland, J.S. Aldridge, D.C. Driscoll and A.C. Gossard, *Appl. Phys. Lett.* **81**, 1699 (2002)

Single-electron transistor coupled to resonator
This experiment was developed in stages. We first had to determine how to extract radio frequency signals from the SET, with frequencies up to 1 GHz. This was accomplished by developing a technique for using the SET as a mixer, driven by a local oscillator provided by an external RF signal. Our first implementation of this allowed us to demonstrate mixing to 300 MHz (R.G. Knobel, C.S. Yung and A.N. Cleland, *Appl. Phys. Lett.* **81**, 532 (2002)); later implementations worked to well above 700 MHz.

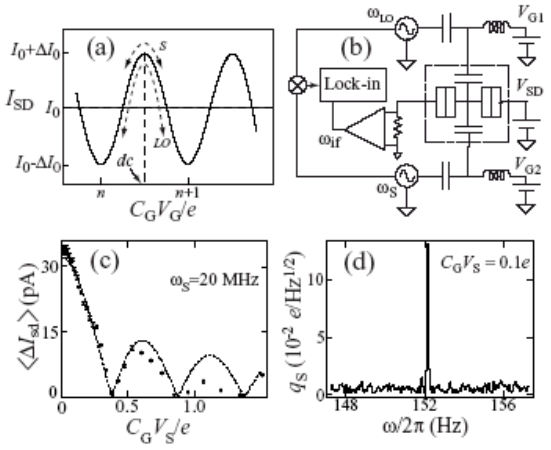

Figure 6. (a) Schematic diagram for mixing. The gate charge is set for maximum current (dashed vertical line), and a signal and (for heterodyne mixing) local oscillator voltage are coupled to the gate. (b) Mixing circuit schematic for both homodyne and heterodyne mixing. The SET is in the dashed box in the center. (c) Homodyne detector signal at dc, measured as a function of signal voltage. The signal at 20 MHz was applied to gate 2, while the SET was in the superconducting state. Points are experimental data, the dashed line is the expected Bessel function response. (d) Heterodyne mixing spectral density about 152.15 Hz, with the SET in the normal state. Vertical axis is in units of input signal charge spectral density.

For this experiment, we used a lithographically patterned SET, comprising two Al/AlOx/Al tunnel junctions and two interdigitated coupling capacitors, fabricated using electron beam lithography and shadow evaporation. The device was fabricated on a GaAs heterostructure, to allow for in-situ fabrication of nanomechanical structures.

The device was mounted on a dilution refrigerator and cooled to 30 mK. All leads were filtered with metal powder filters and source and drain leads with RC filters at 1.5 K and at room temperature. The SET was operated as a mixer both in the superconducting state, and in the normal state, in a magnetic field of 1 Tesla. The relatively large value

of the SET resistance limited the noise performance and output bandwidth.

The homodyne response is shown in Figure 6(c) for gate 2 at 20 MHz. A fit to the expected dependence is also shown; the zeroes in the response allow us to calibrate the signal voltage. The non-zero capacitance between the gate and source-drain leads can rf-modulate the source-drain voltage as well.

For heterodyne mixing, the signal voltage is applied to one gate, and a local oscillator voltage is applied to the other gate. The source-drain current is modulated by both signals, and a current generated at the intermediate (difference) frequency. The IF signal (magnitude and phase) was detected using a lock-in amplifier, whose reference signal was generated by a separate mixer, shown in Figure 6(b). High-pass filters ensured that this reference signal was not transmitted to the SET. The measured spectral response is shown in Figure 6(d), showing the peak at the IF frequency as well as the sideband noise.

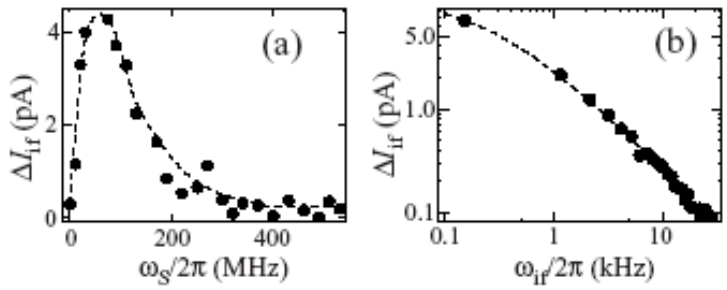

Figure 7. (a) Mixing signal amplitude as a function of LO frequency at constant IF frequency; the signal and LO powers were -68 dBm and -61 dBm respectively. The low frequency rolloff is due to high-pass filtering, and the high frequency rolloff due to the device limitation. The dashed line is a guide to the eye. (b) Mixing signal as a function of IF frequency for an LO frequency of 50 MHz. The dashed line is a fit giving a -3 dB single-side bandwidth of 250 Hz.

We also measured the heterodyne mixer amplitude as the dc source-drain voltage and dc gate voltage are varied. The *e* periodicity in C_gV_g is observed, and the dependence on V_{SD} has the expected maximum near $e/2C$. The gain of the device is tunable by varying the dc gate bias, source-drain voltage, and oscillator power. The IF response was calculated using an analytic model for the SET, and the measured response follows the predicted behavior, but is approximately a factor of 2 smaller than calculated. At present we do not understand this discrepancy.

Figure 7 shows the frequency dependence of the mixer signal, for fixed IF and constant LO and signal power. The figure shows a measurable signal up to 300 MHz, limited by the cutoff frequency for this device. Figure 7(b) shows the 250 Hz output bandwidth for the SET. This bandwidth can be increased by lowering the junction resistance, operating in the superconducting state, or reducing the cable capacitance. Use of a closely coupled preamplifier or tuned *LC* circuit could further increase the output bandwidth. Noise measurements near the intermediate frequency at optimum gain yield

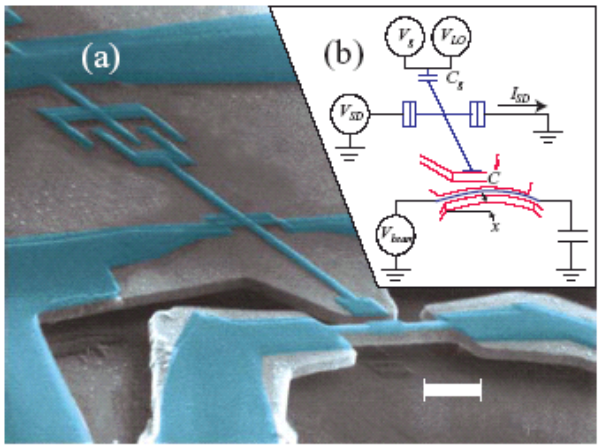

Figure 8. The device used in the experiment. (a) Scanning electron micrograph of the device, showing the doubly-clamped GaAs beam, and the aluminum electrodes (colorized) forming the single electron transistor and beam electrode. The scale bar is 1 μm long. The Al/AlOx/Al tunnel junctions have approximately 50x50 nm^2 overlap. The inset (b) shows a schematic of the operation of the device.

a signal charge sensitivity of 4×10^{-3} $e/\mathrm{Hz}^{1/2}$, limited by noise in the room-temperature electronics.

Developing this mixer system then allowed us to employ the SET as a displacement sensor for a radiofrequency mechanical resonator. It has been a long-standing goal to detect the effects of quantum mechanics on a macroscopic mechanical oscillator. Position measurements of an oscillator are ultimately limited by quantum mechanics, where ``zero-point motion'' fluctuations in the quantum ground state combine with the uncertainty relation to yield a lower limit on the measured average displacement. Developing a position transducer, integrated with a mechanical resonator, which can approach this limit would have important applications in the detection of very weak forces, for example in magnetic resonance force microscopy as well as in a variety of other precision experiments. One implementation that might allow near quantum-limited sensitivity is to use a single electron transistor (SET) as a displacement sensor. In this technique, the exquisite charge sensitivity of the SET at cryogenic temperatures is exploited to measure motion by capacitively coupling it to the mechanical resonator. We achieved the first experimental realization of such a device, yielding an unequalled displacement sensitivity of 2×10^{-15} m/Hz$^{1/2}$ for a 116 MHz mechanical oscillator at a temperature of 30 mK, a sensitivity roughly a factor of 100 larger than the quantum limit for this oscillator.

Our device consists of a 3 μm long x 250 nm wide x 200 nm thick doubly-clamped beam of single-crystal GaAs, capacitively coupled to an aluminum SET, located 250 nm from the beam. The beam was patterned using electron beam lithography and etched from a GaAs heterostructure using a sequence of reactive ion etching and dilute HF wet etching. The SET was formed through double-angle shadow evaporation, using a pattern defined in a second step of electron-beam lithography. The device was mounted on a dilution refrigerator and cooled to 30 mK. All electrical leads were filtered. An out-of-plane 8 T magnetic field was applied to drive the aluminum out of the superconducting state, and to provide a field for actuation and sensing of the beam motion.

The beam was driven using the magnetomotive technique, in which an alternating current through the beam electrode, along its length in the presence of the magnetic

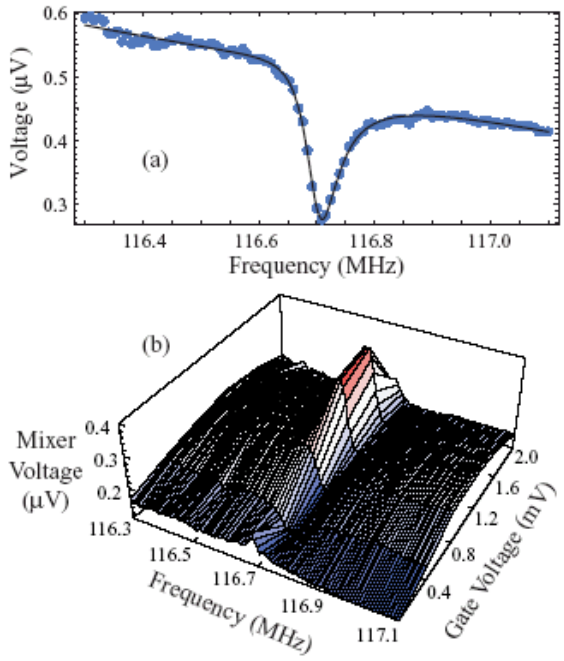

Figure 9. Single electron transistor measurement of the beam motion. (a) Intermediate frequency voltage (SET mixer output) as a function of beam drive frequency, for P = -125 dBm drive power. The solid line is a fit to a Lorentzian plus linear background with arbitrary phase. The beam electrode had a dc voltage of 5 V, the LO power was -70 dBm, and the IF was 151 Hz. The SET gate voltage was tuned to give maximum signal. (b) IF voltage for P = -115 dBm drive power, as a function of dc gate voltage and drive frequency. The slowly varying background interferes with the resonance signal, whose phase varies with the gate voltage.

field, generates a Lorentz force. We measured the induced electromotive force (EMF) developed along the beam due to its resulting motion through the magnetic field by measuring the reflected and transmitted power. The beam vibrates in its fundamental in-plane mode with a resonant frequency of 116.7 MHz. The measured EMF fits well to a Lorentzian function with a quality factor of 1700. The beam displacement is related to the EMF. We thus determine the displacement as a function of power, yielding the resonator mass m = 2.84 x 10^{-15} kg and effective spring constant k = 1530 N/m. The device is shown in Figure 8.

Figure 9 (a) shows the mixer signal for a drive power of -125 dBm. Using the magnetomotive calibration, this corresponds to an extrapolated amplitude of 2.3x10^{-14} m on resonance. The charge detected by the SET is due to the change in coupling capacitance times the beam voltage, as well as secondary signals due to the induced EMF, and capacitively coupled charge due to cable resonances and ohmic losses. The former is very small compared to the direct signal (less than 1%), and the second varies slowly with frequency. Thus the total signal detected by the SET has the form of a Lorentzian, plus a background with an arbitrary phase.

The quality factor Q and resonant frequency obtained using the SET were the same as those from the magnetomotive technique, and the amplitude varied as $P^{1/2}$. The SET response is found to be 9.9 V/μm, proportional to the displacement, when the SET is biased optimally, with a LO frequency offset from the beam drive signal by 151 Hz. As the SET gate voltage is varied from the optimum value, the sensitivity decreases and interference with the background becomes more pronounced. The resonant signal decreases linearly with magnetic field, and increases linearly with beam voltage.

The detector noise is about 100 times larger than the thermal noise of the measured beam, and about a factor of 20 larger than the quantum noise in a 1 GHz resonator with

Q=10^4. By using improved electronics and impedance matching, the second-stage noise could be reduced by roughly a factor of ten, and better lithography could reduce the SET-beam separation, increasing the SET response. A higher quality factor would yield larger signals in both the thermal and quantum limits; experimentally the Q is observed to reduce as the resonators are made smaller, at least partly due to surface damage and contamination. Flash heating of resonators in vacuum has been demonstrated to yield significantly higher quality factors, a technique that could be applied here. The expected increase in displacement sensitivity using a combination of these techniques could, in a second-generation device, allow measurement in the quantum-limited regime.

Hence we have demonstrated an ultrasensitive, potentially quantum-limited displacement sensor based on a single-electron transistor, enabling us to read out the motion of a nanomechanical resonant beam at its resonant frequency. The device has a displacement sensitivity of 2.0x10^{-15} m/$Hz^{1/2}$ at the 116.7 MHz resonant frequency of the mechanical beam, limited by the noise in the conventional electronics.

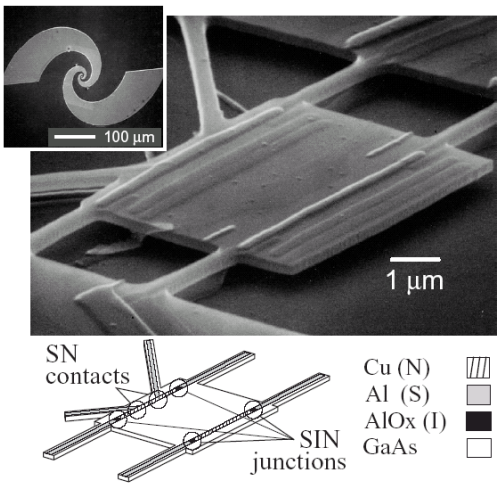

Figure 10. Micrograph of suspended structure, with 1 μm scale bar. Top left: Log spiral antenna for coupling radiation to the device. Bottom: Schematic of device, indicating the GaAs suspended island, the six supporting legs, the SIN tunnel junctions and the ohmic SN contacts.

SIN thermometric tunnel junctions

One important question relates to the coupling strength between electrons and phonons in a mechanically suspended structure. We therefore pursued a number of measurements to try and quantify this coupling, using primarily normal metal-insulator-superconductor (NIS) tunnel junctions, with which the temperature of the electrons can be determined from the zero-bias conductance. We therefore have built a number of structures that allow us to heat the electrons and the phonons, and from thermal measurements extract the coupling.

The primary experiment was published as "Thermal conductance and electron-phonon coupling in mechanically suspended nanostructures", C.S. Yung, D.R. Schmidt and A.N. Cleland, *Appl. Phys. Lett.* **81**, 31 (2002). A more recent experiment showed how to implement the thermometer at radio frequencies, published as "Nanoscale radio-frequency thermometry", D.R. Schmidt, C.S. Yung and A.N. Cleland, *Appl. Phys. Lett.* **83**, 1002 (2003). We have since completed an experiment where the electron-phonon coupling could be measured in a dynamic fashion, allowing us to watch in time domain as a pulse energy dissipated from the electrons into the phonons with few-nanosecond time scale. This work is submitted to

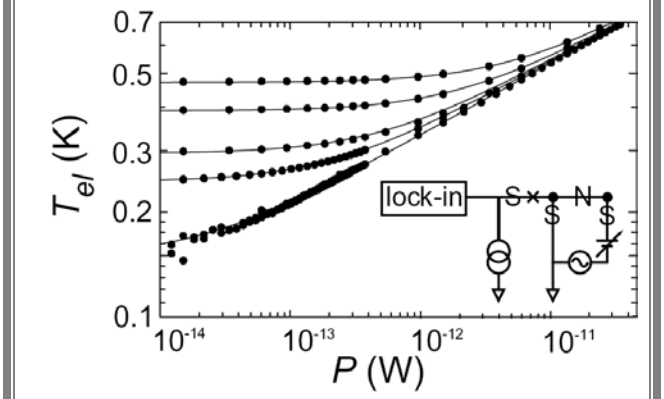

Figure 11. Electron temperature measured as a function of power dissipated in the normal metal, measured at 0.025 K, 0.24 K, 0.3 K, 0.4 K, and 0.5 K (indicated by the intercept). The 0.025 K data intercepts T_{el} at 0.15 K; solid lines are fits to the data. Inset is a diagram of the measurement setup.

Phys. Rev. Lett., "Direct temporal measurement of hot-electron relaxation in a phonon-cooled metal island", D.R. Schmidt and A.N. Cleland.

We demonstrated the integration of SIN tunnel junctions with a nanoscale suspended single-crystal GaAs structure, allowing us to measure the electron-phonon coupling in a normal metal film on the suspended structure, as well as measure the phonon thermal conductance through the supporting legs. Our device can be applied to e.g. infrared bolometry.

The device was fabricated from a GaAs/AlGaAs heterostructure consisting of a 200 nm GaAs top layer and a 400 nm $Al_{0.7}Ga_{0.3}As$ sacrificial layer, on a bulk GaAs substrate. The lateral dimensions of the mechanical structure were defined using electron-beam lithography to pattern an etch mask, used for a timed anisotropic reactive ion etch of the GaAs heterostructure. We used $SiCl_4$ to etch to a depth of 400 nm. The structure is shown in Figure 10; the six supporting legs are 0.2x0.2x0.3 μm^3, and the central GaAs island is 0.2x5x6 μm^3. The AlGaAs layer was removed with a timed wet, undercutting the island and six legs. The tunnel junction circuit was defined on the surface of the suspended structure, using a second step of electron-beam lithography to create a stencil mask for angled shadow evaporation. These included a pair of SIN tunnel junctions connected back-to-back in a SINIS pair configuration, and a separate SINIS pair with two ohmic superconductor-normal metal (SN) contacts to the center normal metal element. Only (superconducting) Al was deposited on the support legs, minimizing the thermal conductance. The tunnel junctions can be used as SINIS junction pairs, or, using the SN contacts, as single SNIS junctions.

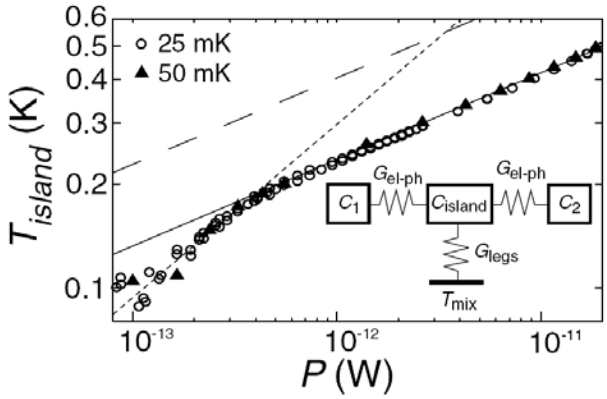

Figure 12. Island temperature as a function of power dissipated in the island phonon gas, measured at 25 mK (circles) and 50 mK (triangles). Solid line is a fit to the data, yielding a phonon mean free path of 7.7 μm. The long dash line is for a 1 μm mean free path for comparison. The quantum of thermal conductance is indicated by the short dashed line.

We measured the electron-phonon coupling by passing a dc current through the two SN contacts, heating the normal metal, and monitoring the electron temperature T_{el} using one of the SNIS junctions. The SIN junction, located 5 μm from the dc injection point, is ac biased to allow a lock-in measurement of the zero-bias conductance, extracting the electron temperature. Negligible measurement power was dissipated. Figure 12 shows T_{el} as a function of power, for different mixing chamber temperatures. The solid lines are fits to the standard bulk hot electron form, in agreement with previous measurements. Measurements at other temperatures yield similar fits and fit parameters. Calculations of the acoustic mismatch between the Cu and the GaAs phonon gases predict a reduced fit value for the power law. However, the applicability of acoustic mismatch theory is debatable, as the phonon modes in the Cu film are effectively two dimensional below 1 K. Note that we identify the island phonon temperature with the mixing chamber temperature.

The thermal conductance of the support legs was measured by dc biasing one of the SINIS pairs, and measuring the corresponding rise in phonon temperature using an electrically isolated SNIS junction. The heating power deposited in the normal Cu section (C_1) of the first SINIS pair heats the island phonon gas, and is then transmitted through the legs to the bulk substrate. The phonon temperature is inferred from the electron temperature of the normal Cu section (C_2) of the SNIS thermometer, using the previously determined electron-phonon coupling. The measured thermal conductance is shown in , for mixing chamber temperatures of 25 mK and 50 mK. The solid line is a fit to the data of the form expected for bulk thermal conductance. This corresponds to a mean free path of 7.7 μm, indicating that the phonons undergo primarily specular (rather than diffuse) reflections within the legs. Also plotted (short dashes) is the quantum of thermal conductance for six legs. The data agrees well with the bulk theory, crossing over to the quantum limit at approximately 170 mK. Note the large phonon mean free path in our device masks the transition to the quantum limit; we have also plotted the bulk thermal conductance for a 1 μm mean free path (long dashes), which would make the transition to the quantum limit at 550 mK. In addition, the thermal conductance of the legs is significantly larger than the electron-phonon effective conductance, so the assumption that the phonon temperature is equal to the dilution refrigerator temperature in the electron-phonon heating measurements is a good one.

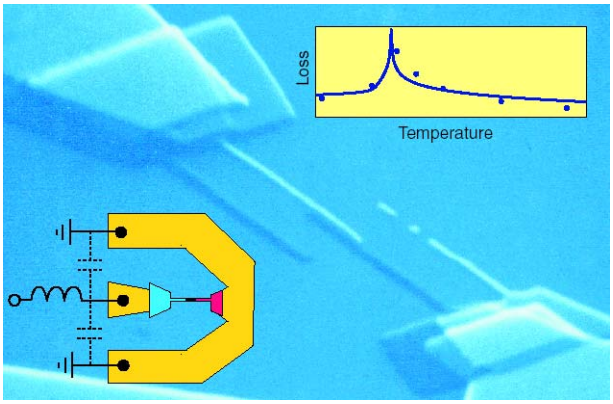

Figure 13. rf-SIN thermometer. *Background:* SEM image of SIN tunnel junction. *Left inset:* Electrical circuit used to readout thermometer, with a tuned *LC* circuit impedance matching the junction to the 50 Ω readout cabling. *Right inset:* Reflected power loss, with a peak as a function of temperature when perfect impedance matching occurs.

We have also succeeded in demonstrating how to read out these thermometers at high frequencies: The SIN thermometer is ultimately limited by its intrinsic *RC* time constant to about 10 GHz, and we have successfully developed circuitry allowing the readout of these intrinsically high resistance devices at frequencies up to about 300 MHz, with 1 GHz a trivial extension of this demonstration. The image shown in Figure 13 captures the essence of the concept, an image that was published on the cover of the corresponding issue of *APL*, "Nanoscale radio-frequency thermometry", D.R. Schmidt, C.S. Yung and A.N. Cleland, *Appl. Phys. Lett.* **83**, 1002 (2003).
The basic concept is to embed the SIN junction in a tuned *LC* circuit, the junction serving to determine the reflected power from the circuit driven on resonance. The reflected power loss is plotted in the upper right, showing increasing loss as the SIN resistance approaches the optimal (impedance-matched) resistance as a function of temperature.

The *LC* circuit is designed to resonate at between 0.1-1 GHz, and the effective *Q* (determined be the ratio of the characteristic $(L/C)^{1/2}$ impedance to the cable 50 Ω impedance) determined the bandwidth of the reflected power measurement, and is typically of order $1/10^{th}$ the resonance frequency, or between 10-100 MHz. The measured loss allows determination of the junction resistance, and from a measurement (or calculation based on BCS theory) of the temperature dependence of the zero-bias resistance, the temperature can be extracted.

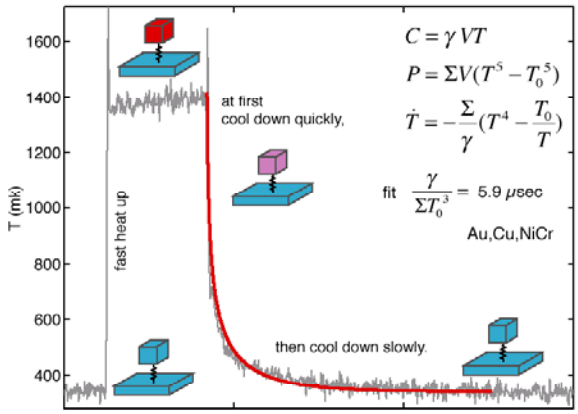

Figure 14. Dynamic measurement of electron-phonon coupling, showing heating and cooling cycle of electron gas in a small metal island at 300 mK. Red line is fit of dynamic theory to data, allowing us to fit the electron-phonon rate of 6 μsec, corresponding to a time constant of 1.2 μsec.

We have since used this new technique to make the first measurement of the dynamic electron-phonon coupling in a metal island, extracting temperature as a function of time as the electrons emit phonons. Data are shown in Figure 16.This allowed us to measure the heat capacity of the metal island, with a result that agreed with the small volume of metal of about 1 fJ/K. Extending the lithographic techniques to smaller structures should allow us to demonstrate a heat capacity of only 10 k_B, equivalent to only 10 degrees of freedom in a classical system, which should allow us to measure the heat capacity of just a small number of e.g. spins in a metal. This work has been submitted for review (D.R. Schmidt, C.S. Yung, A.N. Cleland, *submitted to Phys. Rev. Lett.* (2003)).

Theoretical treatments

Phonon bandstructure calculation

One interesting area is whether the phonon dispersion curves in a mechanically suspended structure can be controlled in order to enhance or reduce the transport of phonons. This is of interest if one wishes to "trap" phonons in a small volume. We therefore completed a model calculation where we replaced a simple insulating beam, the basis for calculating the quantum of thermal conductance, by a beam made from an artificial one-dimensional phononic crystal. We found that at the lowest temperatures, and longest thermal phonon wavelengths, the quantum limit of thermal conductance is recovered, while for intermediate temperatures, where the dominant phonon wavelength is of the order of the phononic crystal repeat distance, a significant suppression of the conductance is predicted. At higher temperatures the conductance returns to that of a simple beam. This work was published as "Thermal conductance of nanostructured phononic crystals", A.N. Cleland, D.R. Schmidt and C.S. Yung, *Phys. Rev. B* **64**, 172301 (2001).

Periodically modulated mechanical structures, which generate classical band structures, have been used for some time for applications in ultrasound and ultrasonic transducers; a description of the current theoretical and experimental work appears in a review by Kushwaha. The dispersion relation for acoustic phonons traveling in a periodically modulated material is found to develop gaps in the transmission spectrum at wavevectors associated with the modulation wavevector; these gaps should have an effect on the thermal conductance of a beam fabricated from such a material.

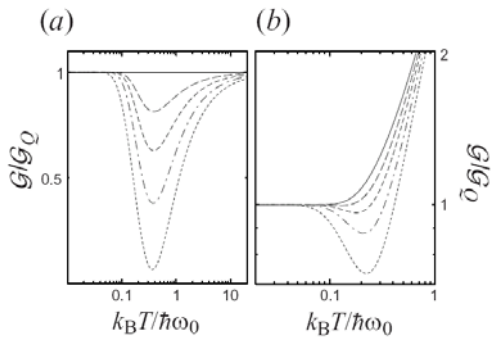

Figure 15. a) Calculated thermal conductance in units of the quantum of thermal conductance, for one mode of a phononic crystal beam, as a function of temperature normalized to the bandgap center. The solid line is for a simple beam, showing the quantum value G_Q = 1, and the dotted lines are for phononic crystal beams with bandgap widths of 0.2, 0.4, 0.6 and 1. (b) Thermal conductance including the higher order modes, for the simple beam (solid line) and for the same series of modulation.

We have calculated the dispersion relations for a periodically modulated, quasi one-dimensional beam, using two different acoustic models. We find that the resulting band structure, with gaps at frequencies that correspond to the phonons dominant at quite low temperatures, yields significant reductions in the thermal conductance from the quantum limit G_Q at moderate temperatures. However, the presence of delocalized Bloch states at the lowest phonon frequencies, below the gap, gives a thermal conductance that approaches G_Q at the lowest temperatures.

One model we used was for the longitudinal acoustic mode in a beam of variable cross-section. This structure is shown in Figure 16. Another model we used involved varying the density and elastic constants of a material in a similar fashion. The outcome of these types of structures, in terms of the effect on phonon

transport and phonon conductance, can be represented by the resulting thermal conductance as a function of temperature. We assume the beam is adiabatically coupled to thermal reservoirs at either end, using smooth, graduated increases in the cross-sectional area to the bulk solid; we therefore avoid end-to-end phonon resonances, and the acoustic mismatch from abrupt area transitions. We calculate the temperature dependence of the thermal conductance for a single low frequency Bloch mode, with transmissivity equal to one for frequencies in the allowed bands, and zero in the forbidden gap region. The result of the calculation is shown in Figure 15(a), calculated for temperatures well below the cut-off temperature for the second mode. In part (b) of that figure we display the temperature dependence including the higher order modes.

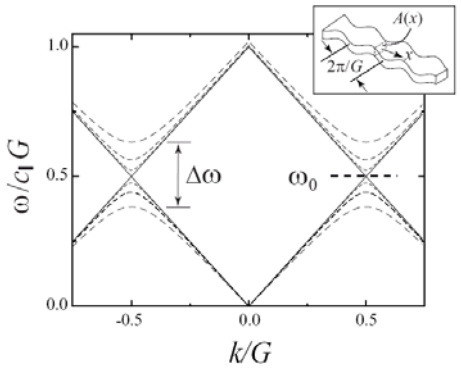

Figure 16. Calculated dispersion relation for modulation strengths 0, 0.1, 0.25 and 0.5 in the longitudinal acoustic model. The gap for is indicated, as is the bandgap center frequency. Eleven bands were included in the calculation, the lowest two are shown here.

Applications to quantum computation

Building on the work of coupling the SET to a high-frequency flexural resonator, we have also developed a quantum computation scheme in which phase qubits are coupled to mechanical resonators, the former used for actual computation, and the latter as memory and quantum state transfer elements.

We have prepared a manuscript that is being submitted to *Phys. Rev. Lett.* as "Quantum information processing with nanomechanical resonators", A.N. Cleland and M.R. Geller. The quantum-information-processing architecture is based on the integration of ultrahigh-frequency nanomechanical resonators with Josephson-junction-based qubit circuits, which can be used to implement the single- and multi-qubit operations critical to quantum computation. The qubits are eigenstates of large-area, current-biased Josephson junctions, manipulated and measured using strobed external circuitry. Two or more of these ``phase qubits" are coupled to a high-quality-factor piezoelectric mechanical resonator, which forms the backbone of our architecture, enabling coherent manipulation of the

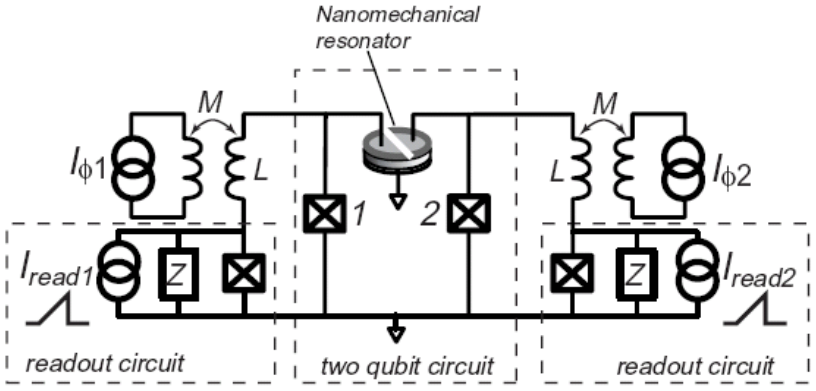

Figure 17. Proposed architecture for achieving two-qubit entanglement with the use of a nanomechanical resonator. The qubits are the two Josephson junctions, coupled to a resonator, shown as a disc with a split gate

qubits. The integrated system is analogous to one or more few-level atoms (the Josephson junction qubits) in a tunable electromagnetic cavity (the nanomechanical resonator).

Our implementation uses large-area current-biased Josephson junctions, with capacitance C and critical current I_0; a circuit model is shown in Figure 17. The nanomechanical resonator is designed with a fundamental thickness resonance frequency between 1 - 10 GHz, with a quality factor Q of 10^5 – 10^6. Piezoelectric dilatational resonators with thickness resonance frequencies in this range, and quality factors of order of 10^3 at room temperature, have been fabricated from sputtered AlN. Single-crystal AlN can also be grown by chemical vapor deposition. Our simulations are based on such a resonator, with a diameter and thickness of 1x0.5 μm^2. Such resonators can be used to coherently store a qubit state prepared in a current-biased Josephson junction, return it to that junction, or transfer it to another junction, as well as entangle two or more junctions. These operations are performed by tuning the energy level spacing of the qubit state into resonance with the resonator quantum levels, generating electromechanical Rabi oscillations. The full Hamiltonian for the system is equivalent to that of a few-level atom in an electromagnetic cavity. The cavity ``photons'' here are phonons, which interact with the ``atoms'' (here the Josephson junctions) via the piezoelectric effect. This analogy will allow us to adapt quantum-information processing protocols developed for cavity-QED to our solid-state architecture.

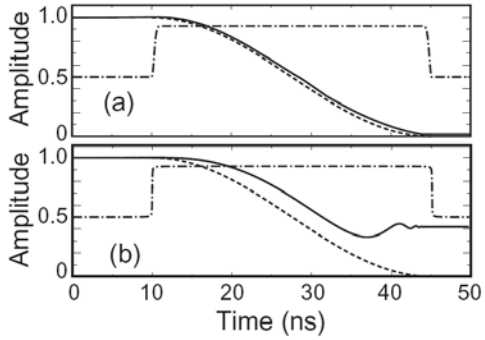

Figure 18. (a) Phase qubit storage. Solid curve is $|c_{10}(t)|^2$, dashed curve is analytic RWA calculation, dash-dotted curve is bias current s(t). (b) Qubit storage with arctangent bias-current profile. All other parameters are the same as in (a). Solid curve is numerical result.

We first show that we can coherently transfer a qubit state from a junction to a resonator, simulating this process by numerically integrating the exact amplitude equations. The Josephson junction had a Josephson coupling energy E_J = 43.05 meV and charging energy E_c = 53.33 neV. Our main result is shown in Figure 18. The qubit transfer depends sensitively on the shape of the bias current profile $s(t) = I(t)/I_0$, which starts at s=0.50, and is then adiabatically changed to the resonant value s=0.928. We find that the time during which s changes should be at least exponentially localized. Therefore one must bring the system into resonance as quickly as possible without violating adiabaticity. The power-law tails associated with an arctangent function, for example, lead to deviations from the desired behavior, shown in Figure 18(b). The result in Figure 18(a) was obtained using Gaussian profiles with a cross-over time of 1 ns. All quasibound states were included in the calculation, and convergence with the resonator's Hilbert space dimension was obtained. The junction is held in resonance for

half a Rabi period, during which energy is exchanged at the Rabi frequency. The systems are then brought out of resonance.

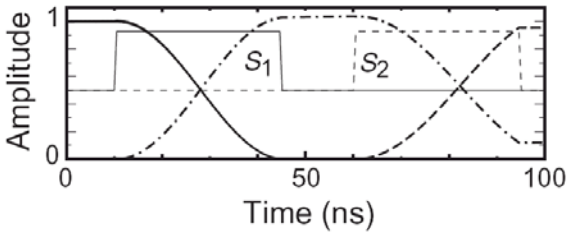

Figure 19. Qubit transfer between two junctions. Solid curve is $|c_{100}(t)|^2$, dashed-dotted curve is $|c_{001}(t)|^2$, dashed curve is $|c_{010}(t)|^2$. Thin solid and dotted curves show $s_1(t)$ and $s_2(t)$, the bias currents through junctions 1 and 2.

To pass a qubit state a|0>+b|1> from junction 1 to junction 2, the state is loaded into the first junction and the bias current changed to bring the junction into resonance with the resonator for half a Rabi period. This writes the state a|0> +b|1>into the resonator. After the first junction is taken out of resonance, the second junction is brought into resonance for half a Rabi period, passing the state to the second junction. We have simulated this operation numerically, assuming two identical junctions coupled to the resonator described above. The results are shown in Figure 19, where $c_{m1\ m2\ n}$ is the probability amplitude (in the interaction representation) to find the system in the state |m1 m1 n >, with m1 and m2 labeling the states of the two junctions. We can prepare an entangled state of two junctions by bringing the first junction into resonance with the resonator for 1/4 of a Rabi period, which, according to our RWA analysis, produces the state $(|100> - |001>)/2^{1/2}$. After bringing the second junction into resonance for a half of a Rabi period, the state of the resonator and second junction are swapped, leaving the system in the state $(|100> - |010>)/2^{1/2}$ with a probability of 0.987, where the resonator is in the ground state and the junctions are entangled. Using the cavity-QED analogy, it will be possible to transfer the methodology developed for the standard two-qubit operations, in particular controlled-NOT logic, to the electromechanical system, using mostly existing technology and demonstrated techniques.

Publications

Peer reviewed journals

R.G. Knobel and A.N. Cleland, “Nanometre-scale displacement sensing using a single electron transistor”, *Nature* **424**, 291 (2003)

D.R. Schmidt, C.S. Yung and A.N. Cleland, “Nanoscale radio-frequency thermometry”, *Appl. Phys. Lett.* **83**, 1002 (2003)

A.N. Cleland, J.S. Aldridge, D.C. Driscoll and A.C. Gossard, “Nanomechanical displacement sensing using a quantum point contact”, *Appl. Phys. Lett.* **81**, 1699 (2002)

R.G. Knobel, C.S. Yung and A.N. Cleland, “Single-electron transistor as a radio-frequency mixer”, *Appl. Phys. Lett.* **81**, 532 (2002)

C.S. Yung, D.R. Schmidt and A.N. Cleland, “Thermal conductance and electron-phonon coupling in mechanically suspended nanostructures”, *Appl. Phys. Lett.* **81**, 31 (2002)

R. Knobel and A.N. Cleland, “Piezoelectric displacement sensing with a single-electron transistor”, *Appl. Phys. Lett.* **81**, 2258 (2002)

A.N. Cleland and M.L. Roukes, “Noise processes in nanomechanical resonators”, *J. Appl. Phys.* **92**, 2758 (2002)

A.N. Cleland, D.R. Schmidt and C.S. Yung, “Thermal conductance of nanostructured phononic crystals”, *Phys. Rev. B* **64**, 172301 (2001)

A.N. Cleland, M. Pophristic and I. Ferguson, “Single-crystal aluminum nitride nanomechanical resonators”, *Appl. Phys. Lett.* **79**, 2070 (2001)

Conference proceedings (refereed)

J.S. Aldridge, R.S. Knobel, D.R. Schmidt, C.S. Yung and A.N. Cleland, “Nanoelectronic and Nanomechanical Systems”, *SPIE Proceedings* **4591**,11 (2001)

Submitted for publication

D.R. Schmidt and A.N. Cleland, “Direct temporal measurement of hot-electron relaxation in a phonon-cooled metal island”, *submitted to Phys. Rev. Lett.*

A.N. Cleland and M.R. Geller, “Quantum information processing with nanomechanical resonators”, *submitted to Phys. Rev. Lett.*

In manuscript form

M.R. Geller and A.N. Cleland, “Electron-Phonon Coupling in Reduced Dimensional Structures”, *to be submitted to Phys. Rev. B*

J.S. Aldridge, D.C. Driscoll, A.C. Gossard and A.N. Cleland, “Mechanically suspended quantum dot structures”, *to be submitted to Phys. Rev. B*

Personnel

These are personnel supported in whole or in part over the course of this program.

Dr. A.N Cleland (PI)

Dr. R.G. Knobel (now faculty at Queen's University, Kingston, Ontario Canada)

Dr. D. R. Schmidt (accepted a position as a visiting scientist at JILA, CU Boulder)

Christopher Yung

J. Sequoyah Aldridge

Report of Inventions

None

Appendix. Reprints and preprints of publications and manuscripts

23. Passey, Q. R. & Melosh, H. J. Effects of atmospheric breakup on crater field formation. *Icarus* **42,** 211–233 (1980).
24. Melosh, H. J. *Impact Cratering: A Geological Process* (Oxford Univ. Press, Oxford, 1989).
25. Schmidt, R. M. & Housen, K. R. Some recent advances in the scaling of impact and explosion cratering. *Int. J. Impact Eng.* **5,** 543–560 (1987).
26. Ivanov, B. A., *et al.* in *Chronology and Evolution of Mars* (ed. Kallenbach, R.) 87–104 (Kluwer, Dordrecht, 2001).
27. Hartmann, W. K. Martian cratering VI: Crater count isochrons and evidence for recent volcanism from Mars Global Surveyor. *Meteorit. Planet. Sci.* **34,** 167–177 (1999).
28. Bland, P. A. *et al.* The flux of meteorites to the Earth over the last 50,000 years. *Mon. Not. R. Astron. Soc.* **283,** 551–565 (1996).

Acknowledgements We thank B. Ivanov, W. Hartmann and P. Brown for providing cratering data, flux data, and for discussions, and B. Ivanov, H. J. Melosh, V. Shuvalov, J. Morgan, B. Pierazzo and M. Gounelle for suggestions that improved earlier drafts of this manuscript. This work benefited greatly from comments and suggestions from C. Chapman. N.A. thanks RFBR for support, and P.A.B. thanks the Royal Society for support.

Competing interests statement The authors declare that they have no competing financial interests.

Correspondence and requests for materials should be addressed to P.A.B. (p.a.bland@imperial.ac.uk).

Nanometre-scale displacement sensing using a single electron transistor

Robert G. Knobel*† & Andrew N. Cleland*

* *Department of Physics and iQUEST, University of California, Santa Barbara, California 93106, USA*

It has been a long-standing goal to detect the effects of quantum mechanics on a macroscopic mechanical oscillator[1–3]. Position measurements of an oscillator are ultimately limited by quantum mechanics, where 'zero-point motion' fluctuations in the quantum ground state combine with the uncertainty relation to yield a lower limit on the measured average displacement. Development of a position transducer, integrated with a mechanical resonator, that can approach this limit could have important applications in the detection of very weak forces, for example in magnetic resonance force microscopy[4] and a variety of other precision experiments[5–7]. One implementation that might allow near quantum-limited sensitivity is to use a single electron transistor (SET) as a displacement sensor[8–11]: the exquisite charge sensitivity of the SET at cryogenic temperatures is exploited to measure motion by capacitively coupling it to the mechanical resonator. Here we present the experimental realization of such a device, yielding an unequalled displacement sensitivity of 2×10^{-15} m Hz$^{-1/2}$ for a 116-MHz mechanical oscillator at a temperature of 30 mK—a sensitivity roughly a factor of 100 larger than the quantum limit for this oscillator.

A classical simple harmonic oscillator, in equilibrium with its environment at temperature T, will have an average total energy $k_B T$. The position of the oscillator fluctuates continuously, with a root mean square displacement amplitude $\delta x = (k_B T/m\omega_0^2)^{1/2}$ for an oscillator of mass m and resonant frequency $f_0 = \omega_0/2\pi$. This classical displacement amplitude can be made arbitrarily small by reducing the temperature. One implication of quantum mechanics, however, is that the quantized nature of the oscillator energy yields an intrinsic fluctuation amplitude, the 'zero-point motion' $\delta x_{zp} = (\hbar/2m\omega_0)^{1/2}$. This is achieved for temperatures T well below the energy quantum, $T \ll T_Q \equiv \hbar\omega_0/k_B$. A second implication of quantum mechanics is that the instrument used to measure the position of the oscillator will necessarily perturb it, further limiting the possible measurement resolution, as quantified by the Heisenberg uncertainty principle. A continuous measurement of the average position of an oscillator, using a quantum-limited amplifier, is thus limited to $\sqrt{2}$ times the zero-point motion, or $\delta x_{meas} \geq (\hbar/m\omega_0)^{1/2}$. We note that 'back-action evading' techniques have in principle unlimited measurement precision, although these yield less information and are still subject to zero-point fluctuations if the measurement is slower than the oscillator relaxation time[1,12].

A 1-GHz nanomechanical flexural resonator was recently demonstrated[13]. This resonator would have $T_Q = 50$ mK, so when operated on a dilution refrigerator at 10 mK, the inequality $T \ll T_Q$ could be reached. A resonator with similar dimensions would be a candidate for detecting the transition from classical to quantum noise, because the small mass gives a relatively large zero-point displacement noise, $\delta x_{zp} \approx 2 \times 10^{-14}$ m. In terms of the spectral displacement noise density, this corresponds to $S_x^{1/2} = 5 \times 10^{-18}$ m Hz$^{-1/2}$ on resonance, fairly small due to the relatively low quality factor $Q \approx 500$. Techniques to measure the displacement of large-scale resonators, such as optical interferometry or electrical parametric transducers[1,14,15], can achieve better displacement noise limits than this, but the larger mass of the resonator makes reaching the quantum limit more difficult. Such techniques do not scale well to nanomechanical resonators, and other techniques more applicable to these size scales[16,17] are unlikely to approach quantum-limited sensitivity. The single electron transistor provides a possible system in which sufficient sensitivity can be achieved.

The single-electron transistor (SET) consists of a conducting island separated from leads by low-capacitance, high-resistance tunnel junctions. The current through the SET is modulated by the charge induced on its gate electrode, with a period e, the charge of one electron. The SET is the most sensitive electrometer[18,19], with a demonstrated sensitivity below $10^{-5}\ e\,\mathrm{Hz}^{-1/2}$. The motion of a nanomechanical resonator may be detected by capacitively coupling the gate of the SET to a metal electrode placed on the resonator, and biasing the electrode at a constant voltage V_{beam} (see Fig. 1). The capacitance C between the SET and the beam then has a coupled charge $q = V_{beam}C$. As the beam vibrates in the x direction, in the

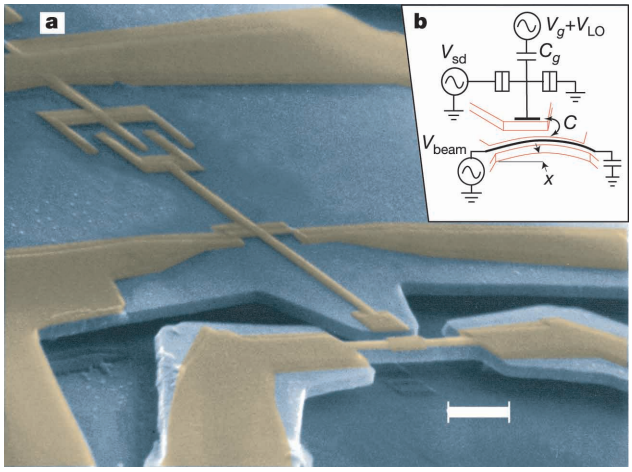

Figure 1 The device used in the experiment. **a**, Scanning electron micrograph of the device, showing the doubly clamped GaAs beam, and the aluminum electrodes (coloured) forming the single electron transistor and beam electrode. Scale bar, 1 μm. The Al/AlO_x/Al tunnel junctions have approximately 50×50 nm^2 overlap. **b**, A schematic of the mechanical and electrical operation of the device.

† Present address: Department of Physics, Queen's University, Kingston, Ontario K7L 3N6, Canada.

plane of the device, the resulting variation in capacitance ΔC will modulate the charge induced on the SET, $\Delta q = V_{\rm beam}\Delta C$, changing the SET source–drain current. As the voltage $V_{\rm beam}$ is increased, the charge modulation Δq and the sensitivity to the resonator motion will increase. However, the source-drain current is due to the stochastic flow of electrons through the SET, so the centre island's voltage fluctuates randomly. This causes a fluctuating 'back-action' force on the beam. This force increases as $V_{\rm beam}$ increases, resulting in a voltage for which the total noise is minimized. The displacement sensitivity at this optimal voltage is calculated[9,10] to be of order $10^{-16}\,{\rm m\,Hz^{-1/2}}$, approaching the sensitivity needed to measure quantum effects.

Our device (Fig. 1) consists of a 3 μm long × 250 nm wide × 200 nm thick doubly-clamped beam of single-crystal GaAs, capacitively coupled to an aluminum SET, located 250 nm from the beam. The beam was patterned using electron beam lithography and etched from a GaAs heterostructure using a sequence of reactive ion etching and dilute HF wet etching[20]. The SET was formed through double-angle shadow evaporation, using a pattern defined in a second step of electron-beam lithography[21,22]. The device was mounted on a dilution refrigerator and cooled to 30 mK. All electrical leads were filtered[23]. An out-of-plane 8 T magnetic field was applied to drive the aluminum out of the superconducting state, and to provide a field for actuation and sensing of the beam motion.

The beam was driven using the magnetomotive technique, in which an alternating current I through the beam electrode, along its length L in the presence of the magnetic field B, generates a Lorentz force $F = IlB$. We measured the induced electromotive force (EMF) $\mathscr{E}$ developed along the beam owing to its resulting motion through the magnetic field[16,24,25] by measuring the reflected and transmitted power. The beam vibrates in its fundamental in-plane mode with a resonant frequency $f_0 = 116.7$ MHz (see Fig. 2). The measured EMF fits well to a lorentzian function with a quality factor $Q \approx 1700$. The beam displacement Δx is related to the EMF $\mathscr{E}$ by[25]:

$$\Delta x = \frac{\mathscr{E}}{\xi l B \omega} \qquad (1)$$

where $\xi = 0.523$ is an integration constant. We thus determine the displacement Δx as a function of power P, as shown in Fig. 2, yielding the resonator mass $m = 2.84 \times 10^{-15}$ kg and effective spring constant $k = 1{,}530\,{\rm N\,m^{-1}}$.

The SET was characterized using low-frequency electrical measurements, giving a series junction resistance $R_{J1} + R_{J2} = 200\,{\rm k\Omega}$, a gate capacitance $C_g = 0.59$ fF, a coupling capacitance between the beam electrode and the SET of $C = 0.13$ fF, and a total SET island capacitance $C_\Sigma = 1.3$ fF. In order to detect motion at the resonant frequency of the beam, the SET was operated as a mixer[11], with a local oscillator (LO) voltage $V_{\rm LO}$ applied to the gate at a frequency offset from the drive frequency by an intermediate frequency (IF) of less than 1 kHz ($f_{\rm IF} = |f_{\rm LO} - f|$). The SET was biased so as to give optimum mixing signal, with $V_{\rm sd} \approx e/C_\Sigma$ and the dc gate voltage adjusted to give peak dc current. The $V_{\rm LO}$ amplitude was set to give maximum signal gain, with coupled charge at the LO frequency $q_{\rm LO} \approx 0.4e$. The voltage across the SET was measured at the intermediate frequency.

Figure 3a shows the mixer signal for a drive power $P = -125$ dBm. Using the magnetomotive calibration, this corresponds to an extrapolated amplitude of $\Delta x = 2.3 \times 10^{-14}$ m on resonance. The charge Δq detected by the SET is due to the change in coupling capacitance times the beam voltage, $\Delta q = V_{\rm beam}\Delta C$, as well as secondary signals due to the induced EMF, and capacitively coupled charge due to cable resonances and ohmic losses. The former is very small compared to the direct signal (less than 1%), and the second varies slowly with frequency. Thus the total signal detected by the SET has the form of a lorentzian, plus a background with an arbitrary phase, as shown in Fig. 3a.

The quality factor Q and resonant frequency f_0 obtained using the SET were the same as those from the magnetomotive technique, and the amplitude varied as $P^{1/2}$. The SET response is found to be 9.9

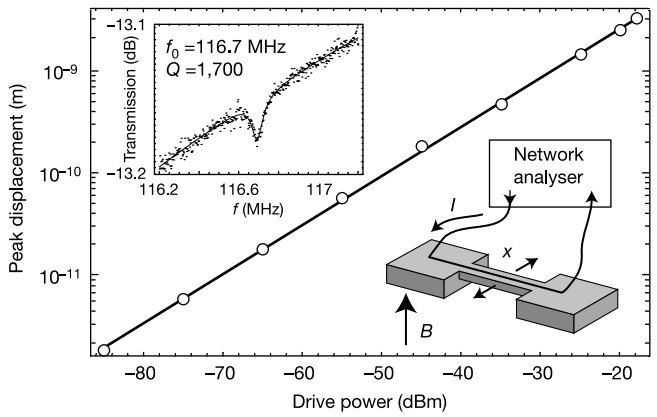

Figure 2 Magnetomotive measurements of the beam resonance. Upper inset, Raw magnetomotive transmission data (20 averages, 10 Hz bandwidth) as a function of drive frequency f, for a drive power $P = -85$ dBm, with a fit of a lorentzian line shape with a linear background. The fit yields the resonance frequency $f_0 = 116.7$ MHz and quality factor $Q = 1700$. The main plot shows the measured midpoint displacement Δx of the beam driven at its frequency resonance $f = f_0$, as a function of magnetomotive drive power P at 30 mK and in an 8 T magnetic field. The fit response $\Delta x = 839\sqrt{P}$ nm/W$^{1/2}$ (solid line), with the beam's known physical geometry (lower inset), corresponds to an effective spring constant $k = 1{,}530\,{\rm N\,m^{-1}}$ and resonator mass $m = 2.84 \times 10^{-15}$ kg.

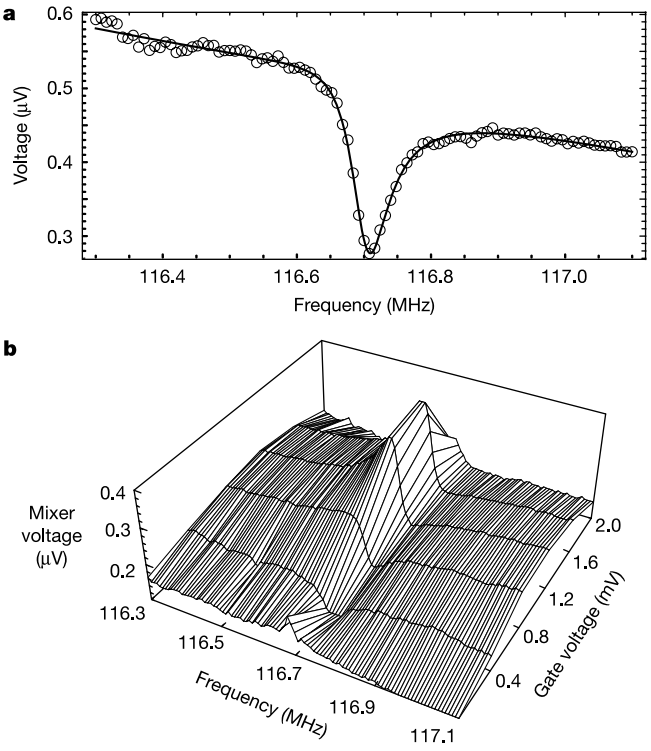

Figure 3 Single electron transistor measurement of the beam motion. **a**, Intermediate frequency voltage (SET mixer output) as a function of beam drive frequency, for $P = -125$ dBm drive power. The solid line is a fit to a lorentzian plus linear background with arbitrary phase. The beam electrode had a d.c. voltage $V_{\rm beam} = 5$ V, the LO power was −70 dBm, and the IF was 151 Hz. The SET gate voltage was tuned to give maximum signal. **b**, IF voltage for $P = -115$ dBm drive power, as a function of d.c. gate voltage and drive frequency. The slowly varying background interferes with the resonance signal, whose phase varies with the gate voltage.

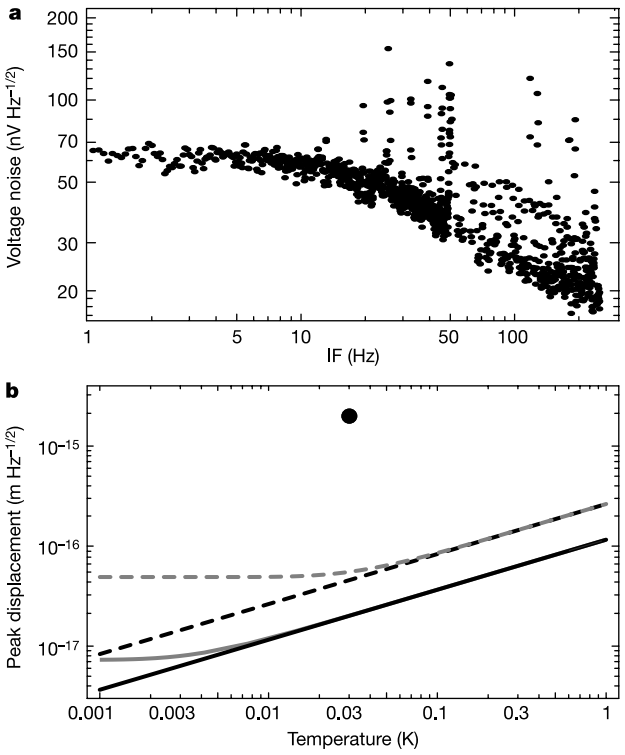

Figure 4 Noise and quantum limits for the device. **a**, Output voltage noise $S_V^{1/2}$ as a function of mixer intermediate frequency in the same configuration as used for the driven beam measurements (LO = −70 dBm, $f_{LO} = 100$ MHz, $V_{sd} \approx e/C_\Sigma$, $V_{beam} = 5$ V, $B = 8$ T, $T = 30$ mK). For the displacement measurements, an intermediate frequency of 151 Hz was used, corresponding to a noise level of about 20 nV Hz$^{-1/2}$. **b**, Calculated displacement noise for two resonators, the resonator measured in this experiment (solid lines) and for a hypothetical 1–GHz resonator (dashed lines), fabricated from GaAs with dimensions 450 × 50 × 40 nm and $Q = 10^4$. The black lines correspond to the thermal noise and the grey lines include the back-action noise and zero-point motion in an ideal quantum-limited position measurement. The measured noise of our device is indicated by the black circle.

Δx Vμm^{-1}, proportional to the displacement Δx, when the SET is biased optimally, with a LO frequency offset from the beam drive signal by 151 Hz. As the SET gate voltage is varied from the optimum value, Fig. 3b, the sensitivity decreases and interference with the background becomes more pronounced. The resonant signal decreases linearly with magnetic field B, and increases linearly with V_{beam}.

Figure 4a shows the output voltage noise of the SET mixer. For the intermediate frequency used (151 Hz), the noise (~20 nV Hz$^{-1/2}$) is dominated by the second-stage amplifier. The displacement sensitivity can be calculated from the SET response: We find a peak sensitivity of $S_x^{1/2} \approx 2.0 \times 10^{-15}$ m Hz$^{-1/2}$.

We can now evaluate the potential for quantum-limited detection: In Fig. 4b we show the calculated thermal and quantum noise for this beam, and for a 1–GHz resonator, which would be in its quantum ground state at the base temperature of our dilution refrigerator. We see that the detector noise is ~100 times larger than the thermal noise of the measured beam, and about a factor of ~20 larger than the quantum noise of a 1–GHz resonator with $Q = 10^4$. By using improved electronics and impedance matching, the second-stage noise could be reduced by roughly a factor of ten, and better lithography could reduce the SET-beam separation, increasing the SET response. A higher–quality factor would yield larger signals in both the thermal and quantum limits; experimentally the Q is observed to reduce as the resonators are made smaller, at least partly due to surface damage and contamination. Flash heating of resonators in vacuum has been demonstrated to yield significantly higher quality factors[26,27], a technique which could be applied here. The expected increase in displacement sensitivity using a combination of these techniques could, in a second–generation device, allow measurement in the quantum-limited regime.

In conclusion, we have demonstrated an ultrasensitive, potentially quantum-limited displacement sensor based on a single-electron transistor, enabling us to read out the motion of a nanomechanical resonant beam at its resonant frequency. The device has a displacement sensitivity of 2.0×10^{-15} m Hz$^{-1/2}$ at the 116.7–MHz resonant frequency of the mechanical beam, limited by the noise in the conventional electronics. □

Received 28 March; accepted 29 May 2003; doi:10.1038/nature01773.

1. Bocko, M. F. & Onofrio, R. On the measurement of a weak classical force coupled to a harmonic oscillator: Experimental progress. *Rev. Mod. Phys.* **68,** 755–790 (1996).
2. Braginsky, V. B. & Khalili, F. Y. *Quantum Measurement* (Cambridge Univ. Press, Cambridge, 1992).
3. Cho, A. Researchers race to put the quantum in mechanics. *Science* **299,** 36–37 (2002).
4. Sidles, J. A. *et al.* Magnetic resonance force microscopy. *Rev. Mod. Phys.* **67,** 249–265 (1995).
5. Armour, A. D., Blencowe, M. P. & Schwab, K. C. Entanglement and decoherence of a micromechanical resonator via coupling to a cooper-pair box. *Phys. Rev. Lett.* **88,** 148301 (2002).
6. Tobar, M. E. & Blair, D. G. Sensitivity analysis of a resonant-mass gravitational wave antenna with a parametric transducer. *Rev. Sci. Instrum.* **66,** 2751–2759 (1995).
7. Long, J. C. *et al.* Upper limits to submillimetre-range forces from extra space-time dimensions. *Nature* **421,** 922–925 (2003).
8. White, J. D. An ultra high resolution displacement transducer using the Coulomb blockade electrometer. *Jap. J. Appl. Phys 2* **32,** L1571–L1573 (1993).
9. Blencowe, M. P. & Wybourne, M. N. Sensitivity of a micromechanical displacement detector based on the radio-frequency single-electron transistor. *Appl. Phys. Lett.* **77,** 3845–3847 (2000).
10. Zhang, Y. & Blencowe, M. P. Intrinsic noise of a micro-mechanical displacement detector based on the radio-frequency single-electron transistor. *J. Appl. Phys.* **91,** 4249–4255 (2002).
11. Knobel, R. & Cleland, A. N. Piezoelectric displacement sensing with a single-electron transistor. *Appl. Phys. Lett.* **81,** 2258–2260 (2002).
12. Caves, C. M., Thorne, K. S., Drever, R. W. P., Sandberg, V. D. & Zimmermann, M. On the measurement of a weak classical force coupled to a quantum-mechanical oscillator. 1. Issues of principle. *Rev. Mod. Phys.* **52,** 341–392 (1980).
13. Huang, X. M. H., Zorman, C. A., Mehregany, M. & Roukes, M. L. Nanoelectromechanical systems: Nanodevice motion at microwave frequencies. *Nature* **421,** 496 (2003).
14. Abramovici, A. *et al.* Improved sensitivity in a gravitational wave interferometer and implications for LIGO. *Phys. Lett. A* **218,** 157–163 (1996).
15. Mamin, H. & Rugar, D. Sub-attonewton force detection at millikelvin temperature. *Appl. Phys. Lett.* **79,** 3358–3360 (2001).
16. Cleland, A. N. & Roukes, M. L. External control of dissipation in a nanometer-scale radiofrequency mechanical resonator. *Sensors Actuators A* **72,** 256–261 (1999).
17. Beck, R. G. *et al.* GaAs/AlGaAs self-sensing cantilevers for low temperature scanning probe microscopy. *Appl. Phys. Lett.* **73,** 1149–1151 (1998).
18. Schoelkopf, R. J., Wahlgren, P., Kozhevnikov, A. A., Delsing, P. & Prober, D. E. The radiofrequency single-electron transistor (rf-SET): A fast and ultrasensitive electrometer. *Science* **280,** 1238–1242 (1998).
19. Devoret, M. H. & Schoelkopf, R. J. Amplifying quantum signals with the single-electron transistor. *Nature* **406,** 1039–1046 (2000).
20. Cleland, A. N., Aldridge, J. S., Driscoll, D. C. & Gossard, A. C. Nanomechanical displacement sensing using a quantum point contact. *Appl. Phys. Lett.* **81,** 1699–1701 (2002).
21. Fulton, T. A. & Dolan, G. J. Observations of single-electron charging effects in small tunnel junctions. *Phys. Rev. Lett.* **59,** 109–112 (1987).
22. Knobel, R., Yung, C. S. & Cleland, A. N. Single-electron transistor as a radio-frequency mixer. *Appl. Phys. Lett.* **81,** 532–534 (2002).
23. Martinis, J. M., Devoret, M. H. & Clarke, J. Experimental tests for the quantum behavior of a macroscopic degree of freedom: The phase difference across a Josephson junction. *Phys. Rev. B* **35,** 4682 (1987).
24. Greywall, D. S., Yurke, B., Busch, P. A., Pargellis, A. N. & Willett, R. A. Evading amplifier noise in nonlinear oscillators. *Phys. Rev. Lett.* **72,** 2992–2995 (1994).
25. Cleland, A. N. & Roukes, M. L. Fabrication of high frequency nanometer scale resonators from bulk Si crystals. *Appl. Phys. Lett.* **69,** 2653 (1996).
26. Yang, J., Ono, T. & Esashi, M. Surface effects and high quality factors in ultrathin single-crystal silicon cantilevers. *Appl. Phys. Lett.* **77,** 3860–3862 (2000).
27. Yasumura, K. Y. *et al.* Quality factors in micron- and submicron-thick cantilevers. *J. Microelectromech. Syst.* **9,** 117–125 (2000).

Acknowledgements We thank C. Yung, D. Schmidt and S. Aldridge for conversations, and B. Hill for processing support. We acknowledge support provided by the National Science Foundation XYZ-On-A-Chip programme, by the Army Research Office, and by the Office of Naval Research/DARPA SPINS programme.

Competing interests statement The authors declare that they have no competing financial interests.

Correspondence and requests for materials should be addressed to A.N.C. (cleland@physics.ucsb.edu).

Nanoscale radio-frequency thermometry

D. R. Schmidt, C. S. Yung, and A. N. Cleland
Department of Physics, University of California, Santa Barbara, California 93106

(Received 21 March 2003; accepted 22 May 2003)

We experimentally demonstrate the high bandwidth readout of a thermometer based on a superconductor–insulator–normal metal (SIN) tunnel junction, embedded in a rf resonant circuit. Our implementation enables basic studies of the thermodynamics of mesoscopic nanostructures. It can also be applied to the development of fast calorimeters, as well as ultrasensitive bolometers for the detection of far-infrared radiation. We discuss the operational details of this device, and estimate the ultimate temperature sensitivity and measurement bandwidth. © *2003 American Institute of Physics.* [DOI: 10.1063/1.1597983]

Thermodynamic studies of mesoscopic devices have lagged far behind the corresponding electrical and magnetic investigations. This dearth can be attributed to a lack of fast, robust thermometers that can be easily integrated with nanoscale structures. Electronic thermometers that function at very low temperatures and have fast response times will enable future probes of thermal physics at smaller size scales and shorter time spans than have previously been explored, and are also a key technology for far-infrared bolometry. In this letter, we describe our development of a nanoscale thermometer, based on a superconductor–insulator–normal metal (SIN) tunnel junction, that should allow thermodynamic measurements in the 1–100-MHz frequency range.

The measurement of temperature in nanoscale systems is a difficult problem for which a number of different approaches have been used. One very sensitive technique is to use a dc superconducting quantum interference device to measure the Johnson–Nyquist noise in a normal metal film. This approach has been used to measure electron–phonon coupling effects in normal metal films,[1,2] as well as in the first observation of the quantum of thermal conductance for phonons[3] by Schwab and coworkers.[4] By contrast, the earlier measurement of the quantum of thermal conductance for electrons[5,6] used the thermoelectric effect in a quantum point contact. Another semiconductor-based method uses the temperature dependence of weak localization in heavily doped GaAs.[7] Thermopower in mesoscopic AuFe wires has been extensively studied using noise thermometry with conventional amplifiers.[8]

Here, we describe the use of submicron SIN tunnel junctions as high-speed thermometers. Large-area SIN tunnel junctions have been used as the thermistor element in bolometric applications,[9] and we have previously used mechanically-suspended SIN junctions as low-frequency thermometers to confirm the measurement of the quantum of thermal conductance.[10] At temperatures sufficiently below the superconducting transition temperature T_C, the tunnel junction's small-signal resistance at zero bias, $R_0 \equiv dV/dI(0)$, is exponentially dependent on the ratio of temperature T to the superconducting energy gap Δ, $R_0 \propto e^{\Delta/k_B T}$. This resistance can be measured using very small bias currents, with negligible self-heating. The resulting high responsivity of the SIN junction, and the fact that it can be well impedance-matched to room-temperature amplifiers, allows its use in a variety of situations. For example, full density-of-states measurements have been made on mesoscopic devices with SIN junctions.[11]

Previous applications of submicron SIN tunnel-junction thermometers have been conducted under dc or audio-frequency heating conditions. However, these tunnel junctions should be able to operate at much higher frequencies. The intrinsic electrical bandwidth is set by the product of the tunnel resistance R_0 and the junction capacitance C_J, $f_{3\,\mathrm{dB}} = 1/2\pi R_0 C_J$. For a fixed tunnel barrier thickness, this product is independent of the junction area A. With typical values of $R_0 A \sim 10^3\ \Omega\ \mu\mathrm{m}^2$ and $C_J/A \sim 10^{-13}\ \mathrm{F}/\mu\mathrm{m}^2$, this corresponds to $f_{3\,\mathrm{dB}} \sim 2$ GHz.

The time scale for the thermal relaxation of the normal metal electrons depends on the cooling mechanism. Diffusive cooling of the electrons into a larger normal metal volume occurs at time scales dictated by the diffusion constant, and can be made less than 1 ns. The time scale for cooling via phonon emission is set at low temperatures by the electron–phonon relaxation time, and possibly by the quasiparticle relaxation time in the superconductor. The small-signal electron–phonon thermal conductance to the substrate is $G_{e-p} = 5\Sigma V T^4$, where Σ is a material-dependent parameter and V the normal metal volume.[2,12] The electronic heat capacity is also proportional to volume, $C_e = \gamma V T$, resulting in a volume-independent thermal time constant $\tau_{\mathrm{th}} = C/G_{e-p} = \gamma/5\Sigma T^3 \sim 10\ T^{-3}$ ns K^3.[13] The relaxation rate of a phonon-cooled metal is thus about $1/\tau_{\mathrm{th}} \sim 10^8$ Hz at 1 K, and 10^5 Hz at 100 mK.

Stray cabling capacitance limits the measurement bandwidth of many mesoscopic devices to the audio range. A number of researchers have recognized the merits of using rf resonant circuits to eliminate the bandwidth-reducing effect of this capacitance. The device is placed in a resonant circuit with a discrete inductor L and capacitance C, such that the device resistance acts to damp the circuit resonance (see Fig. 1). Thus, the resistance measurement can be performed by measuring the power reflected from the LC circuit near its resonance frequency $f_{\mathrm{res}} = 1/2\pi\sqrt{LC}$, which can easily be arranged to fall in the 50–2000-MHz range. Gödel *et al.*[14] employed this technique to measure a quantum point contact.

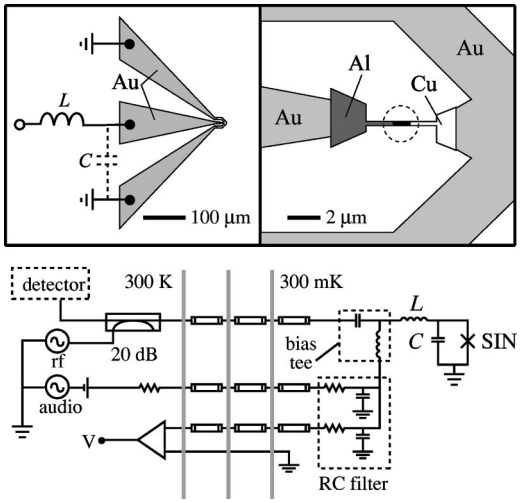

FIG. 1. Top: Schematic of the tunnel-junction layout, on the right showing the metal electrode geometry with the tunnel junction in the dotted circle, and on the left the larger-scale bond pads with the LC circuit, the C due to the capacitance of the bond pads. Bottom: Readout circuit, configured for simultaneous dc and rf measurements. All electrical leads are thermally clamped at each stage of the cryostat, and the dc and rf portions are connected together through a rf bias tee. The resonant circuit comprises the inductor L and capacitance C, the latter in parallel with the tunnel junction SIN.

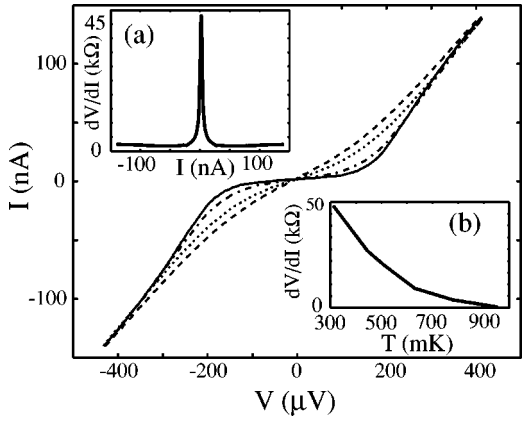

FIG. 2. Dc current–voltage characteristics, measured at a number of different temperatures. The superconducting gap of Al is easily visible at the lowest temperature (solid line: 315 mK) which was thermally smeared as the temperature was raised (dash-dot, 510 mK; dotted, 780 mK; dashed, 950 mK). Inset (a): Bias-dependent differential resistance $R(I)=dV/dI(I)$ at 315 mK. Inset (b): Zero-bias resistance R_0 as a function of temperature.

Record charge sensitivity was achieved by Schoelkopf *et al.*[15] by reading out a single-electron transistor (SET) in a LC resonant circuit. Fujisawa *et al.*[16] used a qualitatively similar transmission-based measurement to study the high-frequency noise in a GaAs quantum dot. The maximum readout bandwidth Δf is set by the width of the LC resonance, which for a large resistance device is set by the $Z_0=50\ \Omega$ cable, and is of order $\Delta f=f_{\mathrm{res}}/Q=Z_0/2\pi L\sim 10-100$ MHz. While a frequency of 100 MHz is still below the intrinsic electrical bandwidth of the SIN junction, it is sufficient to allow the measurement of the electron–phonon relaxation time for a submicron SIN thermometer as well as other phonon-mediated relaxation processes.

We fabricated the SIN tunnel junctions using a standard multiple-angle evaporation technique, using Cu as the normal metal and Al as the superconductor.[17] The tunnel junction had a 90 nm thick Al layer and a 90 nm thick Cu layer, with an overlap area of $0.3\times 1.0\ \mu\mathrm{m}^2$, and a normal state resistance of 2.5 kΩ. The Cu normal metal element is electrically and thermally connected to the Au ground lead.

We glued the GaAs chip to a printed circuit board mounted in a small metal box, and made electrical connections using Au wire bonds. A surface-mounted coil provided $L=390$ nH of inductance. The stray resonant capacitance $C=0.6$ pF resulted in a LC resonance frequency of about $f_{\mathrm{res}}=340$ MHz.

The box containing the SIN junction was mounted in a ^{3}He cryostat wired with the measurement circuit shown in Fig. 1. The current–voltage characteristics for temperatures from 310 to 950 mK are shown in Fig. 2, with the differential resistance at 315 mK shown in inset (a). The measured superconducting voltage gap is $2\Delta/e=386\ \mu$V, typical for thin film Al. The differential resistance at zero bias $R_0(T)$ is plotted in inset (b).

We then measured the reflected rf power from the LC resonator with the embedded tunnel junction. For swept frequency measurements, an rf signal was generated at the source (reflection) port of a two-port network analyzer, and used to measure the reflection coefficient of the resonator as a function of both dc current bias and temperature. The source power at the top of the cryostat was typically -100 dBm (100 fW), with a one-way cable loss of about 2.5 dB. We display our measurements in terms of the total round-trip return loss R_{loss}, including the cable loss.

Figure 3(a) shows the measured return loss at the LC resonance frequency, as a function of dc current bias. The return loss is given by $R_{\mathrm{loss}}=|(Z_0+Z)/(Z_0-Z)|^2$, where Z is the LC resonator impedance, $Z\approx R/Q^2$ for an SIN differential resistance $R=dV/dI$ measured on resonance. The return loss clearly corresponds to the dc differential resistance shown in Fig. 2(a). Below 510 mK, additional structure appears, as shown in Fig. 3(b). This double-lobed behavior is easily understood: For one value of R, the LC resonant circuit is most closely matched to the cable impedance Z_0, maximizing the return loss at that point. This occurs for $R(I)=22$ kΩ in our measurements. This is also exhibited in the temperature dependence of the return loss, shown in Fig. 4(a). The maximum in the return loss is observed at ~ 510 mK, for which $R_0=dV/dI(I=0)\sim 20$ kΩ. The optimal temperature range for rf thermometry can be controlled by the choice of circuit parameters.

Finally, we measured the noise properties of the rf thermometer, using a mixer to detect the reflected power. The mixer local oscillator (LO) was provided by a separate signal source phase-locked to the rf drive. The phase of the LO was adjusted to achieve monotonic response as a function of bias. The mixer output was low-pass filtered (<20 MHz), amplified and Fourier transformed using a dynamic signal analyzer, allowing measurement of the noise from dc to 100 kHz.

The dominant source of noise was from the first-stage amplifier, and as expected was flat, with no measurable $1/f$ component. For an input power of -110 dBm (10 fW) to the LC resonator, we measured a resistance noise of 40 $\Omega/\mathrm{Hz}^{1/2}$.

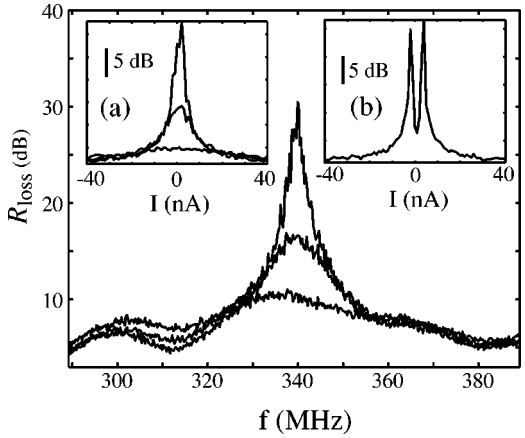

FIG. 3. Return loss as a function of drive frequency. The LC resonance is strongly modulated by biasing the SIN junction, shown by the three curves at 0.0, 6.0, and 13.0 nA. The return loss R_{loss} includes the contribution due to the cable. Higher R_{loss} indicates lower reflected power. Inset (a) Bias-dependent return loss at 338.92 MHz for 510, 630, and 950 mK. The peak in R_{loss} is suppressed at 950 mK. The analogous dc measurement is shown in Fig. 2(a). Inset (b) At 315 mK the return loss at 338.92 MHz is doubly-peaked as a function of current bias.

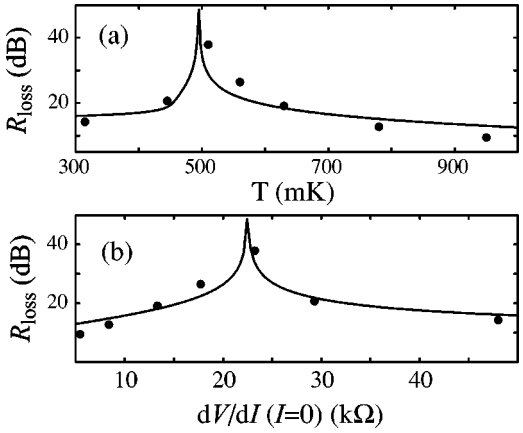

FIG. 4. (a) Temperature dependence of the return loss at zero bias and 338.92 MHz is nonmonotonic and peaked at ~510 mK. (b) The data shown in (a) and from Fig. 2(b) were used extract the dependence of return loss on the differential resistance of the tunnel junction. When the $dV/dI(0)$ ~22 kΩ, the resonator is closely matched to the cable impedance and the return loss is maximized. In (a) and (b), the solid line is a calculated result, assuming optimal matching to the cable impedance at dV/dI~22 kΩ.

Using a temperature responsivity dT/dR of 7 μK/Ω, we calculate the temperature noise to be ~280 μK/Hz$^{1/2}$. While this is comparable to the spectral noise density of the dc measurement for similar input power, the bandwidth is far higher.

This noise figure is very promising for our measurement system, but leaves significant room for improvement. The first-stage amplifier can be operated at cryogenic temperatures, improving its input noise by a factor of 15. Secondly, lowering the temperature of the SIN tunnel junction to below 300 mK would increase the sensitivity. Lastly, the input rf power and frequency can be optimized for largest signal. These contributions are multiplicative, and each can realistically lower the noise by about an order of magnitude. We therefore estimate that a noise temperature of better than 1 μK/Hz$^{1/2}$ is attainable. The measurement bandwidth achieved using our resonant circuit is approximately the width of the resonance shown in Fig. 3, or about 10 MHz. If an optimized SIN-based thermometer were integrated into a bolometer, it would potentially be able to detect single few-THz photons at count rates of up to about 10^7 Hz.[18]

In conclusion, we have demonstrated a technique to measure the temperature of the normal metal side of an SIN tunnel junction thermometer with a bandwidths of up to 100 MHz. This rf-SIN opens up possibilities for studies of basic thermodynamics in nanostructures, and for bolometric detector technology. Thermodynamic measurements can now be performed at sub-μs time scales with the rf-SIN.

We acknowledge financial support provided by the NASA Office of Space Science under grant NAG5-11426, the Army Research Office under Award DAAD-19-99-1-0226.

[1] M. L. Roukes, M. R. Freeman, R. S. Germain, R. C. Richardson, and M. B. Ketchen, Phys. Rev. Lett. **55**, 422 (1985).
[2] F. C. Wellstood, C. Urbina, and J. Clarke, Phys. Rev. B **49**, 5942 (1994).
[3] L. G. C. Rego and G. Kirczenow, Phys. Rev. Lett. **81**, 232 (1998).
[4] K. Schwab, E. A. Henriksen, J. M. Worlock, and M. L. Roukes, Nature (London) **404**, 974 (2000).
[5] L. W. Molenkamp, T. Gravier, H. van Houten, O. J. A. Buijk, M. A. A. Mabesoone, and C. T. Foxon, Phys. Rev. Lett. **68**, 3765 (1992).
[6] A. Greiner, L. Reggiani, T. Kuhn, and L. Varani, Phys. Rev. Lett. **78**, 1114 (1997).
[7] T. S. Tighe, J. M. Worlock, and M. L. Roukes, Appl. Phys. Lett. **70**, 2687 (1997).
[8] C. Strunk, M. Henny, C. Schönenberger, G. Neuttiens, and C. V. Haesendonck, Phys. Rev. Lett. **81**, 2982 (1998).
[9] M. Nahum and J. M. Martinis, Appl. Phys. Lett. **63**, 3075 (1993).
[10] C. S. Yung, D. R. Schmidt, and A. N. Cleland, Appl. Phys. Lett. **81**, 31 (2002).
[11] H. Pothier, S. Guéron, N. O. Birge, D. Esteve, and M. H. Devoret, Phys. Rev. Lett. **79**, 3490 (1997).
[12] V. F. Gantmakher, Rep. Prog. Phys. **37**, 317 (1974).
[13] See Ref. 10: Yung *et al.* determined that $\Sigma \sim 2\times10^{-9}$ W/(μm^3 K^5). At low temperatures, $\gamma \sim 10^{-16}$ J/(μm^3 K^2) for Cu.
[14] W. Gödel, S. Manus, D. Wharam, J. P. Kotthaus, G. Böhm, W. Klein, G. Tränkle, and G. Weimann, Electron. Lett. **30**, 977 (1994).
[15] R. J. Schoelkopf, P. Wahlgren, A. A. Kozhevniv, P. Delsing, and D. E. Prober, Science **280**, 1238 (1998).
[16] T. Fujisawa and Y. Hirayama, Appl. Phys. Lett. **77**, 543 (2000).
[17] T. A. Fulton and G. J. Dolan, Phys. Rev. Lett. **59**, 109 (1987).
[18] A 0.005-μm^3 Cu normal metal element has a heat capacity $C \sim 1\times10^{-19}$ J/K at 200 mK. A 5-THz photon then raises the temperature by ~30 mK. For a noise figure of 1 μK/Hz$^{1/2}$ and 10-MHz bandwidth, the single photon signal would equal the rms temperature noise.

Nanomechanical displacement sensing using a quantum point contact

A. N. Cleland[a] and J. S. Aldridge
Department of Physics and iQUEST, University of California, Santa Barbara, California, 93106

D. C. Driscoll and A. C. Gossard
Materials Department and iQUEST, University of California, Santa Barbara, California, 93106

(Received 10 May 2002; accepted for publication 10 June 2002)

We describe a radio frequency mechanical resonator that includes a quantum point contact, defined using electrostatic top gates. We can mechanically actuate the resonator using either electrostatic or magnetomotive forces. We demonstrate the use of the quantum point contact as a displacement sensor, operating as a radio frequency mixer at the mechanical resonance frequency of 1.5 MHz. We calculate a displacement sensitivity of about 3×10^{-12} m/Hz$^{1/2}$. This device will potentially permit quantum-limited displacement sensing of nanometer-scale resonators, allowing the quantum entanglement of the electronic and mechanical degrees of freedom of a nanoscale system. © *2002 American Institute of Physics.* [DOI: 10.1063/1.1497436]

The observation of quantized plateaus in the conductance of high-mobility quantum point contacts[1,2] has generated significant interest in both the physics and application of these devices. The highly sensitive dependence of the source-drain conductance of a quantum point contact (QPC) on electrostatic fields provides a straightforward means of detecting very small electronic signals. The QPC has been used, for example, to detect charge motion and controllably introduce quantum decoherence in the electron transport through an electron interferometer.[3,4] A QPC has been demonstrated[5] as a scanned charge-imaging sensor, with a measured charge noise of about 0.01 $e/\mathrm{Hz}^{1/2}$ at 1 kHz.

Of further interest is the potentially extremely large bandwidth attainable using a QPC, due to the very small intrinsic capacitance ($\sim$100 aF) and short electron transit times ($\sim$1 ps); the QPC should in principle respond at frequencies up to of order 10 THz.[6] However, the relatively large resistance of the QPC, coupled with unavoidable stray cabling capacitance, typically limits its practical bandwidth to the order of 10^4–10^5 Hz. The QPC has however recently been demonstrated[7] to work well as a radio frequency (rf) mixer, by employing the nonlinearity in the QPC current–voltage characteristic to generate harmonic multiples of the applied rf signals. A local oscillator (LO) at a frequency ω_{LO}, combined with a signal at ω_S, will, through the QPC nonlinearity, generate signals at the sum and difference frequencies $|\omega_{\mathrm{LO}}\pm\omega_S|$. For a sufficiently small intermediate frequency (IF) $\omega_{\mathrm{IF}}=|\omega_{\mathrm{LO}}-\omega_S|$, the difference frequency will lie within the output bandwidth of the QPC, and the signal can thereby be detected. Mixing has been demonstrated[8] at frequencies up to 2.9 GHz, with an optimal conversion loss of -13 dB.

In this work we demonstrate the use of a QPC mixer as a displacement detector, where we take advantage of the piezoelectric effect in GaAs to modulate the current through an integrated QPC. Previously, a micromachined GaAs mechanical resonator that included an integrated field-effect transistor (FET) has been demonstrated,[9,10] with a measured displacement sensitivity of 10^{-9} m/Hz$^{1/2}$. A significant limitation in this device was the low output bandwidth, of order 10^3 Hz.

Our device is shown in Fig. 1. The structure was etched from a single-crystal GaAs heterostructure grown by molecular beam epitaxy, comprising a bulk $\langle100\rangle$ GaAs wafer, 700 nm of $Al_{0.7}Ga_{0.3}As$ (the sacrificial layer), 600 nm of GaAs, 40 nm of $Al_{0.3}Ga_{0.7}As$, a Si delta-doped layer, 70 nm of $Al_{0.3}Ga_{0.7}As$, and a 10 nm GaAs capping layer. The suspended mechanical structure includes all layers above the sacrificial layer (see below). The two-dimensional electron gas (2DEG) in which the QPC is formed is at the lower GaAs–$Al_{0.3}Ga_{0.7}As$ interface, where similar samples[11] had a carrier density of $\sim1.4\times10^{15}/\mathrm{m}^2$, and a mobility of ~40 m^2/V s at 4.2 K. In our device the 2DEG mobility was significantly degraded by processing.

We used photolithography to define a set of NiAuGe ohmic contacts to the 2DEG. Next electron-beam lithography was used to define Ti/Au (5 nm/40 nm) electrodes for the top gates, as well as for actuation of the mechanical structure. A second photolithography step defined Ti/Au (5 nm/110 nm) wire-bond pads to make contact with the metal electrodes and ohmic contacts. A second electron beam li-

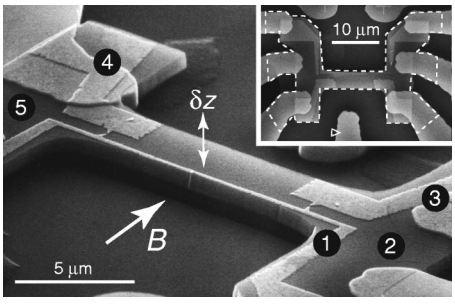

FIG. 1. SEM micrograph of the QPC electrodes defined on the surface of a suspended beam. The magnetic field B used for magnetomotive actuation is indicated, as is the direction of flexure δz. The numbers identify the electrodes: (1) is the drive electrode that also serves as a QPC gate, (2) and (5) define the source and drain ohmic contacts, (3) and (4) the other sides of the two QPC gates. Only one QPC was used at a time. Inset: Larger scale image of the structure, with the dotted line outlining the suspended area.

[a]Electronic mail: cleland@iquest.ucsb.edu

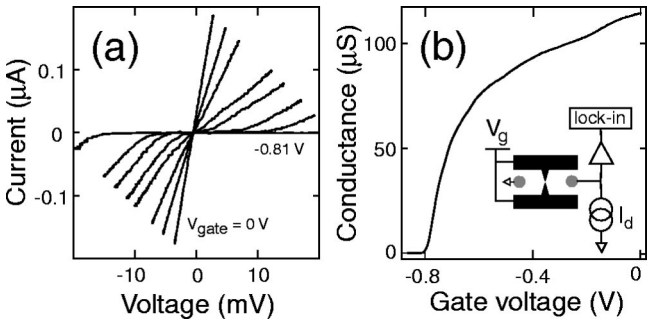

FIG. 2. (a) Current–voltage characteristic for the QPC, measured for different gate voltages $V_g = 0$, -0.64, -0.73, -0.76, -0.77, -0.78, -0.79, and -0.81 V. (b) Conductance at zero bias as a function of gate voltage. Inset: Schematic of measurement setup.

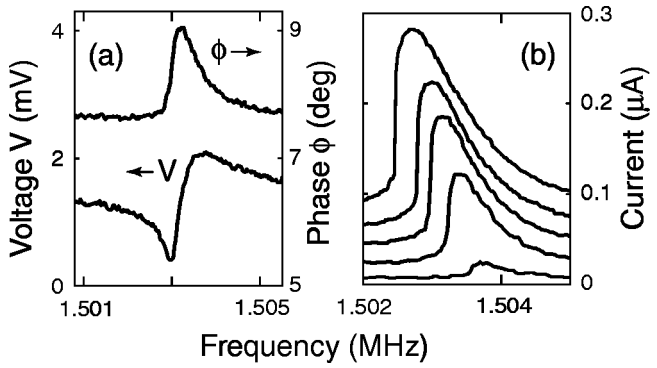

FIG. 3. (a) Amplitude and phase of signal reflected from magnetomotive drive electrode. Measurements made with applied power of -70 dB in a magnetic field of 5 T; (b) intermediate frequency current through QPC for same applied power to magnetomotive drive electrode, in magnetic fields of 1, 2, 3, 4, and 5 T. IF frequency was $\nu_{IF} = \omega_{IF}/2\pi = 13.7$ Hz, with 100% amplitude modulation of the LO signal.

thography step then defined the structural masking layer. The unmasked area of the heterostructure was etched using $SiCl_4$-based reactive ion etching, etching to a depth of about 800 nm, almost through the sacrificial layer. The sacrificial layer was then etched using a timed submersion in concentrated hydrochloric acid, followed by a 10% solution of hydrofluoric acid. This step was timed to suspend the lateral area shown by the dotted outline in Fig. 1, creating a structure with a suspended length of roughly 45 μm and a thickness of 0.72 μm.

The sample was placed in a vacuum can that was submerged in liquid He at 4.2 K. A magnetic field B could be applied in the plane of the sample (see Fig. 1).

We recorded the current–voltage characteristics of the QPC as a function of the voltage applied to the top gate electrodes, numbered 1 and 4 in Fig. 1, as shown in Fig. 2(a). In Fig. 2(b) we show the zero-bias conductance as a function of gate voltage. Quantized steps are not visible in this measurement at 4.2 K. We then characterized the response of the QPC as a rf mixer, by applying a combination of a local oscillator and a signal to the gate electrode 1, and measuring the current through contacts 2 and 5 at the intermediate frequency ω_{IF}. We found that the mixer operates well up to a LO frequency of about 20 MHz, and for intermediate frequencies up to about 2 kHz; these frequencies are limited by the particular measurement configuration rather than by the QPC itself.[12] For a typical configuration with a gate voltage of -0.8 V, dc bias voltage across the QPC of 60 mV, and a LO power of -11 dBm, the IF current i_{IF} through the QPC was linear in the signal voltage v_S, with $i_{IF} \approx 0.9 v_S$ μA/V.

We characterized the mechanical properties of the suspended structure by applying an in-plane magnetic field B, and measuring the resulting electrical impedance of the drive electrode 1. This impedance acquires additional real and imaginary frequency-dependent terms due to the combination of Lorentz-force actuation and the resulting electromotive voltage developed as the structure moves in the magnetic field.[13,14] The fundamental resonance frequency is $\omega_0/2\pi = 1.503$ MHz, with a quality factor $Q \approx 3000$. In Fig. 3(a) we display the response for $B = 5$ T. Shifts in the resonance frequency are apparent, due to the nonlinear response for large motional amplitudes.[15,16]

We employed the QPC to detect the motion: In-plane strain in GaAs, generated by out-of-plane flexure, will generate out-of-plane piezoelectric fields.[17] These modulate the QPC conductance in a manner analogous to the top gate. In Fig. 3(b) we display the measured QPC current i_{IF} when the drive electrode 1 was driven with an amplitude-modulated signal, which served to both generate magnetomotive actuation of the structure, and as a local oscillator for the QPC mixer. The change in the QPC mixer response as a function of ω_{LO} is due to the generation of a frequency-dependent piezoelectric voltage at ω_{LO} between the 2DEG layer and the top gates, and the amplitude modulation of the gate drive then mixes this voltage to the intermediate frequency ω_{IF}, permitting detection of the motion. Data are for a range of magnetic fields, with the expected B^2 dependence for the peak amplitude.

We could also actuate and sense the structure in the absence of a magnetic field; in Fig. 4 we display the QPC current as the LO frequency is swept through the mechanical resonance, for different LO powers. Mechanical actuation occurs due to the electrostatic interaction between the drive electrode 1 and the substrate, and the QPC detects both this frequency-independent voltage, and the resonant piezoelectric voltage due to the strain in the structure.

We can estimate the displacement sensitivity of the QPC from our measurements; using the magnetomotive reflec-

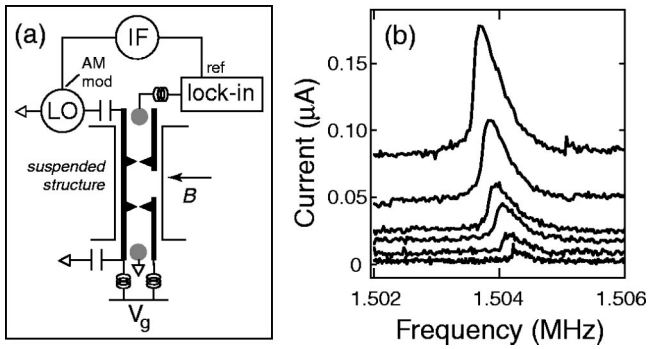

FIG. 4. (a) Measurement schematic for electrostatic drive and detection using the QPC. The LO drive signal is capacitively coupled to electrode 1, and is amplitude modulated at the IF frequency $\omega_{IF}/2\pi = 13.7$ Hz. The QPC current is lock-in detected with the IF signal as a reference. Care was taken to ensure that no spurious mixing signals were detectable. (b) IF current through the QPC for a range of applied LO powers, with $P_{LO} = -61$, -56, -53.5, -51, and -48.5 dB. The remnant magnetic field is estimated from magnetomotive measurements to be less than 0.01 T.

tance measurements, we can calculate the midpoint displacement δz of the structure, and from the corresponding magnitude of the IF current i_{IF}, we find the responsivity $i_{\mathrm{IF}} \approx 28\ \delta z$ nA/μm. Our current detection is limited by the voltage noise in the IF preamplifier, and corresponds to a noise of $\delta z_{\mathrm{rms}} \approx 3 \times 10^{-12}$ m/Hz$^{1/2}$, better than what is achieved with optical interferometry.[18] The corresponding force noise is about $\delta F_{\mathrm{rms}} \approx 0.3$ nN/Hz$^{1/2}$. We note that the thermal force noise $\sqrt{4k_B T m \omega_0 / Q} \approx 1$ fN/Hz$^{1/2} \ll \delta F_{\mathrm{rms}}$, well below our electrical noise level. As noted by Beck *et al.*,[10] the sensitivity *improves* with reduction in size scale, due to the increase in strain for a given displacement. Our device geometry allows for significantly smaller structures, with correspondingly higher frequencies, potentially approaching 1 GHz. The delicate sensitivity of the QPC can therefore potentially be employed as a quantum-limited displacement sensor, and allow the entanglement of a phase-coherent electron transmission sensor with a mechanical resonator.[19]

The authors thank R. Knobel for valuable conversations, and acknowledge the support of a Research Corporation Research Innovations Award, the National Science Foundation XYZ-On-A-Chip Program, and the Army Research Office.

[1] B. J. van Wees, H. van Houten, C. W. J. Beenakker, J. J. G. Williamson, L. P. Kouwenhoven, D. van der Marel, and C. T. Foxon, Phys. Rev. Lett. **60**, 848 (1988).
[2] B. J. van Wees, L. P. Kouwenhoven, E. M. M. Willems, C. J. P. M. Harmans, J. E. Mooij, H. van Houten, C. W. J. Beenakker, J. J. G. Williamson, and C. T. Foxon, Phys. Rev. B **43**, 12431 (1991).
[3] E. Buks, R. Schuster, M. Heiblum, D. Mahalu, and V. Umansky, Nature (London) **391**, 871 (1998).
[4] D. Sprinzak, E. Buks, M. Heiblum, and H. Shtrikman, Phys. Rev. Lett. **84**, 5820 (2000).
[5] L. H. Chen, M. A. Topinka, B. J. LeRoy, R. M. Westervelt, K. D. Maranowski, and A. C. Gossard, Appl. Phys. Lett. **79**, 1202 (2001).
[6] M. J. Kelly, R. J. Brown, C. G. Smith, D. A. Wharam, M. Pepper, H. Ahmed, D. G. Hasko, D. C. Peacock, J. E. F. Frost, and R. Newbury, Electron. Lett. **25**, 992 (1989).
[7] W. Gödel, S. Manus, D. A. Wharam, J. P. Kotthaus, G. Böhm, W. Klein, G. Tränkle, and G. Weimann, Electron. Lett. **30**, 977 (1994).
[8] A. G. C. Haubrich, D. A. Wharam, H. Kriegelstein, S. Manus, A. Lorke, J. P. Kotthaus, and A. C. Gossard, Appl. Phys. Lett. **70**, 3251 (1997).
[9] R. G. Beck, M. A. Eriksson, R. M. Westervelt, K. L. Campman, and A. C. Gossard, Appl. Phys. Lett. **68**, 3763 (1996).
[10] R. G. Beck, M. A. Eriksson, M. A. Topinka, R. M. Westervelt, K. D. Maranowski, and A. C. Gossard, Appl. Phys. Lett. **73**, 1149 (1998).
[11] J. G. E. Harris, D. D. Awschalom, K. D. Maranowski, and A. C. Gossard, J. Appl. Phys. **87**, 5102 (2000).
[12] The LO cable was not 50 Ω terminated, leading to large cable resonances, and the IF output bandwidth was limited by the QPC impedance of about 1 MΩ.
[13] A. N. Cleland and M. L. Roukes, Appl. Phys. Lett. **69**, 2653 (1996).
[14] A. N. Cleland and M. L. Roukes, Sens. Actuators A **72**, 256 (1999).
[15] D. Greywall, B. Yurke, P. Busch, A. Pargellis, and R. Willett, Phys. Rev. Lett. **72**, 2992 (1994).
[16] B. Yurke, D. Greywall, A. Pargellis, and P. Busch, Phys. Rev. A **51**, 4211 (1995).
[17] J. Söderkvist and K. Hjort, J. Micromech. Microeng. **4**, 28 (1994).
[18] H. Mamin and D. Rugar, Appl. Phys. Lett. **79**, 3358 (2001).
[19] A. D. Armour and M. P. Blencowe, Phys. Rev. B **64**, 035311 (2001).

Single-electron transistor as a radio-frequency mixer

R. Knobel, C. S. Yung, and A. N. Cleland[a)]
Department of Physics and iQUEST, University of California, Santa Barbara, Santa Barbara, California 93106

(Received 14 March 2002; accepted for publication 10 May 2002)

We demonstrate the use of the single-electron transistor as a radio-frequency mixer, based on the nonlinear dependence of current on gate charge. This mixer can be used for high-frequency, ultrasensitive charge measurements over a broad and tunable range of frequencies. We demonstrate operation of the mixer, using a lithographically defined thin-film aluminum transistor, in both the superconducting and normal states of aluminum, over frequencies from 10 to 300 MHz. We have operated the device both as a homodyne detector and as a phase-sensitive heterodyne mixer. We demonstrate a charge sensitivity of $<4\times10^{-3}\ e/\sqrt{\mathrm{Hz}}$, limited by room-temperature electronics. An optimized mixer has a theoretical charge sensitivity of $\lesssim1.5\times10^{-5}\ e/\sqrt{\mathrm{Hz}}$. © *2002 American Institute of Physics.* [DOI: 10.1063/1.1493221]

Coulomb blockade can occur when current through a device passes through high-resistance contacts to a small-capacitance island. The condition for Coulomb blockade is that the resistance of each contact must exceed $R_K\equiv h/e^2\approx25.8\ \mathrm{k}\Omega$, and the electrostatic charging energy E_C of the island must satisfy $E_C\equiv e^2/2C_\Sigma\gg k_BT$, where C_Σ is the capacitance of the island. The charging energy can be tuned electrostatically using a gate capacitively coupled to the island; the current is periodic in the gate charge, with a period e, the charge of one electron. In this mode of operation, these devices are known as single-electron transistors (SETs).[1,2] An important application of the SET is as an ultrasensitive electrometer, with a theoretical charge sensitivity[3] of order $10^{-6}e/\sqrt{\mathrm{Hz}}$.

The high electrical resistance associated with Coulomb blockade, coupled with the unavoidable stray cable capacitance, has traditionally limited measurements with the SET to frequencies $\lesssim10^4$ Hz. This can be increased to about 1 MHz by placing a first-stage amplifier in close proximity to the SET.[4,5] A significant innovation has recently been demonstrated,[6] where the SET is coupled through a tuned LC tank circuit, so that at the resonance frequency $\omega_0=1/\sqrt{LC}$ the output impedance of the SET is matched to a 50 Ω cable. This technique, termed a radio-frequency SET (rf-SET), allows operation at resonance frequencies up to $\sim10^9-10^{10}$ Hz, with a demonstrated charge sensitivity near the theoretical limit. However, the measurement bandwidth about the resonant frequency is limited to a few percent of ω_0, as the tank circuit quality factor must satisfy $Q\gtrsim\sqrt{2R_K/50\ \Omega}\approx30$ to achieve impedance matching. This limits applications of this device to measurements where the frequency of the signal to be measured is externally controlled, or is known beforehand to fairly high precision. In addition, the tuning circuit requires a well-characterized electrical environment, which is not always easily achieved (for example, with carbon nanotube-based transistors).

Here we demonstrate the use of the SET as a homodyne detector and as a heterodyne mixer. In the former, the nonlinear dependence of the current I on the coupled charge is employed to mix a rf signal to dc, while in the latter, the signal is mixed with a local oscillator to generate a signal at the difference frequency, close to dc, whose amplitude and phase may be measured. These techniques may be employed with any gated Coulomb blockade device, allowing measurements at frequencies up to $\omega_{\max}\approx I/e$, above which nonadiabatic current transport and photon-assisted tunneling become significant.

For this experiment, we used a lithographically patterned SET, comprising two $\mathrm{Al/AlO}_x\mathrm{/Al}$ tunnel junctions and two interdigitated coupling capacitors, fabricated using electron beam lithography and shadow evaporation[1] [see Fig. 1(a)]. The device was fabricated on a GaAs heterostructure to allow *in situ* fabrication of nanomechanical structures:[7] We plan to implement the mixer as a motion sensor for a nanomechanical resonator, capacitively coupled to the SET.[8]

The device was mounted on a dilution refrigerator and cooled to ≃30 mK. All leads were filtered with metal powder filters[9] and source and drain leads with RC filters at 1.5 K and at room temperature. The SET was operated as a mixer both in the superconducting state and in the normal state, in a magnetic field of 1 T. Figure 1(b) shows the

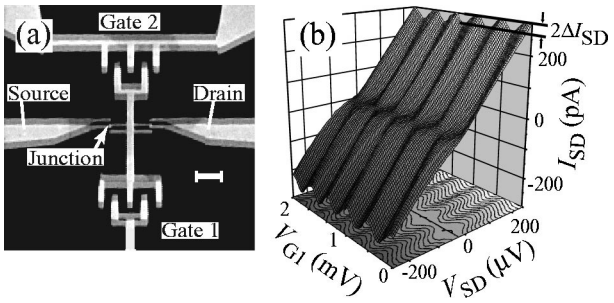

FIG. 1. (a) Electron micrograph of a typical sample, showing the $\approx50\times50\ \mathrm{nm}^2$ overlap of the junctions and the two gate capacitors. The scale bar is 1 μm. (b) dc normal-state current–voltage characteristic of the SET at 30 mK, where the modulation due to gate 1 is shown; the same behavior was seen when modulating gate 2. The device parameters extracted from this measurement are $C_{G1}=4.2\times10^{-16}$ F, $C_{G2}=2.8\times10^{-16}$ F, $R\equiv R_1+R_2=850\ \mathrm{k}\Omega$, and $C_\Sigma\approx2\times10^{-15}$ F.

a)Electronic mail: cleland@iquest.ucsb.edu

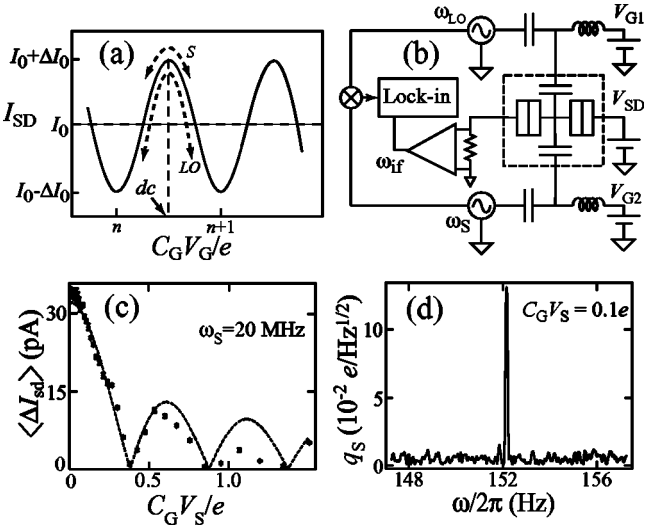

FIG. 2. (a) Schematic diagram of mixing. The gate charge is set for maximum current (dashed vertical line), and a signal and (for heterodyne mixing) local oscillator voltage are coupled to the gate. (b) Mixing circuit schematic of both homodyne and heterodyne mixing. The SET is in the dashed box in the center. (c) Homodyne detector signal at dc, measured as a function of the signal voltage. The signal at 20 MHz was applied to gate 2, while the SET was in the superconducting state. Points are experimental data, and the dashed line is the expected Bessel function response. (d) Heterodyne mixing spectral density about $\omega_{if}=152.15$ Hz, with $C_GV_S=0.1e$, $C_GV_{LO}=0.3e$, $\omega_{LO}/2\pi=20$ MHz, and $\omega_S=\omega_{LO}+\omega_{if}$, with the SET in the normal state. The vertical axis is in units of input signal charge spectral density $q_S=C_GV_S$.

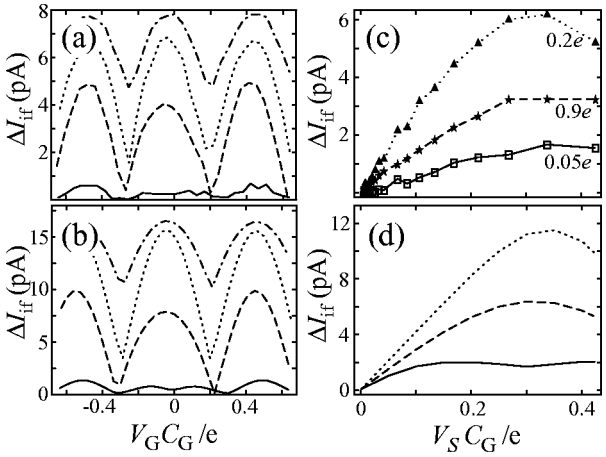

FIG. 3. (a) Amplitude of the mixing signal as a function of the dc gate charge for a range of V_{SD} (offset for clarity, with $V_{SD}=4$, 50, 100, and 150 μV bottom to top), with $\omega_{LO}/2\pi=20$ MHz and $\omega_{if}/2\pi=152.15$ Hz. (b) Modeled mixing current as a function of the dc gate charge, $V_{LO}C_G=0.2e$, $V_SC_G=0.25e$ at 30 mK varying V_{SD} as in (a). (c) Measured *if* current as a function of the rf charge on the gate for $\omega_{LO}/2\pi=20$ MHz and $\omega_{if}/2\pi=152.15$ Hz, with fixed source–drain bias $V_{SD}=90$ μV. The three traces are for varying $V_{LO}C_G/e$. (d) Modeled *if* current for $V_{SD}=100$ μV at 30 mK varying $V_{LO}C_G$ as in (c).

normal-state current–voltage characteristic, as the dc bias on one gate was varied. The relatively large value of the SET resistance limits the noise performance and output bandwidth, as discussed below.

For near-optimal V_{SD}, as shown in Fig. 2(a), the source–drain current I_{SD} is approximately sinusoidal in the gate voltage V_G, with peak-to-peak amplitude $2\Delta I_0$ about an average value I_0, and period e in the gate charge C_GV_G; at optimal source–drain bias $\Delta I_0 \approx I_0$. For homodyne detection, we bias the gate with a dc voltage V_G such that the current is at a maximum, and apply a rf voltage $V_S\cos\omega_St$. For frequencies smaller than the tunneling rate, the dc current is then the time average of the instantaneous current $\langle I_{SD}[V_G+V_S\cos(\omega_St)]\rangle$. At frequencies of order I/e and higher, electrons can be transferred through the SET nonadiabatically, reducing the Coulomb gap.[10] At still higher frequencies, where the photon energy is comparable to the difference in final energy states $\hbar\omega\approx\Delta E$, photon-assisted tunneling can occur. This effect is negligible in our measurements.[11] For heterodyne mixing, we couple a local oscillator (LO) voltage $V_{LO}\cos\omega_{LO}t$ to the other gate, as shown in Fig. 2(b).

The homodyne response is shown in Fig. 2(c) for gate 2 at 20 MHz. For a model current dependence $I_{SD}\approx I_0-\Delta I_0\cos(2\pi C_GV_G/e)$, we expect

$$\langle I_{SD}(V_S)\rangle = I_0 + \Delta I_0\left|J_0\left(\frac{2\pi C_GV_S}{e}\right)\right|, \tag{1}$$

where J_0 is the zeroth-order Bessel function. A fit to this dependence is shown in Fig. 2(c); the zeroes in the response allow us to calibrate the signal voltage V_S. The nonzero capacitance between the gate and source–drain leads can rf modulate V_{SD} as well, causing deviations from Eq. (1) at larger rf amplitudes.

For heterodyne mixing, the signal voltage is applied to one gate, and a local oscillator voltage $V_{LO}\cos\omega_{LO}t$ to the other gate. The source–drain current is modulated by both signals, and a current is generated at the intermediate frequency $\omega_{if}=|\omega_S-\omega_{LO}|$. The *if* signal (magnitude and phase) was detected using a lock-in amplifier, whose reference signal was generated by a separate mixer, shown in Fig. 2(b). High-pass filters ensured that this reference signal was not transmitted to the SET. The measured spectral response is shown in Fig. 2(d), showing the peak at ω_{if} as well as the sideband noise.

Figure 3(a) shows the heterodyne mixer amplitude as the dc source–drain voltage V_{SD} and dc gate voltage V_G are varied. The e periodicity in C_GV_G is observed, and the dependence on V_{SD} has the expected maximum near $e/2C_\Sigma$. Figure 3(c) shows the *if* current as a function of signal amplitude V_S; the same dependence is found when V_{LO} is varied. The gain of the device is tunable by varying the dc gate bias, source–drain voltage, and oscillator power. The *if* response was calculated using an analytic model for the SET,[12] and is shown in Figs. 3(b) and 3(d). The measured response follows the predicted behavior, but is approximately a factor of 2 smaller than calculated. At present we do not understand this discrepancy.

Figure 4(a) shows the frequency dependence of the mixer signal, for fixed ω_{if} and constant LO and signal power. Figure 4(a) shows a measurable signal up to $\omega_{LO}/2\pi\approx 300$ MHz, limited by the $\omega_{max}/2\pi\sim 300$ MHz cutoff frequency for this device. Figure 4(b) shows the ~ 250 Hz output bandwidth for the SET. This can be increased by lowering the junction resistance, operating in the superconducting state, and reducing the cable capacitance. Use of a closely coupled preamplifier or tuned LC circuit could further increase the output bandwidth. Noise measure-

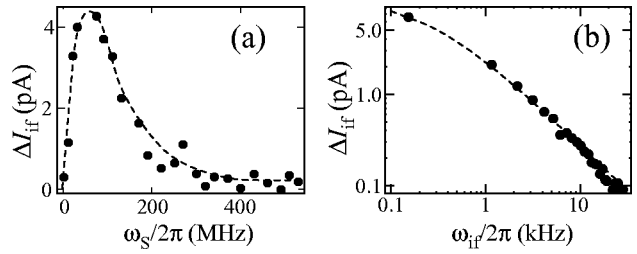

FIG. 4. (a) Mixing signal amplitude as a function of ω_{LO} at constant $\omega_{if}=152.15$ Hz; the signal and LO powers were -68 and -61 dBm, respectively. The low-frequency rolloff is due to high-pass filtering, and the high-frequency rolloff is due to the I_{SD}/e limitation. The dashed line is a guide to the eye. (b) Mixing signal as a function of ω_{if} for $\omega_{\mathrm{LO}}=50$ MHz. The dashed line is a fit that gives a -3 dB single-side bandwidth of 250 Hz.

ments near the intermediate frequency ω_{if} at optimum gain yield a signal charge sensitivity $\delta q_S<4\times10^{-3}e/\sqrt{\mathrm{Hz}}$, limited by noise in the room-temperature electronics [Fig. 2(d)].

The heterodyne response can be understood by using the sinusoidal approximation for the current–charge response. The heterodyne current ΔI_{if} at ω_{if} is then related to the signal and LO voltages V_S and V_{LO} by

$$\Delta I_{if}=2\Delta I_0 J_1\left(\frac{2\pi C_G V_S}{e}\right)J_1\left(\frac{2\pi C_G V_{\mathrm{LO}}}{e}\right), \tag{2}$$

in terms of the first-order Bessel function J_1. The small signal *if* current gain $g_I=\Delta I_{if}/\Delta I_S$ is optimized for V_{LO} at the first maximum of J_1, $C_G V_{\mathrm{LO}}\approx0.293e$. For a current source $\Delta I_S=\omega_S C_G V_S\ll\omega_S e$, the current at optimal bias is $\Delta I_{if}=g_I I_S\approx3.66\Delta I_0 C_G V_S/e=1.83(\omega_{\max}/\omega_S)\Delta I_S$. Current gain is therefore expected at frequencies below $\omega_{\max}\sim300$ MHz for this device.

We estimate the expected charge noise for the mixer using the current shot noise $S_I(\omega)\approx2eI_{\mathrm{SD}}$. The output noise at ω, referenced to the input charge noise power $S_q(\omega)$, is approximately

$$S_q(\omega)=\frac{2eI_{\mathrm{SD}}}{(\partial\Delta I_{if}/\partial q_s)^2}\approx\frac{2eI_{\mathrm{SD}}}{(3.66\Delta I_0/e)^2}, \tag{3}$$

yielding input charge noise $\delta q_S(f)\approx0.97\sqrt{e/I_0}$. For our device this yields $\delta q_S(f)\approx1.3\times10^{-4}e/\sqrt{\mathrm{Hz}}$, while for an optimized SET with $R=2R_K$, C=1 fF, we find $\delta q_S(f)\approx1.5\times10^{-5}e/\sqrt{\mathrm{Hz}}$. This optimized SET would have a current gain of $g_I\approx30$ at 100 MHz and 3 at 1 GHz. An important question remains regarding the impact of $1/f$ charge noise: If this noise modulates the mixer gain, it will contribute at ω, while if not the mixer can operate outside the $1/f$ noise-dominated band even for low ω_{if}.

In conclusion, we have demonstrated the use of a lithographically defined single-electron transistor as a radio-frequency mixer that allows the detection of signals over a fully tunable 300 MHz band. The use of this technique is complementary with SET bandwidth-enhancing techniques such as the rf-SET. The generic nature of the mixer response, and the ease with which the mixer operation can be configured, should allow its application in devices using carbon nanotubes, single molecules, and quantum dots in addition to metal tunnel junction circuits.

The authors acknowledge the financial support provided by the National Science Foundation XYZ-On-A-Chip Program, Contract No. ECS-9980734, and by the Research Corporation through a Research Innovation Award. They thank Bob Hill for processing support.

[1] T. A. Fulton and G. J. Dolan, Phys. Rev. Lett. **59**, 109 (1987).
[2] *Single Charge Tunneling*, edited by H. Grabert and M. H. Devoret, NATO ASI Series, No. 294 (Plenum, New York, 1992).
[3] A. N. Korotkov, Phys. Rev. B **49**, 10381 (1994).
[4] J. Pettersson, P. Wahlgren, P. Delsing, D. B. Haviland, T. Claeson, N. Rorsman, and H. Zirath, Phys. Rev. B **53**, R13272 (1996).
[5] E. H. Visscher, J. Lindeman, S. M. Verbrugh, P. Hadley, J. E. Mooij, and W. van der Vleuten, Appl. Phys. Lett. **68**, 2014 (1996).
[6] R. J. Schoelkopf, P. Wahlgren, A. A. Kozhevnikov, P. Delsing, and D. E. Prober, Science **280**, 1238 (1998).
[7] A. N. Cleland and M. L. Roukes, Nature (London) **392**, 160 (1998).
[8] M. P. Blencowe and M. N. Wybourne, Appl. Phys. Lett. **77**, 3845 (2000).
[9] J. M. Martinis, M. H. Devoret, and J. Clarke, Phys. Rev. B **35**, 4682 (1987).
[10] R. J. Fitzgerald, J. M. Hergenrother, S. L. Pohlen, and M. Tinkham, Phys. Rev. B **57**, 9893 (1998).
[11] P. K. Tien and J. P. Gordon, Phys. Rev. **129**, 647 (1963).
[12] K. Uchida, K. Matsuzawa, J. Koga, R. Ohba, S. Takagi, and A. Toriumi, Jpn. J. Appl. Phys., Part 1 **39**, 2321 (2000).

Thermal conductance and electron-phonon coupling in mechanically suspended nanostructures

C. S. Yung, D. R. Schmidt, and A. N. Cleland[a)]
Department of Physics and iQUEST, University of California at Santa Barbara, Santa Barbara, California 93106

(Received 18 February 2002; accepted for publication 9 May 2002)

We have fabricated and characterized the principal thermal properties of a mechanically suspended nanostructure, consisting of a micron-scale suspended GaAs island, upon which we have defined superconductor-insulator-normal metal tunnel junctions. The tunnel junctions allow for sensitive thermometry and heating of the electrons in a thermally isolated normal metal element, permitting the determination of the low-temperature thermal conductance of the legs that support the GaAs island, as well as the low-temperature electron-phonon coupling. This device forms the basis of a nanoscale bolometric detector, whose optical performance can be estimated from these measurements. © *2002 American Institute of Physics.* [DOI: 10.1063/1.1491300]

It has recently become possible to fabricate fully suspended, three-dimensional integrated devices that can be used for sensitive measurements of energy and thermal transport in nanostructures. Recent experiments have measured the low temperature thermal conductance of submicron single crystal GaAs wires,[1] in the range of 1–10 K, as well as the quantum of thermal conductance of a suspended polycrystalline silicon nitride membrane,[2] in the range of 0.1–10 K. A challenging problem is temperature measurement of the suspended device. Tighe *et al.*[1] relied on the temperature dependence of the zero-bias resistance of an n^+-doped GaAs resistor, while Schwab *et al.*[2] used a dc superconducting quantum interference device to monitor the Johnson–Nyquist noise in a normal metal film. An alternate approach is to employ a superconductor-insulator-normal metal (SIN) tunnel junction as an electron thermometer. These have been used for measuring the thermal conductivity of large-scale suspended silicon nitride membranes,[3] as well as for electronic refrigeration.[4–6] SIN tunnel junctions have also been used as sensitive probes of the electron energy distribution in mesoscopic metallic systems.[7] Here we demonstrate the integration of SIN tunnel junctions with a nanoscale suspended single-crystal GaAs structure, allowing us to measure the electron-phonon coupling in a normal metal film on the suspended structure, as well as measure the phonon thermal conductance through the supporting legs. Our device can be applied to infrared bolometry.

The device was fabricated from a GaAs/AlGaAs heterostructure consisting of a 200 nm GaAs top layer and a 400 nm $Al_{0.7}Ga_{0.3}As$ sacrificial layer, on a bulk GaAs substrate. The lateral dimensions of the mechanical structure were defined using electron-beam lithography to pattern an etch mask, used for a timed anisotropic reactive ion etch of the GaAs heterostructure. We used $SiCl_4$, flowing at 10 sccm at a pressure of 3 mTorr, with a rf power of 100 W, to etch to a depth of 400 nm. The structure is shown in Fig. 1; the six supporting legs are $0.2\times0.2\times3\ \mu m^3$ and the central GaAs island is $0.2\times5\times6\ \mu m^3$. The AlGaAs layer was removed with a timed wet etch in 7% hydrofluoric acid, undercutting the island and six legs. The tunnel junction circuit was defined on the surface of the suspended structure, using a second step of electron-beam lithography to create a stencil mask for angled shadow evaporation. These included a pair of SIN tunnel junctions connected back-to-back in a SINIS pair configuration, and a separate SINIS pair with two ohmic superconductor-normal metal (SN) contacts to the center normal metal element. The tunnel junctions were made by first evaporating 100 Å of Al, perpendicular to the sample surface, and oxidizing in 200 mTorr of O_2 for 3 min, forming the superconducting-insulating connections for the SIN junctions; the oxidation time determines the normal state junction resistance (R_N). A second evaporation of 100 Å of Al, at 45° to the sample surface, formed the superconducting connections for the SN contacts. A final evaporation at −45° of 600 Å of Cu completed the tunnel junctions. Only (superconducting) Al was deposited on the support legs, minimizing the thermal conductance (see Fig. 1). The tunnel junctions can

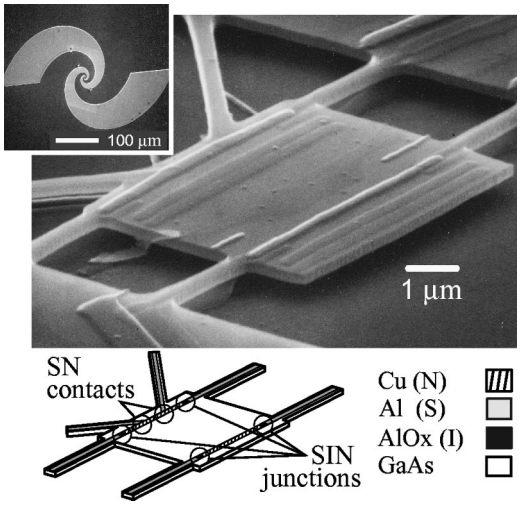

FIG. 1. Micrograph of suspended structure, with 1 μm scale bar. Top left: Log spiral antenna for coupling radiation to the device. Bottom: Schematic of device, indicating the GaAs suspended island, the six supporting legs, the SIN tunnel junctions and the ohmic SN contacts.

a)Electronic mail: cleland@iquest.ucsb.edu

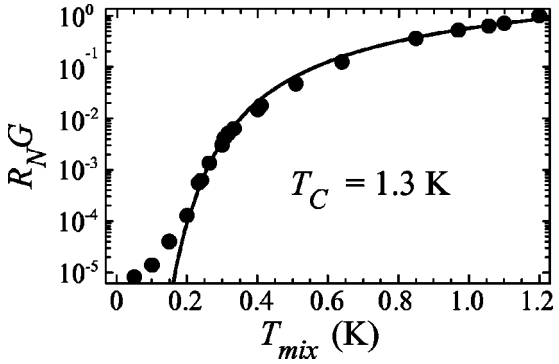

FIG. 2. Normalized zero-bias conductance G of one SNIS tunnel junction, as a function of T_{mix}. Conductance is in units of the normal state resistance R_N, and T_{mix} was measured by a calibrated thermometer. Solid line is a BCS fit to the data.

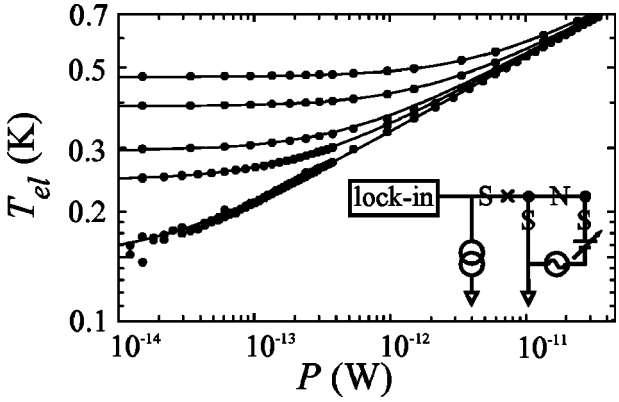

FIG. 3. Electron temperature T_{el} measured as a function of power P dissipated in the normal metal, measured at $T_{\mathrm{mix}}=0.025$, 0.24, 0.3, 0.4, and 0.5 K (indicated by the intercept). The 0.025 K data intercept T_{el} at 0.15 K; solid lines are fits to the data. Inset is a diagram of the measurement setup.

be used as SINIS junction pairs, or, using the SN contacts, as single SNIS junctions.

Electrical contacts to the device were made with Au wire bonds. The device was mounted in a stainless steel can thermally anchored to the mixing chamber of a dilution refrigerator, with a base temperature of 25 mK. All electrical connections to the sample were extensively filtered at room temperature, at the 1 K pot, and at the mixing chamber with π filters, three pole RC filters and stainless steel powder filters.

We calibrated the SINIS junction pairs as electron thermometers by measuring the zero-bias conductance $G=dI/dV(V_{\mathrm{dc}}=0)$ as a function of the mixing chamber temperature T_{mix}. Figure 2 shows the measured normalized conductance $R_N G$ of one of the SNIS pairs, with $R_N=20\ \mathrm{k}\Omega$. The other SINIS pair was very similar, with $R_N=130\ \mathrm{k}\Omega$. Also shown is a one-parameter fit to Bardeen–Cooper–Schrieffer (BCS) theory,[8] giving a transition temperature of $T_c=1.3$ K, that of bulk aluminum. Measurements below 0.2 K deviate from the BCS theory, possibly due to multiple Andreev reflections in the normal section of the SINIS pair,[9] or an indication of sufficient spurious radiation that the electrons do not cool to below 150 mK, due to the small volume of Cu ($\Omega=6\times0.3\times0.06\ \mu\mathrm{m}^3$ of Cu). Bulk electron-phonon coupling theory indicates that for this volume, an ambient power of 10^{-14} W is sufficient to heat the electrons to $T_{el}=150$ mK, for an island phonon temperature $T_{\mathrm{island}}\approx T_{\mathrm{mix}}=25$ mK.[10] We note that the measurement-induced heating of the electron gas is negligible, as measurements were done with an applied power of only $\approx10^{-17}$ W.

We measured the electron-phonon coupling by passing a dc current through the two SN contacts, heating the normal metal, and monitoring the electron temperature T_{el} using one of the SNIS junctions, as shown in the inset of Fig. 3. The SIN junction, located 5 μm from the dc injection point, is ac biased to allow a lock-in measurement of the zero-bias conductance extracting T_{el} from the fit in Fig. 2. Negligible measurement power was dissipated. Figure 3 shows T_{el} as a function of power P, for different mixing chamber temperatures T_{mix}. The solid lines are fits of the form $P=\Sigma\Omega(T_{el}^n-T_{\mathrm{island}}^n)$, with $n=4.84$ and $\Sigma=2\times10^9\ \mathrm{W/m^3\,K^{4.84}}$, for $T_{\mathrm{mix}}=25$ mK, in agreement with previous measurements;[10–12] bulk theory predicts $n=5$ and $\Sigma\approx0.2-2\times10^9\ \mathrm{W/m^3\,K^5}$. Measurements at other T_{mix} yield similar values for n and Σ. Calculations of the acoustic mismatch[13] between the Cu (T_{latt}) and the GaAs (T_{island}) phonon gases predict $T_{\mathrm{latt}}>T_{\mathrm{island}}$, which results in a reduced fit value n. However, the applicability of acoustic mismatch theory is debatable, as the phonon modes in the Cu film are effectively two-dimensional below 1 K.[14] Note that we will identify the island phonon temperature T_{island} with T_{mix}.

The thermal conductance of the support legs was measured by dc biasing one of the SINIS pairs, and measuring the corresponding rise in T_{island} using an electrically isolated SNIS junction. The heating power deposited in the normal Cu section (C_1) of the first SINIS pair (see inset of Fig. 4) heats the island phonon gas, and is then transmitted through the legs to the bulk substrate. The power dissipated is $P=I(V-2\Delta/e)$, using the measured current I and voltage V across the heater SINIS pair, assuming quasiparticle relaxation to the gap ($\Delta=180\ \mu$eV) as the dominant heating process, with negligible subsequent recombination.[15] T_{island} is inferred from the electron temperature of the normal Cu section (C_2) of the SNIS thermometer, using the previously determined electron-phonon coupling. The measured thermal conductance is shown in Fig. 4, for $T_{\mathrm{mix}}=25$ and 50 mK. The solid line is a fit to the data of the form $P=\alpha(T_{\mathrm{island}}^4$

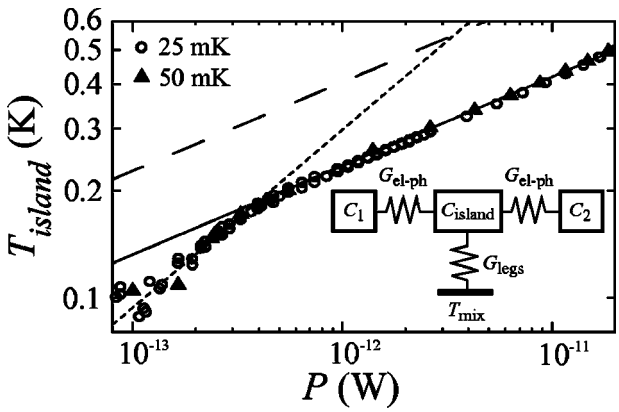

FIG. 4. Island temperature T_{island} as a function of power P dissipated in the island phonon gas, measured at $T_{\mathrm{mix}}=25$ mK (circles) and 50 mK (triangles). Solid line is a fit to the data, yielding a phonon mean free path $\Lambda=7.7\ \mu$m. The long dash line is for $\Lambda=1\ \mu$m, for comparison. The quantum of thermal conductance for six legs is indicated by the short dash line.

$-T_{\mathrm{mix}}^4$) with $\alpha = 3.3\times10^{-10}$ W/K^4. This corresponds to a mean free path $\Lambda = 7.7\ \mu$m,[16] indicating that the phonons undergo primarily specular (rather than diffuse) reflections within the legs.[1] Also plotted (short dashes) is the quantum of thermal conductance[2,17] for six legs, $6\times4\times\mathcal{G}_0 = 8\pi^2k_B^2T/h$. The data agree well with the bulk theory, crossing over to the quantum limit at ~170 mK. Note the large phonon mean free path in our device masks the transition to the quantum limit; we have also plotted the bulk thermal conductance for $\Lambda = 1\ \mu$m (long dashes), which would make the transition to the quantum limit at 550 mK. In addition, the thermal conductance of the legs is significantly larger than the electron-phonon effective conductance, so the assumption that $T_{\mathrm{island}} \approx T_{\mathrm{mix}}$ in the electron-phonon heating measurements is a good one.

We can estimate the performance of this device as a bolometric detector, assuming an operational temperature of 100 mK. Antenna-coupled infrared power heats the electrons in C_2, through the two SN contacts, and the resulting temperature rise in C_1 is detected with a SINIS pair (see Fig. 4). We take the electron heat capacitances $C_1 = C_2 \approx 7.4\times10^{-19}$ J/K at $T = 0.1$ K,[18] and for the island phonons $C_{\mathrm{island}} \approx 1.0\times10^{-20}$ J/K. The thermal conductance between the electrons in C_1 and C_2 and the island phonons is $G_{el\text{-}ph} \approx 1.1\times10^{-14}$ W/K, and the phonon thermal conductance of the support legs is $G_{\mathrm{legs}} \approx 1.5\times10^{-13}$ W/K. The dominant thermal noise source is due to the finite value of $G_{el\text{-}ph}$. The estimated noise equivalent power (NEP) at low frequencies is $\mathrm{NEP} = (4k_BT^2G_{el\text{-}ph})^{1/2} \approx 7\times10^{-20}$ W/Hz$^{1/2}$. Current noise from the first-stage amplifier is a significant additional contribution for this device, due to the high zero-bias resistance $\sim10^8\ \Omega$, limiting the effective NEP to $\approx4\times10^{-17}$ W/Hz$^{1/2}$.[19] We are investigating alternative approaches to reading out the device, using a single-electron transistor as a first-stage amplifier.

The authors acknowledge the financial support provided by NASA Office of Space Science under Grant No. NAG5-8669 and the Army Research Office under Award No. DAAD-19-99-1-0226. We thank Bob Hill for processing support.

[1] T. S. Tighe, J. M. Worlock, and M. L. Roukes, Appl. Phys. Lett. **70**, 2687 (1997).
[2] K. C. Schwab, E. A. Henriksen, J. M. Worlock, and M. L. Roukes, Nature (London) **404**, 974 (2000).
[3] M. M. Leivo and J. P. Pekola, Appl. Phys. Lett. **72**, 1305 (1998).
[4] M. Nahum, T. M. Eiles, and J. M. Martinis, Appl. Phys. Lett. **65**, 3123 (1994).
[5] M. M. Leivo, J. P. Pekola, and D. V. Averin, Appl. Phys. Lett. **68**, 1996 (1996).
[6] J. P. Pekola, A. J. Manninen, M. M. Leivo, K. Arutyunov, J. K. Suoknuuti, T. I. Suppula, and B. Collaudin, Physica B **280**, 485 (2000).
[7] H. Pothier, S. Guéron, N. O. Birge, D. Esteve, and M. H. Devoret, Phys. Rev. Lett. **79**, 3490 (1997).
[8] L. Solymar, *Superconductive Tunnelling and Applications* (Chapman and Hall, London, 1972).
[9] A. F. Volkov, A. V. Zaitsev, and T. M. Klapwijk, Physica C **210**, 21 (1993).
[10] F. C. Wellstood, C. Urbina, and J. Clarke, Phys. Rev. B **49**, 5942 (1994).
[11] M. L. Roukes, M. R. Freeman, R. S. Germain, R. C. Richardson, and M. B. Ketchen, Phys. Rev. Lett. **55**, 422 (1985).
[12] A. H. Steinbach, J. M. Martinis, and M. H. Devoret, Phys. Rev. Lett. **76**, 3806 (1994).
[13] E. T. Swartz and R. O. Pohl, Rev. Mod. Phys. **61**, 605 (1989).
[14] $T \approx \pi v_s\hbar/(k_Bd) \approx 1.4$ K for $v_s = 3710$ m/s and $d = 60$ nm.
[15] H. Kinder, Phys. Rev. Lett. **28**, 1564 (1972).
[16] Using $\kappa = 1/3cv_s\Lambda$, with $v_s = 3710$ m/s and a Debye temperature of 345 K. We note Λ is longer than the legs.
[17] L. G. C. Rego and G. Kirczenow, Phys. Rev. Lett. **81**, 232 (1998).
[18] Estimated from the specific heat of Cu.
[19] Estimated from the voltage responsivity of 0.4 mV/K and a current noise of 10^{-15} A/Hz$^{1/2}$.

Piezoelectric displacement sensing with a single-electron transistor

R. Knobel and A. N. Cleland[a)]
Department of Physics and iQUEST, University of California at Santa Barbara, Santa Barbara, California 93106

(Received 30 May 2002; accepted for publication 23 July 2002)

We propose a displacement sensing scheme for rf mechanical resonators made from GaAs, based on detecting the piezoelectrically induced charge. By using a single-electron transistor to detect the charge, we calculate that a significantly higher displacement sensitivity can be achieved than by using capacitive displacement sensing, primarily due to the strong piezoelectric coupling strength. We estimate a displacement sensitivity of order 10^{-17} m/Hz$^{1/2}$ for a 1 GHz GaAs resonator. Our model solves the coupled electromechanical response self-consistently, including the effects of both dissipative and reactive electronic circuit elements on the resonator behavior. © *2002 American Institute of Physics.* [DOI: 10.1063/1.1507616]

There is significant interest in developing detection schemes that might achieve quantum-limited displacement sensing of nanometer-scale resonators.[1–3] At present, one of the most promising approaches is to use a single-electron transistor (SET) capacitively coupled to a flexural beam resonator.[1,4] In this scheme, the flexural beam is biased with a constant voltage, so that its motion changes the charge coupled to a nearby SET, hence changing the current through the SET. Increasing the voltage applied to the beam leads to larger coupled charge signals, but also increases the back-action coupling between the SET and the beam. For a model cantilever and SET, applying the optimal bias voltage yields[1] a displacement sensitivity of 4×10^{-16} m/Hz$^{1/2}$.

Here, we demonstrate that if instead the resonator is fabricated from a piezoelectric material, such as GaAs,[3] AlGaAs,[5] or AlN,[6] and the SET is configured to sense the piezoelectric voltage developed when the beam flexes, then a significantly higher displacement sensitivity can be achieved; we calculate a noise figure of 5×10^{-17} m/Hz$^{1/2}$, dominated equally at peak sensitivity by the current and back action noise of the SET. This technique is similar to that of Beck *et al.*,[7] where an integrated field-effect transistor was used to sense strain. Here, the superior noise performance of the SET permits several orders of magnitude improvement in the displacement sensitivity.

In Fig. 1(a), we show the heterostructure design from which the device could be fabricated, and in Fig. 1(b), a schematic view of the doubly clamped resonator that includes the SET. The heterostructure includes a two-dimensional electron gas (2DEG) 50 nm below its surface, which acts as a ground plane for the actuation and detection signals. The device is fabricated using a sequence of electron-beam lithography, etching, and metal deposition to define the SET and the mechanical resonator.[4] The model resonator, with dimensions $L\times w\times t=0.64\times0.2\times0.1$ μm^3, is designed to operate at the fundamental flexural frequency $\omega_1/2\pi=1.027(E/\rho)^{1/2}(t/L^2)=1.0$ GHz, using Young's modulus $E=85$ GPa and $\rho=5.32$ g/cm^3 for GaAs.

Flexure of the resonator in the z direction, with the $\langle100\rangle$ crystal axis aligned along z, will generate a piezoelectric polarization density $\mathbf{P}$ along z, with the polarization amplitude proportional to the distance from the midpoint ($z=0$) of the beam.[8] The polarization induces a screening charge on the detection electrode, which can be detected by the SET. Conversely, when an electric field is applied between the actuation electrode and the 2DEG, along z, the beam will respond with an in-plane strain, which couples to the fundamental flexural mode. For a neutral axis displacement $U(x)$, the polarization density $P(x,z)$ a height z above the neutral axis is $P(x,z)=0.315d_{14}EzU''(x)$.[9] Here, $d_{14}=3.03$ pC/N is the relevant piezoelectric constant for $Al_{0.3}Ga_{0.7}As$.[5,8] For the fundamental flexural mode, the polarization density is largest at the beam surface $z=t/2$, and is maximum at the beam ends $x=\pm L/2$, crossing zero at $x=\pm0.276L$, and reaching a secondary (negative) maximum at the beam center $x=0$. This polarization induces a charge q on the detection electrode, which extends from the beam end to the zero-crossing point, over the full width w of the beam. The induced charge is the integral of the polarization at the surface, $P(x,t/2)$, over the area of the detection electrode.

The circuit connected to the detection electrode will affect the electromechanical response of the resonator (a somewhat related effect was described by Schwab).[10] The response can be determined by solving the coupled electrical

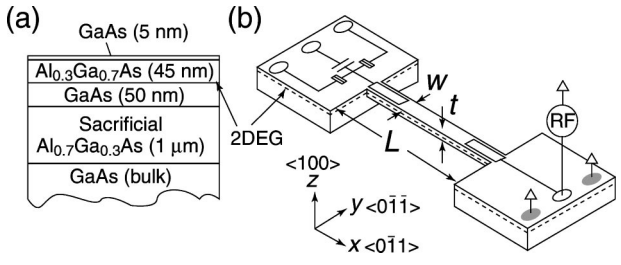

FIG. 1. (a) GaAs/AlGaAs heterostructure design; layer thicknesses indicated in parentheses. A 2DEG is formed at the GaAs-(modulation-doped) $Al_{0.3}Ga_{0.7}As$ interface. Vertical axis is not to scale. (b) Sketch of device; the resonator has dimensions $L\times w\times t$, with the SET situated at one end of the beam, coupled to a detection electrode, with an actuation electrode that is driven by a rf source at the other end. V_g is the voltage applied to the gate of the SET, and V_{ds} the drain–source bias voltage. The GaAs crystal axes, and the geometric axes, are indicated.

a)Electronic mail: cleland@iquest.ucsb.edu

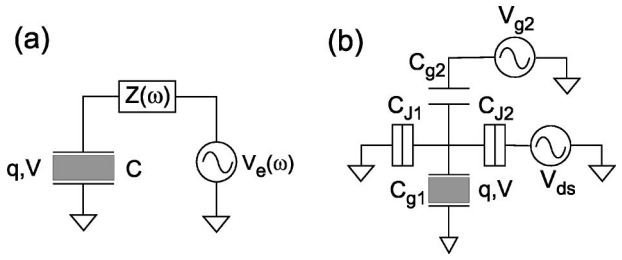

FIG. 2. (a) Nyquist equivalent circuit connected to the piezoelectric detection electrode, with impedance $Z(\omega)$ and voltage source $V_e(\omega)$. (b) Circuit model for detection electrode as the island of the SET.

and mechanical equations of motion self-consistently. In a piezoelectric material, the stress, strain, electric field, and polarization density provide a complete description of the state of the system, and any pair of these can be chosen as the independent variables, the other two determined through the linear piezoelastic relations.[11] In our case, we consider only the fundamental flexural mode for the resonator, electrically coupled through the detection electrode shown in Fig. 1(b), and we simplify the full tensor relations to those involving the force F coupled to the fundamental mode shape, the displacement $\mathcal{U}=U(0)$ of the beam midpoint, and the charge q and voltage V induced on the detection electrode. These are then related to one another through the relations[9]

$$\begin{pmatrix} F \\ q \end{pmatrix} = \begin{pmatrix} k & a \\ a & C \end{pmatrix} \quad \begin{pmatrix} \mathcal{U} \\ V \end{pmatrix}. \tag{1}$$

Here, $k=M\omega_1^2$ is the effective spring constant for a beam mass M, C is the geometric capacitance associated with the detection electrode, and a is a scaled piezoelectric constant that relates the force to an applied voltage, for fixed displacement, and the induced charge to a displacement, for a fixed voltage. The material symmetries make the constants for these two relations equal. For the fundamental mode of our model GaAs/AlGaAs flexural resonator, we have $k=2700$ N/m, $C=0.448\varepsilon\varepsilon_0(wL/t)=65$ aF, and $a=0.771d_{14}E(wt/L)=6.2\times10^{-9}$ C/m.

The mechanical resonator response includes inertial and dissipative terms in the displacement $\mathcal{U}$, and we model the electrical circuit as a Nyquist equivalent circuit with impedance $Z(\omega)$ and voltage $V_e(\omega)$, as shown in Fig. 2(a). The coupled equations of motion, using Eq. (1), are then given by

$$\left.\begin{aligned} \left(k-M\omega^2+iM\frac{\omega\omega_1}{Q_m}+\frac{i\omega Z}{1+i\omega CZ}a^2\right)\mathcal{U} \\ =F_D+\frac{1}{1+i\omega CZ}aV_e, \\ q=\frac{a\mathcal{U}+CV_e}{1+i\omega CZ} \end{aligned}\right\}. \tag{2}$$

For a real impedance $Z(\omega)=R$, at low frequencies $\omega RC\ll1$, the circuit damps the resonator, giving a net quality factor $1/Q_t=1/Q_m+1/Q_{\rm el}$ with the electrical contribution $Q_{\rm el}=M\omega_1/a^2R$. This type of damping has been observed with an atomic force microscope cantilever in carbon nanotube-based SETs.[12] If the force F_D is the thermomechanical noise at temperature T, with *classical* spectral density $S_F(\omega)=2k_BTM\omega_1/\pi Q_m$, and the resistor has Nyquist

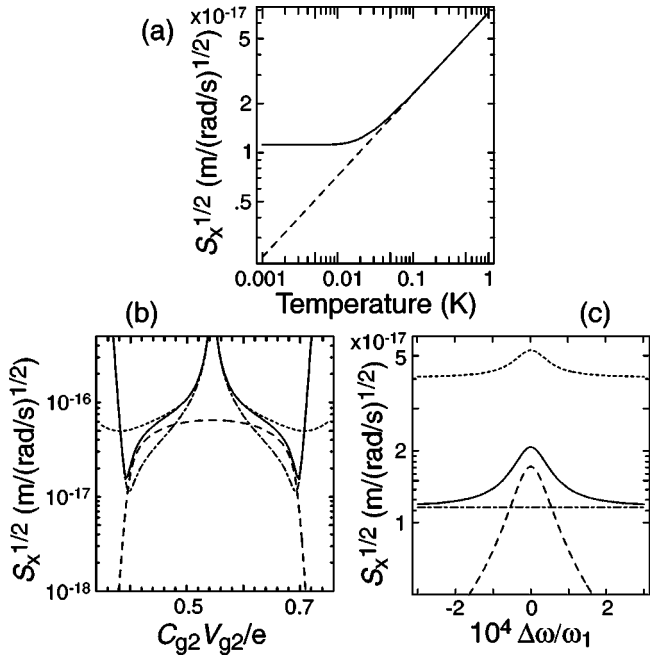

FIG. 3. (a) Displacement noise as a function of temperature, at the beam resonance frequency for the model beam. The dashed line is the classical thermal noise, while the solid line is the Callen–Welton noise. (b) Displacement noise as a function of gate voltage, at the beam resonance frequency for the model SET with $V_{\rm ds}=0.3e/C_\Sigma$ at 10 and 100 mK. (c) Displacement noise at $V_{g2}=0.4e/C_{g2}$ as a function of frequency detuning from the beam resonance, showing the resonance response effect on the back-action noise. In plots (b) and (c), dashed lines are back-action noise S_X^B, dashed–dotted lines readout noise S_X^R, and solid lines total noise for 10 mK while dotted lines indicate the total noise for 100 mK.

voltage noise at temperature T, $S_V(\omega)=2k_BTR/\pi$, the effective force noise from Eq. (2) is that corresponding to thermomechanical force noise for a quality factor Q_t. The *classical* spectral density of the displacement noise $S_X^T(\omega)$ at temperature T, including both the thermomechanical and electrical noise, is given by

$$S_X^T(\omega)=\frac{1}{(\omega_1^2-\omega^2)^2+(\omega\omega_1/Q_t)^2}\frac{2k_BT\omega_1}{\pi MQ_t}. \tag{3}$$

On resonance $\omega=\omega_1$, the displacement noise is $S_X^T(\omega)^{1/2}=\sqrt{2k_BTQ_t/\pi M\omega_1^3}$. For mechanical resonators at low temperatures, with $\hbar\omega_1\gtrsim k_BT$, we should use the Callen–Welton quantum formula for the noise,[13] $S_F(\omega)=(\omega_1/\pi MQ_t)\hbar\omega\coth(\hbar\omega/2k_BT)$, replacing the last ratio in Eq. (3). The temperature dependence of this displacement noise on resonance for the model beam with an assumed quality factor Q_t of 10^4 is plotted in Fig. 3(a). The quantum limited displacement noise of this beam is 1.1×10^{-17} m/(rad/s)$^{1/2}$.

At high frequencies $\omega RC\gg1$, the electrical circuit stiffens the mechanical response, shifting the resonance frequency without adding dissipation. In this limit, the voltage noise is reduced by the RC rolloff of the circuit.

For capacitive loading of the resonator, with $Z=1/i\omega C_e$, the external circuit will only act to stiffen the effective mechanical response, so that the resonance frequency shifts to $\omega_1'^2=\omega_1^2+a^2/MC_e$.

We now analyze the displacement sensitivity of the piezoelectric resonator coupled to a SET, whose circuit is

shown in Fig. 2(b). In order to measure the motion of the beam at the resonant frequency, the SET can either be used with a resonant tank circuit[14] (termed rf-SET), or can be used as a rf mixer;[4] in the latter implementation, operation at frequencies up to and above 1 GHz is achievable. These frequency-shifting techniques should not significantly modify the noise analysis presented here.

The displacement sensitivity is limited by two effects: The current noise of the SET $S_I(\omega)$ adds to the detected displacement signal, generating a spectral noise density $S_X^R(\omega)$ referenced to the beam displacement, which we term the readout noise. In addition, the fluctuation in the number of electrons on the SET center island causes the island voltage to fluctuate. This voltage noise actuates the beam resonator, providing a source of back-action noise, with displacement spectral density $S_X^B(\omega)$ (again referred to the beam displacement). Semiclassical expressions for the noise of a SET have been developed by Korotkov;[15] here, we use the approximate model developed by Zhang and Blencowe,[16] which applies in the low-temperature limit $k_BT \ll \mathrm{eV}_{ds}$, so that only terms involving n and $n+1$ electrons on the SET island are kept.

With the resonator coupled to one input gate C_{g1} of the SET, the input impedance is that of the other island capacitances in parallel, $Z(\omega)=1/i\omega C_\Sigma'$ with total island capacitance $C_\Sigma = C_{J1}+C_{J2}+C_{g1}+C_{g2} = C_\Sigma' + C_{g1}$. The total displacement noise spectral density $S_X(\omega)$, referred to the beam displacement, is the sum of the contributions from the readout and back-action noise,

$$S_X(\omega) = S_X^R(\omega) + S_X^B(\omega), \tag{4}$$

where we ignore correlations between these two noise sources. The readout noise $S_X^R(\omega)$ is related to the SET current noise $S_I(\omega)$ by the displacement responsivity of the SET,

$$S_X^R(\omega) = S_I(\omega)/(dI_{ds}/d\mathcal{U})^2, \tag{5}$$

where $dI_{ds}/d\mathcal{U}$ is the derivative of the SET current with midpoint displacement $\mathcal{U}$. From Eq. (2), we can relate the SET-coupled charge $q(\mathcal{U})$ to the displacement $\mathcal{U}$ for fixed voltage V_e, $dq/d\mathcal{U} = a/(1+C_{g1}/C_\Sigma')$, and using the form for the SET current-charge dependence $I_{ds}(q)$ we can determine the readout noise S_X^R. The back-action noise can be evaluated from the relation between displacement $\mathcal{U}$ and voltage V_e for fixed drive force F_D; the voltage V_e, equal to the SET center island voltage, is related to the number n of electrons on the center island by $V_e = (en+\tilde{q})/C_\Sigma$, where $\tilde{q}$ is the charge bias applied to the SET, assumed noiseless. From the expression[16] for the spectral density of the number noise $S_n(\omega)$, we then have the spectral density of voltage noise $S_V(\omega) = (e/C_\Sigma)^2 S_n(\omega)$, and from Eq. (2), we can evaluate the corresponding back-action displacement noise S_X^B, with

$$S_X^B(\omega) = \frac{1}{(\omega_1'^2-\omega^2)^2 + (\omega\omega_1/Q)^2}\left(\frac{aC_\Sigma'}{MC_\Sigma}\right)^2 S_V(\omega), \tag{6}$$

with the resonance frequency shifted by the circuit capacitance.

In Fig. 3, we display the two contributions as well as the total noise, calculated for an optimized SET with junction resistances $R_{J1}=R_{J2}=100\ \mathrm{k}\Omega$, junction capacitances $C_{J1}=C_{J2}=0.15$ fF, and gate capacitances $C_{g1}=C_{g2}=65$ aF, at temperatures of 10 and 100 mK.

The detection of the piezoelectrically induced charge in a mechanical resonator with a SET has been shown to be a prime candidate for nearly quantum-limited displacement sensing. Piezoelectric detection is additionally attractive because the piezoelectric signals scale favorably to the small, stiff resonators needed to approach the regime where $\hbar\omega_1 \gtrsim k_BT$. In both the capacitive and piezoelectric schemes, the detection of deviations from the classical motion will be difficult for nanomechanical resonators with $\omega_1/2\pi < 1$ GHz.

The authors acknowledge the financial support provided by the National Science Foundation XYZ-On-A-Chip Program, Contract No. ECS-9980734, by the Army Research Office, and by the Research Corporation through a Research Innovation Award.

[1] M. P. Blencowe and M. N. Wybourne, Appl. Phys. Lett. **77**, 3845 (2000).
[2] A. D. Armour, M. P. Blencowe, and K. C. Schwab, Phys. Rev. Lett. **88**, 148301 (2002).
[3] A. N. Cleland, J. S. Aldridge, D. C. Driscoll, and A. C. Gossard, Appl. Phys. Lett. (to be published).
[4] R. Knobel, C. S. Yung, and A. N. Cleland, Appl. Phys. Lett. **81**, 532 (2002).
[5] S. Adachi, J. Appl. Phys. **58**, R1 (1985).
[6] A. N. Cleland, M. Pophristic, and I. Ferguson, Appl. Phys. Lett. **79**, 2070 (2001).
[7] R. G. Beck, M. A. Eriksson, M. A. Topinka, R. M. Westervelt, K. D. Maranowksi, and A. C. Gossard, Appl. Phys. Lett. **73**, 1149 (1998).
[8] J. Söderkvist and K. Hjort, J. Micromech. Microeng. **4**, 28 (1994).
[9] A. N. Cleland and R. Knobel (unpublished).
[10] K. Schwab, Appl. Phys. Lett. **80**, 1276 (2002).
[11] B. Auld, *Acoustic Fields and Waves in Solids*, 2nd ed. (Wiley, New York, 1990).
[12] M. T. Woodside and P. L. McEuen, Science **296**, 1098 (2002).
[13] V. B. Braginsky and F. Y. Khalili, *Quantum Measurement* (Cambridge University Press, Cambridge, UK, 1992).
[14] R. J. Schoelkopf, P. Wahlgren, A. A. Kozhevnikov, P. Delsing, and D. E. Prober, Science **280**, 1238 (1998).
[15] A. N. Korotkov, Phys. Rev. B **49**, 10381 (1994).
[16] Y. Zhang and M. P. Blencowe, J. Appl. Phys. **91**, 4249 (2002).

Noise processes in nanomechanical resonators

A. N. Cleland[a)]
Department of Physics and iQUEST, University of California at Santa Barbara, Santa Barbara, California 93106

M. L. Roukes
Department of Physics, California Institute of Technology, Pasadena, California 91125

(Received 15 February 2002; accepted for publication 18 June 2002)

Nanomechanical resonators can be fabricated to achieve high natural resonance frequencies, approaching 1 GHz, with quality factors in excess of 10^4. These resonators are candidates for use as highly selective rf filters and as precision on-chip clocks. Some fundamental and some nonfundamental noise processes will present limits to the performance of such resonators. These include thermomechanical noise, Nyquist–Johnson noise, and adsorption–desorption noise; other important noise sources include those due to thermal fluctuations and defect motion-induced noise. In this article, we develop a self-contained formalism for treating these noise sources, and use it to estimate the impact that these noise processes will have on the noise of a model nanoscale resonator, consisting of a doubly clamped beam of single-crystal Si with a natural resonance frequency of 1 GHz. © *2002 American Institute of Physics.* [DOI: 10.1063/1.1499745]

I. INTRODUCTION

Nanomechanical resonators are rapidly being pushed to smaller size scales and higher operational frequencies, partly due to potential applications as on-chip high-Q filters and clocks. Such resonators would have the potential for replacing bulk quartz crystals and surface-acoustic wave resonators in technological and precision measurement applications, which require extensive separate circuitry and space requirements. High-frequency resonators have been fabricated from bulk Si,[1] silicon-on-insulator,[2] silicon carbide,[3] silicon nitride,[4] and from polycrystalline Si (poly-Si).[5,6] High resonance frequencies can be achieved using submicron lithography to define doubly clamped beams with relatively large length-to-thickness ratios of $L/t \sim 10-20$. Smaller aspect ratios, with $L/t \sim 2-5$, allow high frequencies to be achieved with less stringent demands on lithographic capability. For these smaller aspect ratios, however, thermoelastic damping begins to become an important source of energy loss and noise, ultimately limiting the quality factor and noise performance.[4,7]

The resonance frequency of a mechanical structure in general scales as $1/L$, where L is the scale of the resonator. As the size scales are reduced and frequencies increased, however, the short-term stability of the resonator will be limited by certain fundamental noise processes.[8] These noise processes include the thermomechanical noise generated by the internal loss mechanisms in the resonator,[9] Nyquist–Johnson noise from the readout circuitry,[10] and adsorption–desorption noise from residual gas molecules in the resonator packaging.[11] Another noise source is due to temperature fluctuations caused by the finite thermal conductance of the resonator;[12] these fluctuations are fundamental to any object with finite heat capacity, and are distinct from environmental thermal drifts that can be controlled using oven-heated packaging, similar to that used for high-precision quartz clocks. Resonators fabricated from polycrystalline materials, such as those including poly-Si and silicon nitride, are also expected to demonstrate noise from anelastic noise processes caused by grain-boundary and point defect motion.[13]

At present, there does not exist a single self-contained formalism for describing the resonance and noise properties of nanomechanical resonators. In the first part of this work, we therefore develop such a formalism, based on the well-known Euler–Bernoulli theory of beams. We hope that this will provide a clear and useful framework for future developments in the field. In the latter part of the work, we use this formalism to calculate the effects of the most significant and fundamental, classical sources of noise on resonator performance. The importance of thermomechanical noise, arising from the nonzero dissipation and temperature of a resonator, has been recognized for some time, and its effects have been included in previous noise analyses of mechanical resonators.[9,14] Other noise sources have also been included in more recent analyses, as mentioned herein. However, our results are not in agreement with the results of these more recent works, in particular, in terms of the magnitude of the impact of the noise, as well as the method of analysis of some of the noise sources, in particular, that of the effect of temperature fluctuations. We have also included a discussion of defect noise, that to our knowledge has not previously been considered.

We do not consider noise or physical limitations produced by particular transducer implementations. Electrostatically driven and detected resonators suffer from surface charge motion; magnetomotive approaches require large stable ambient magnetic fields; optical approaches require stable sources of monochromatic light. We are more concerned with the limitations set by the physics of resonator

a)Electronic mail: cleland@iquest.ucsb.edu

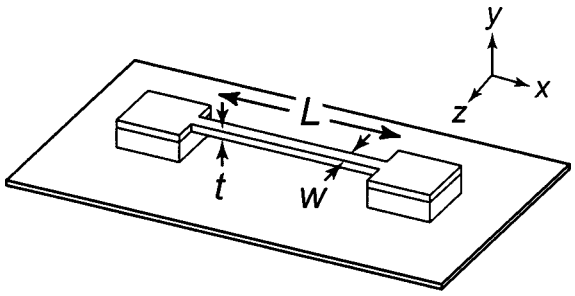

FIG. 1. Doubly clamped beam with length L, width w and thickness t. The end supports are assumed infinitely rigid.

behavior, and transducer approaches should be evaluated separately from these.

II. DOUBLY CLAMPED BEAM RESONATORS

A. Euler–Bernoulli theory

In Fig. 1, we show the structure forming the basis of our calculations: A doubly clamped beam of length L, width w, and thickness t, oriented along the x axis, driven into flexural resonance with displacement along the y axis.

The dynamic behavior of a flexural beam is most easily treated using the Euler–Bernoulli theory, which applies to beams with aspect ratios $L/t \gg 1$.[15] For an isotropic material, the transverse displacement $Y(x,t)$ of the beam centerline (along the y direction), obeys the differential equation

$$\rho A \frac{\partial^2 Y}{\partial t^2}(x,t) = -\frac{\partial^2}{\partial x^2} EI \frac{\partial^2 Y}{\partial x^2}(x,t), \tag{1}$$

where ρ is the material density, $A=wt$ is the cross-sectional area, E is Young's modulus, and $I=wt^3/12$ is the bending moment of inertia. The clamped ends, at $x=0$ and $x=L$, impose the boundary conditions $Y(0)=Y(L)=0$ and $Y'(0)=Y'(L)=0$. The solutions have the form

$$Y_n(x,t) = (C_{1n}(\cos k_n x - \cosh k_n x) + C_{2n}(\sin k_n - \sinh k_n x))\exp(-i\Omega_n t), \tag{2}$$

with eigenvectors k_n satisfying $\cos k_n L \cosh k_n L = 1$. The first four eigenvectors are given by $k_n L = 4.730\,04$, 7.8532, 10.9956, and 14.1372. The angular frequencies Ω_n are given by

$$\Omega_n = \sqrt{\frac{EI}{\rho A}} k_n^2. \tag{3}$$

The fundamental eigenfrequency is given by

TABLE I. Numerical solutions for a doubly clamped beam.

	$n=1$	2	3	4
$k_n L$	4.730 04	7.8532	10.9956	14.1372
ν_n/ν_1	1	2.756	5.404	8.933
C_{1n}/L	−1.0000	−1.0000	−0.9988	−1.0000
C_{2n}/L	0.9825	1.0008	0.9988	1.0000

TABLE II. Parameters for the beam in this calculation.

L (μm)	t (μm)	w (μm)	M (fg)	ν_1 (GHz)	k_1 (μm^{-1})
0.66	0.05	0.05	3.84	1.00	7.17

$$\nu_1 = \Omega_1/2\pi = 1.027\sqrt{\frac{E}{\rho}}\frac{t}{L^2}, \tag{4}$$

and the higher modes are $\nu_n/\nu_1 = 2.756$, 5.404, and 8.933 for $n=2$, 3, and 4.

The eigenfunctions Y_n in Eq. (2) are mutually orthogonal, and we normalize them to the beam length, so that

$$\int_0^L Y_n(x) Y_m(x)\,dx = L^3 \delta_{mn}. \tag{5}$$

The corresponding coefficients C_{1n} and C_{2n} are listed in Table I. An arbitrary solution $Y(x,t)$ to undriven or driven motion can be written

$$Y(x,t) = \sum_{n=1}^{\infty} a_n(t) Y_n(x), \tag{6}$$

where the amplitudes a_n are dimensionless.

The fundamental frequency ν_1 is a function of the material parameters E and ρ as well as the beam dimensions t and L. High frequencies can be achieved by reducing the overall resonator scale, by choosing stiffer and lighter materials, and by reducing the aspect ratio L/t; all three of these approaches are being used, and at present the highest reported frequency is 0.63 GHz, for a SiC beam.[16] For the purposes of this article, we will focus on a single-crystal Si beam with dimensions as given in Table II; the relevant physical properties for Si are given in Table III, all at room temperature. Our calculations are for the fundamental resonance $n=1$.

In the next section, we discuss the anelastic processes that result in a finite quality factor Q for the beam resonance, described within the context of Zener's model for anelastic solids. In that section, we will describe how the Zener model is included in the formalism described so far. In later sections, we discuss other types of noise that are not described within the context of the Zener model; these have to do with parametric changes in the physical properties of the resonator, such as its mass and length, which cause the natural resonance frequency of the resonator to change, but do not necessarily involve energy dissipation. Any single parametric change can be associated with a change in the resonator

TABLE III. Properties for Si at room temperature.

Density	ρ	2330 kg/m^3
Young's modulus	E	1.69×10^{11} N/m^2
Thermal conductivity	κ	1.48 W/cm K
Specific heat	C_V	1.64 J/cm^3 K
Sound speed	c_s	5860 m/s
Phonon mean-free path	ℓ	50 nm
Thermal expansion	α_T	2.8×10^{-6}/K

energy, depending on where in the oscillation cycle the change occurs, but given events that occur randomly over the oscillation period, on average, the energy change is zero. The noise sources we discuss include adsorption–desorption noise due to molecules around the resonator, temperature fluctuations that change the length and longitudinal stress in the resonator, and defect motion within the resonator. The latter can to some extent be included in the Zener model, but some modes of defect motion will not generate intrinsic dissipation but instead give rise to parametric changes.

For these sources of parametric noise, an instantaneous measurement of the response of a resonator, as a function of frequency, would indicate the actual dissipation associated with material losses, while a measurement that takes a nonzero time to complete allows the resonator frequency to fluctuate over the period of the measurement, and would give a response curve that appears to be associated with a higher rate of dissipation than is actually present, due to the spread of resonance frequencies that appear over the course of the measurement. Separating these two effects experimentally is a very challenging but intriguing problem.

B. Dissipation in mechanical resonators

The most significant mechanism for energy loss in a nanomechanical resonator is through intrinsic losses in the beam material, which can be treated using Zener's model for anelastic solids.[13] Other important loss terms include thermoelastic processes,[7] which are negligible for the resonator geometry and dimensions given here, and through the transduction mechanism,[17] which can usually be minimized through design considerations.

In Zener's model, the Hooke's stress–strain relation $\sigma = E\epsilon$, relating the stress σ to the strain ϵ, is generalized to allow for mechanical relaxation in the solid:

$$\sigma + \tau_\epsilon \frac{d\sigma}{dt} = E_R\left(\epsilon + \tau_\sigma \frac{d\epsilon}{dt}\right), \tag{7}$$

where E_R is the relaxed value of Young's modulus. Loads applied slowly generate responses with the relaxed modulus, while rapidly varying loads involve a different value for the modulus.

We consider harmonic stress and strain variations, $\sigma(t) = \sigma e^{i\omega t}$ and $\epsilon(t) = \epsilon e^{i\omega t}$. At low frequencies $\omega\tau \ll 1$, this becomes the standard Hooke's law relation with $E = E_R$. At high frequencies $\omega\tau \gg 1$, the modulus becomes $E = E_U = (\tau_\sigma/\tau_\epsilon)E_R$, the *unrelaxed* Young's modulus. For intermediate frequencies, Young's modulus is complex, of the form

$$E = E_{\text{eff}}(\omega)\left(1 + \frac{i\omega\tau}{1+\omega^2\tau^2}\Delta\right), \tag{8}$$

with mean relaxation time $\tau = (\tau_\sigma\tau_\epsilon)^{1/2}$, fractional modulus difference $\Delta = (E_U - E_R)/E_R$, and effective Young's modulus

$$E_{\text{eff}} = \frac{1+\omega^2\tau^2}{1+\omega^2\tau_\epsilon^2}E_R. \tag{9}$$

Equation (8) implies that the stress σ will include a component that is 90° out of phase with the strain ϵ, which causes energy loss at a rate proportional to Δ. For small Δ, we define the quality factor Q as the ratio of the imaginary to the real part of E:

$$Q^{-1} = \frac{\omega\tau}{1+\omega^2\tau^2}\Delta. \tag{10}$$

We then use the effective Young's modulus E_{eff} in the Euler–Bernoulli formula, Eq. (1) at frequency ω,

$$\omega^2\rho A Y(x) = E_{\text{eff}}(\omega) I\left(1 + \frac{i}{Q}\right)\frac{\partial^4 Y}{\partial x^4}(x). \tag{11}$$

The spatial solutions $Y(x)$ are the same as for Eq. (1), but the dispersion relation giving the damped eigenfrequencies Ω_n' in terms of the undamped frequencies Ω_n is

$$\Omega_n' = \left(1 + \frac{i}{2Q}\right)\Omega_n, \tag{12}$$

for small dissipation Q^{-1}. The imaginary part of Ω_n' implies that the nth eigenmode will decay in amplitude as $\exp(-\Omega_n t/2Q)$.

C. Driven damped beams

We now add a harmonic driving force $F(x,t) = f(x)\exp(i\omega_c t)$, where $f(x)$ is the position-dependent force per unit length. The force is uniform across the beam cross section and directed along y, and the carrier frequency ω_c is close to Ω_1. The equation of motion is[15]

$$\rho A\frac{\partial^2 Y}{\partial t^2} + EA\frac{\partial^4 Y}{\partial x^4} = f(x)e^{i\omega_c t}. \tag{13}$$

We solve this equation for long times, $\Omega_1 t/Q \gg 1$, so any transients damp out. The solution then has the form $Y(x,t) = Y(x)e^{i\omega_c t}$. The amplitude $Y(x)$ may be complex, so that the motion is not necessarily in phase with the force F. Expanding the displacement in terms of the eigenfunctions Y_n,

$$-\omega_c^2\rho A\sum_{n=1}^{\infty} a_n Y_n(x) + EA\sum_{n=1}^{\infty} a_n\frac{\partial^4 Y_n}{\partial x^4} = f(x). \tag{14}$$

Using the defining relation for the eigenfunctions, Eq. (1), the dispersion relation, Eq. (12), and the orthogonality relations, Eq. (5), this can be written

$$(\Omega_m'^2 - \omega_c^2)a_m = \frac{1}{\rho A L^3}\int_0^L Y_m(x)f(x)dx, \tag{15}$$

for each term m in the expansion. For ω_c close to Ω_1, only the $m=1$ term in Eq. (15) has a significant amplitude, given by

$$a_1 = \frac{1}{\rho A L^3}\frac{1}{\Omega_1^2 - \omega_c^2 + i\Omega_1^2/Q}\int_0^L Y_1(x)f(x)dx, \tag{16}$$

for small dissipation Q^{-1}.

We now take a uniform force, $f(x) = f$. The integral in Eq. (16) is then

$$\eta_1 = \frac{1}{L^2}\int_0^L Y_1(x)dx = 0.8309. \tag{17}$$

The amplitude is then

$$a_1 = \frac{\eta_1}{\Omega_1^2 - \omega_c^2 + i\Omega_1^2/Q}\frac{f}{M}, \tag{18}$$

where $M=\rho AL$ is the mass of the beam, and the corresponding displacement of the beam is $Y(x,t)=a_1Y_1(x)\exp(i\omega_c t)$.

If the force distribution $f(x)$ is instead chosen to be proportional to the eigenfunction $Y_1(x)$, the integral Eq. (16) is unity, so that η_1 in Eq. (18) is replaced by the number 1.

We point out that the response function, Eq. (18), while similar to that of a damped, one-dimensional harmonic oscillator, differs slightly in the Q-dependent denominator, but the difference is only apparent for small values of Q: For values of Q greater than 15, the fractional difference at any frequency is less than 1%.

III. NOISE IN DRIVEN DAMPED BEAMS

Systems that dissipate energy are necessarily sources of noise; the converse is also often true. This is the basic statement of the fluctuation–dissipation theorem, and is best known in relation to electrical circuits, where it is termed the Nyquist–Johnson theorem. An electrical circuit element with an electrical impedance $Z(\omega)$ that has a nonzero real part, $R(\omega)=\mathrm{Re}\,Z(\omega)$, will be a source of noise, that is, of fluctuations in the voltage $V(t)$ across the impedance Z, or equivalently in the current $I(t)$ through Z. A voltmeter placed across the circuit element will measure an instantaneous voltage that fluctuates with a Gaussian distribution in amplitude, with zero average value, and a width that is determined only by $R(\omega)$ and the temperature T. A useful way to quantify the noise is to use the average spectral density of the noise in angular frequency space, defined for a noise voltage $V(t)$ by

$$S_V(\omega) = \left\langle \int_{-\infty}^{\infty} V^2(t)\cos(\omega t)dt \right\rangle. \tag{19}$$

Here the angle brackets $\langle \ldots \rangle$ indicate that a statistical ensemble average, over many equivalent systems, is to be taken. The spectral density is proportional to the electrical noise power in a unit bandwidth. The Nyquist–Johnson theorem states that this quantity is given by $S_V(\omega) = (2/\pi)R(\omega)\hbar\omega\coth(\hbar\omega/k_BT)$. At high temperatures or low frequencies, such that $k_BT \gg \hbar\omega$, this approaches the classical limit $S_V(\omega)\to 2k_BTR(\omega)/\pi$. The spectral noise density $S_V(f)$, as a function of frequency $f=\omega/2\pi$, is given in the high-temperature limit by $S_V(f)=2\pi S_V(\omega)=4k_BTR(f)$. The metric units of $S_V(f)$ are V^2/Hz. The corresponding current spectral noise density is $S_I(f)=S_V(f)/R^2(f) \to 4k_BT/R(f)$, in the high temperature limit, with units of A^2/Hz.

The fluctuation–dissipation theorem applies to mechanical resonators with nonzero dissipation, i.e., with finite Q, and ensures that the mechanical resonator will also be a source of noise, but due to the resonant nature of the response of the resonator, the noise spectral density takes on a somewhat different form. We will only treat the high-temperature limit, $k_BT \gg \hbar\omega$, for the resonator noise.

A. Dissipation-induced amplitude noise

The displacement of a forced, damped beam driven near its fundamental frequency is given by Eq. (18). In the absence of noise, this solution represents pure harmonic motion at the carrier frequency ω_c. As discussed, the nonzero value of Q^{-1} and temperature T necessitates the presence of noise, from the fluctuation–dissipation theorem. Regardless of the origin of the dissipation mechanism, it acts to thermalize the motion of the resonator, so that in the presence of dissipation only (no driving force), the mean energy $\langle E_n\rangle$ for each mode n of the resonator will be given by $\langle E_n\rangle = k_BT$, where T is the physical temperature of the resonator. This noise term has been considered by a number of authors.[9,14]

The thermalization occurs due to the presence of a noise force $f_N(x,t)$ per unit length of the beam. Each point on the beam experiences a noise force with the same spectral density, but fluctuating independently from other points; the noise at any two points on the beam is uncorrelated. The noise be written as an expansion in terms of the eigenfunctions $Y_n(x)$,

$$f_N(x,t) = \frac{1}{L}\sum_{n=1}^{\infty} f_{N_n}(t)Y_n(x), \tag{20}$$

where the force f_{N_n} associated with the mode n is uncorrelated with that for other modes n'; the factor $1/L$ appears because of the normalization of the Y_n.

The noise force $f_{N_n}(t)$ has a white spectral density $S_{f_n}(\omega)$, and a Gaussian distribution with a zero mean. The magnitude of the spectral density S_{f_n} may be evaluated by requiring that it achieve thermal equilibrium for each mode n. The spectral density of the noise-driven amplitude a_n of the nth mode is given by

$$S_{a_n}(\omega) = \frac{1}{(\Omega_n^2-\omega^2)^2 + (\Omega_n^2/Q)^2}\frac{S_{f_n}(\omega)}{M^2}. \tag{21}$$

The SI units for S_{f_n} are $(\mathrm{N/m})^2/(\mathrm{rad/s}) = \mathrm{kg}^2/(\mathrm{s}^3\,\mathrm{rad})$. Those for S_{a_n} are 1/(rad/s), because a_n is dimensionless.

The kinetic energy KE_n of the nth mode associated with the spectral density S_{a_n} is given by

$$\begin{aligned}\langle KE_n\rangle &= \frac{1}{2}\int_0^{\infty}\int_0^L \rho A\omega^2 S_{a_n}(\omega)Y_n^2(x)dx\,d\omega \\ &= \frac{1}{2}\int_0^{\infty}\rho AL^3\omega^2 S_{a_n}(\omega)d\omega \approx \frac{\pi}{4}\frac{QL^2}{\Omega_n}\frac{S_{f_n}(\omega)}{M},\end{aligned} \tag{22}$$

where the last equality becomes exact in the limit $Q^{-1}\to 0$. The error in Eq. (22) for finite Q is less than 1% for $Q > 10$.

In order that this yield thermal equilibrium, the kinetic energy is $\langle KE_n\rangle = \frac{1}{2}k_BT$, so the spectral density S_{f_n} must be given by

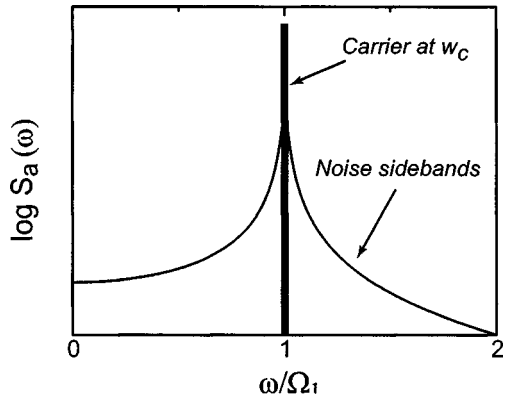

FIG. 2. Frequency spectrum of a driven beam in the presence of noise, showing both the central driven peak as well as the noise sidebands.

$$S_{f_n}(\omega)=\frac{2k_BTM\Omega_n}{\pi QL^2}. \tag{23}$$

The term L^2 appears in Eq. (23) because f_{N_n} is the force per unit length of beam. An equivalent derivation for a one-dimensional simple harmonic oscillator yields the force density $S_F(\omega)=2k_BTM\Omega/\pi Q$. We can write the spectral density of the thermally driven amplitude as

$$S_{a_n}(\omega)=\frac{\Omega_n}{(\Omega_n^2-\omega^2)^2+(\Omega_n^2/Q)^2}\frac{2k_BT}{\pi ML^2Q}. \tag{24}$$

When superposed with a driving force with a carrier frequency $\omega_c=\Omega_1$, the amplitude noise power consists of a δ-function peak at the carrier superposed with the Lorentzian given by Eq. (24), as sketched in Fig. 2.

B. Dissipation-induced phase noise

The form in Eq. (24) represents frequency-distributed amplitude noise. Equivalent expressions can be written for the phase noise, the fractional frequency noise, and the Allan variance,[18] which are useful for time-keeping and filter applications. We note that the different expressions are all equivalent ways of expressing the same noise, and do not represent additional sources of noise. The resonator is driven by the carrier signal near its resonance frequency Ω_1, and in addition by dissipation-induced noise. The time-dependent amplitude is then

$$a(t)=a_0\sin(\omega_ct+\phi(t)+\theta), \tag{25}$$

where $\phi(t)$ represents a phase variation from the carrier at frequency $\omega_c\approx\Omega_1$; the amplitude a_0 is constant, and θ is a phase offset. Following Robins,[19] we pick one frequency component at ω for the phase variation, $\phi(t)=\phi_0\sin(\omega t)$. Assuming small maximum deviation ϕ_0, the amplitude may be written

$$a(t)=a_0\sin(\omega_ct+\theta)+a_0\frac{\phi_0}{2}\sin((\omega_c+\omega)t) - a_0\frac{\phi_0}{2}\sin((\omega_c-\omega)t). \tag{26}$$

The phase variation at ω generates sidebands spaced $\pm\omega$ from the carrier, with amplitude $\pm a_0\phi_0/2$. The lower sideband is phase coherent with the upper sideband, with the opposite sign; this is characteristic of phase noise. Independent sideband signals can be generated by adding an amplitude noise source $M(t)$ to the phase noise $\phi(t)$, so that the amplitude is written as

$$a(t)=a_0(1+M(t))\sin(\omega_ct+\phi(t)+\theta). \tag{27}$$

We consider a single component at ω for both the phase and amplitude modulation, so that

$$M(t)=M_0\sin(\omega t) \qquad \phi(t)=\phi_0\sin(\omega t). \tag{28}$$

Again assuming small variations, this can be written as

$$a(t)=a_0\sin(\omega_ct+\theta)+\tfrac{1}{2}a_0(M_0+\phi_0)\sin((\omega_c+\omega)t) + \tfrac{1}{2}a_0(M_0-\phi_0)\sin((\omega_c-\omega)t). \tag{29}$$

Setting the amplitude $M_0=\phi_0$, the lower sideband disappears and we are left with the independent upper sideband term,

$$a(t)=a_0\sin(\omega_ct+\theta)+a_0\phi_0\sin((\omega_c+\omega)t). \tag{30}$$

Choosing the opposite sign relation $M_0=-\phi_0$ allows the lower sideband to be chosen.

A noise signal at a frequency offset from the carrier can be created from the superposition of a phase and an amplitude modulation of the original carrier. In applications where the resonator is to be used as a frequency source or a clock, the amplitude modulation is unimportant: Use of a zero-crossing detector, or a perfect limiter, eliminates the effects of the amplitude modulation. We therefore ignore this noise source. This is equivalent, from the arguments leading to Eq. (26), to limiting the noise to that which is phase coherent between the upper and lower sidebands, with amplitudes $a(\omega_c+\omega)=-a(\omega_c-\omega)$. Noise which has the opposite phase relation, with $a(\omega_c+\omega)=+a(\omega_c-\omega)$, is due to amplitude modulation. Noise associated with only one sideband consists of the sum or difference of these two ''modes''.

Dissipation-induced noise, of the form given by Eq. (24), is intrinsically phase incoherent on opposite sides of the carrier signal at ω_c. Half of the noise power is therefore associated with amplitude modulation, and half with phase modulation; the phase noise power is therefore *half* the original total noise power.

We can evaluate the dissipation-induced phase noise for a resonator driven at its fundamental resonance frequency. We drive the resonator with a force f per unit length, at the frequency $\omega_c=\Omega_1$. The amplitude for the response is given by Eq. (18),

$$a_1=-i\frac{\eta_1}{\Omega_1^2}\frac{Qf}{M}. \tag{31}$$

The amplitude lags the force by 90°, and includes the multiplicative factor Q. Dissipation generates incoherent noise,

distributed about the carrier with noise power given by Eq. (24). The phase noise power density $S_\phi(\omega)$ at frequency ω from the carrier frequency is then given by

$$S_\phi(\omega)=\frac{1}{2}\frac{S_{a_1}(\Omega_1+\omega)}{|a_1|^2}$$

$$=\frac{\Omega_1}{(2\Omega_1\omega+\omega^2)^2+(\Omega_1^2/Q)^2}\frac{k_BT}{\pi|a_1|^2L^2MQ}. \quad (32)$$

For frequencies that are well off the peak resonance, $\omega \gg \Omega_1/Q$, but small compared to the resonance frequency, $\omega \ll \Omega_1$, we may approximate the denominator as

$$S_\phi(\omega)\approx\frac{k_BT}{4\pi\Omega_1\omega^2|a_1|^2L^2MQ}$$

$$\approx\frac{k_BT\Omega_1}{8\pi E_cQ\omega^2} \quad (\Omega_1/Q\ll\omega\ll\Omega_1). \quad (33)$$

Here, we define the energy E_c at the carrier frequency, $E_c=M\Omega_1^2L^2|a_1|^2/2$. This can also be written in terms of the power $P_c=\Omega_1E_c/Q$ needed to maintain the carrier amplitude, i.e., that needed to counter the loss due to the nonzero value of $1/Q$:

$$S_\phi(\omega)\approx\frac{k_BT}{8\pi P_cQ^2}\left(\frac{\Omega_1}{\omega}\right)^2 \quad (\Omega_1/Q\ll\omega\ll\Omega_1). \quad (34)$$

We can also write this expression in terms of frequency $f=2\pi\omega$,

$$S_\phi(f)\approx\frac{k_BT}{4P_cQ^2}\left(\frac{\nu_1}{f}\right)^2 \quad (\nu_1/Q\ll f\ll\nu_1). \quad (35)$$

C. Frequency noise

The phase fluctuations can also be viewed as *frequency* fluctuations, where the amplitude $a(t)$ has a time dependence

$$a(t)=a_0\sin\left(\int_{-\infty}^{t}\omega(t')dt'+\theta\right). \quad (36)$$

The time-dependent frequency $\omega(t)$ is related to the carrier frequency ω_c and the phase $\phi(t)$ by

$$\omega(t)=\frac{d(\omega_ct+\phi(t))}{dt}=\omega_c+\frac{d\phi}{dt}. \quad (37)$$

We define time-dependent frequency variation $\delta\omega(t)$ as

$$\delta\omega(t)=\omega(t)-\omega_c=\frac{d\phi(t)}{dt}. \quad (38)$$

We consider a single-phase modulation component, so that $\phi(t)=\phi_0\sin(\omega t)$. The frequency variation

$$\delta\omega(t)=\delta\omega_0\cos(\omega t)=\omega\phi_0\cos(\omega t) \quad (39)$$

represents a sinusoidal variation of the frequency, with amplitude $\delta\omega_0=\omega\phi_0$, modulated at ω. The time-dependent amplitude in Eq. (36) is

$$a(t)=a_0\sin(\omega_ct+(\delta\omega_0/\omega)\sin(\omega t)+\theta)$$

$$=a_0\sin(\omega_ct)+\frac{1}{2}a_0\frac{\delta\omega_0}{\omega}\sin((\omega_c+\omega)t)$$

$$-\frac{1}{2}a_0\frac{\delta\omega_0}{\omega}\sin((\omega_c-\omega)t), \quad (40)$$

a result very similar to that for phase variations, Eq. (26).

The arguments leading to the spectral density, Eq. (34), may be reworked to yield the equivalent expression for the frequency variation noise density $S_{\delta\omega}$. A more useful quantity is the *fractional* frequency variation, defined as $y=\delta\omega/\omega_c$. The noise density for y is related to that for the phase noise density by

$$S_y(\omega)=\left(\frac{\partial y}{\partial\phi}\right)^2S_\phi(\omega)=\left(\frac{\omega}{\omega_c}\right)^2S_\phi(\omega), \quad (41)$$

where we use the fact that modulation at ω generates sidebands at $\pm\omega$ from the carrier at ω_c. From Eq. (34), we then have

$$S_y(\omega)\approx\frac{k_BT}{8\pi P_cQ^2} \quad (\omega_c/Q\ll\omega\ll\omega_c). \quad (42)$$

In the frequency domain, this is

$$S_y(f)\approx\frac{\pi k_BT}{4P_cQ^2} \quad (\nu_c/Q\ll f\ll\nu_c). \quad (43)$$

D. Allan variance

A third useful quantity, commonly used to compare frequency standards, is the Allan variance $\sigma_A(\tau_A)$.[20,21] The phase and frequency noise are defined in the frequency domain; the Allan variance is defined in the time domain, as the variance over time in the measured frequency of a source, each measurement averaged over a time interval τ_A, with zero-dead time between measurement intervals. The defining expression for the square of the Allan variance is

$$\sigma_A^2(\tau_A)=\frac{1}{2f_c^2}\frac{1}{N-1}\sum_{m=2}^{N}(\overline{f}_m-\overline{f}_{m-1})^2, \quad (44)$$

where $\overline{f}_m$ is the average frequency measured over the mth time interval, of length $\Delta t=\tau_A$, and f_c is the nominal carrier frequency. The squared Allan variance is related to the phase noise density by[21]

$$\sigma_A^2(\tau_A)=2\left(\frac{2}{\omega_c\tau_A}\right)^2\int_0^\infty S_\phi(\omega)\sin^4(\omega\tau_A/2)d\omega, \quad (45)$$

where $\omega_c=2\pi f_c$ and ω is the modulation frequency.

The Allan variance can be calculated for various functional forms for the phase noise density. For a fractional frequency noise that has a $1/f$ component, so that $S_y(\omega)=A(\omega_c/\omega)$, where A is a scale factor, the phase noise density is $S_\phi(\omega)=A(\omega_c/\omega)^3$, and the Allan variance is

$$\sigma_A(\tau_A)=\sqrt{2\log_e 2A\omega_c}. \quad (46)$$

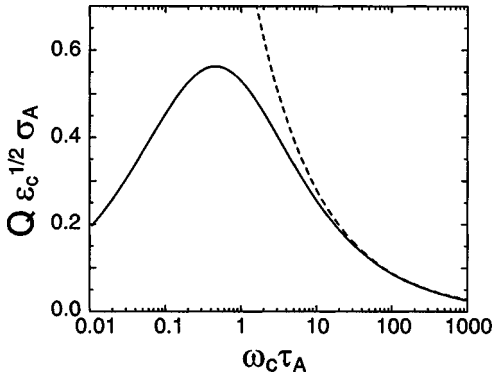

FIG. 3. Dependence of the Allan variance σ_A on the dimensionless time interval $\omega_c\tau$; the Allan variance has been scaled to remove the overall dependence on Q and on drive energy ε_c. The full dependence [from Eq. (32)] is plotted as a solid line, while the approximate form [Eq. (50)] is plotted as a dotted line.

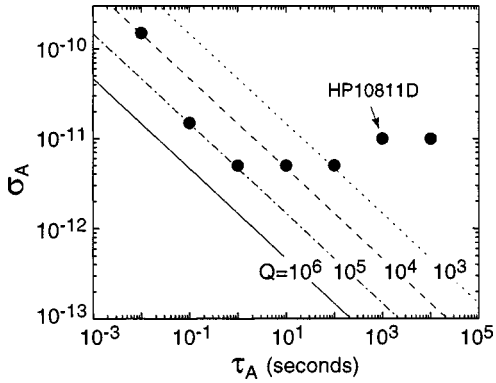

FIG. 4. Allan variance σ_A as a function of measurement interval τ_A, calculated for the model 1 GHz resonator for a range of values of Q from 10^3 to 10^6. The drive power level P_c was chosen so that the amplitude of motion $a_1 = t$, the beam thickness, For comparison, we also display the variance for a 10 MHz quartz crystal frequency standard, the HP10811D; figures taken from manufacturer's specifications.

Hence a $1/f$ fractional frequency noise yields an Allan variance that is independent of the measurement time interval.

For a source that displays frequency drift, the fractional frequency noise will have the form $S_y(\omega) = B(\omega_c/\omega)^2$; the phase noise density is then $S_\phi(\omega) = B(\omega_c/\omega)^4$, and the Allan variance is

$$\sigma_A(\tau_A) = \sqrt{\frac{\pi}{3} B\omega_c^2 \tau_A}. \tag{47}$$

Finally, for a white fractional frequency noise density $S_y(\omega) = C$, the phase noise density has the form $S_\phi(\omega) = C(\omega_c/\omega)^2$, and the Allan variance is

$$\sigma_A(\tau_A) = \sqrt{\frac{\pi C}{\tau_A}}. \tag{48}$$

In particular, for the approximate form for the phase noise density Eq. (34), the Allan variance is

$$\sigma_A(\tau_A) = \sqrt{\frac{k_B T}{8 P_c Q^2 \tau_A}}. \tag{49}$$

Defining the dimensionless drive energy ε_c as the ratio of drive energy per cycle to the thermal energy, $\varepsilon_c = 2\pi P_c/\omega_c k_B T$, we have

$$\sigma_A(\tau_A) = \frac{1}{Q}\sqrt{\frac{\pi}{4\varepsilon_c \omega_c \tau_A}}. \tag{50}$$

We see that the Allan variance falls inversely with the square root of the product $\omega_c\tau_A$, and it is also proportional to the dissipation Q^{-1}. Other things being equal, increasing the resonator frequency ω_c lowers the Allan variance.

In Fig. 3, we display the approximate result Eq. (50) as a function of $\omega_c\tau_A$, scaled to remove the dependence on Q and on ε_c; we also show the full result obtained from integrating Eq. (32), for values of $Q > 100$; for values of Q less than this, the calculated value for the scaled variance falls below that plotted.

We see that the approximate expression given by Eq. (50) works quite well for averaging times τ_A more than a few tens of the oscillation period $2\pi/\omega_c$; in time-keeping or frequency-lock applications, one is typically interested in times much longer than this, so the approximate form is quite adequate.

We now turn to examining what the implications are for the fundamental sources of noise in our model resonator. We will focus on calculating the predicted dependence of the Allan variance.

E. Model resonator Q-dependent noise

We calculate the dependence of the Allan variance σ_A on the time interval and Q for our model 1 GHz resonator, described in Table II. The results of the calculation are shown in Fig. 4. The drive power level P_c is chosen so that the amplitude of motion a_1 in Eq. (18) is equal to the beam thickness t, approximately the amplitude for the onset of nonlinearity. The calculated temperature rise due to dissipation in the resonator from this level of drive power is very small, of order 0.1 K. We also display for comparison the Allan variance for an oven-controlled 10 MHz quartz crystal oscillator, the HP10811D.[22] For quality factors higher than 10^5, the calculated thermally induced fluctuations are comparable to or better than those of the bulk quartz resonator.

IV. TEMPERATURE FLUCTUATIONS

We now turn to a discussion of the effects of finite thermal conductance and heat capacitance on the Allan variance. The small dimensions associated with our model resonator, and of nanoscale resonators in general, imply that the heat capacity of the resonator is very small. The corresponding thermal fluctuations are proportionally larger, and these may in turn produce significant frequency fluctuations, due to the temperature dependence of the resonator material parameters and geometric dimensions. Here, we present a simple model through which the magnitude of these effects can be estimated.

A heat capacitance c, connected by a thermal conductance g to an infinite thermal reservoir at temperature T, will have an average thermal energy $\langle E_c \rangle = cT$ in the absence of any power loads. Changes in the temperature relax with the

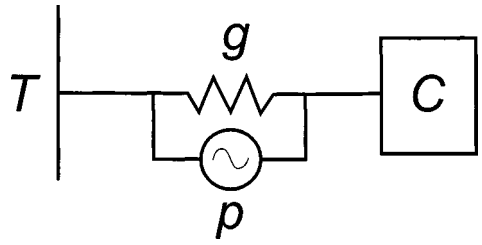

FIG. 5. Thermal circuit with a finite thermal conductance g and a finite heat capacitance c, including a power noise source p.

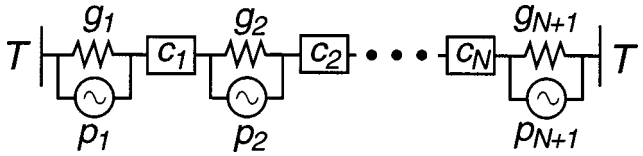

FIG. 6. Thermal model for doubly clamped beam, consisting of a series connection of heat capacitances c_n and thermal conductances g_n, each associated with a cross-sectional slice of the beam of length Δx. Each thermal conductance is associated with a power noise source p_n. The ends are assumed clamped at the reservoir temperature T. There are a total of $N = L/\Delta x$ elements.

thermal time constant $\tau_T = c/g$. The energy E_c will however fluctuate, as the fluctuation–dissipation theorem applies to finite thermal conductances in a manner similar to the dissipation-induced mechanical noise.[23] The thermal circuit therefore includes a power noise source p with spectral density $S_p(\omega) = 2k_B T^2 g/\pi$ (see Fig. 5). The instantaneous energy of the heat capacitance can then be written $E_c(t) = cT + \delta E(t)$, where the spectral density of the energy fluctuations $\delta E(t)$ can be derived from the thermal circuit,

$$S_E(\omega) = \frac{2}{\pi} \frac{k_B T^2 c^2/g}{1+\omega^2 \tau_T^2}. \tag{51}$$

We can interpret the energy fluctuations as temperature fluctuations $\delta T_c(t)$, if we define the temperature as $T_c = E_c/c$. The corresponding spectral density of the temperature fluctuations is given by

$$S_T(\omega) = \frac{2}{\pi} \frac{k_B T^2/g}{1+\omega^2 \tau_T^2}. \tag{52}$$

At low frequencies ω, below that of the thermal frequency $1/\tau_T$, the temperature fluctuations δT follow those driven by the noise source p, while at higher frequencies the nonzero heat capacitance acts as a filter.

For a resonator with the geometry shown in Fig. 1, there is no clear separation of the structure into a distinct heat capacitance and thermal conductance. Instead, we divide the resonator into slices of length Δx and cross-sectional area $A = w \times t$, so that the nth slice has heat capacity $c_n = C_v A \Delta x$, where C_v is the specific heat per unit volume. The $(n-1)$th and nth slices are connected to one another by the thermal conductance $g_n = \kappa A/\Delta x$, with thermal conductivity κ given by the classical formula, $\kappa = (1/3) C_V c_s \ell$ (ℓ is the phonon mean-free path and c_s the sound speed). The thermal conductances g_n are associated with noise power sources p_n, with spectral density $S_{p_n}(\omega) = 2k_B T^2 g_n/\pi$. Finally, the temperatures at the ends of the beam, where the beam is mechanically clamped, are assumed to be given by the reservoir temperature T; see Fig. 6.

In this model, energy fluctuations in the slices $n-1$ and n are anticorrelated through the shared conductance g_n: An energy δE driven into the nth slice by p_n corresponds to the same energy taken from the $(n-1)$th slice. These energy fluctuations then relax through conductance into adjacent slices, and so on through the beam length, so that there is some correlation between the fluctuations in all slices, although the correlations get weak for distant slices.

One might expect that the most accurate model would use slices with differential lengths $\Delta x = dx \to 0$. However, once the slices become shorter than the phonon mean-free path ℓ, the temperature in a slice is no longer well defined. We therefore choose slices with a length $\Delta x = \ell = 50$ nm, so that each element has a volume $V = 50 \times 50 \times 50$ nm^3. The corresponding heat capacity is $c = C_V V = 2 \times 10^{-16}$ J/K, and the thermal links have $g = \kappa \ell = 7.4 \times 10^{-6}$ W/K. The thermal time constant is $\tau_T = 30$ ps, corresponding to thermal frequencies ~ 35 GHz, well outside the range of frequencies of interest for resonator phase fluctuations, $\Omega_1/Q \ll \omega \ll \Omega_1$. For the purposes of this calculation, therefore, we can treat the thermal fluctuations in the low-frequency limit.

Consider only the nth power source of the conductance p_n. If we take the frequency component at ω, the $(n-1)$th and nth slices have temperature variations $T_{n-1}(\omega)$ and $T_n(\omega)$ given by

$$\begin{aligned} (2 + i\omega\tau) T_{n-1} &= -\frac{p_n}{g} + T_{n-2} + T_n \\ (2 + i\omega\tau) T_n &= \frac{p_n}{g} + T_{n-1} + T_{n+1}. \end{aligned} \tag{53}$$

The corresponding equation for the $(n+m)$th slice is given by

$$(2 + i\omega\tau_T) T_{n+m} = T_{n+m-1} + T_{n+m+1}. \tag{54}$$

Taking the limit $\omega\tau_T \ll 1$, we find that the power source $p_n(\omega)$ driving the nth slice generates a temperature variation $T(\omega) = p_n(\omega)/2g$ uniformly across the beam. The corresponding anticorrelated source $-p_n(\omega)$ driving the $(n-1)$th slice generates an equal but opposite temperature variation. Hence, in the limit $\omega\tau_T \ll 1$, the fluctuations driven by conductances within the beam have no net effect.

The other source of temperature fluctuations comes from the conductances at the beam ends, g_1 and g_{N+1}. These also drive the beam uniformly, but as the energy that appears in the first and last elements does not have an adjacent anticorrelated source, there is now a net effect. The final result from this model is that the temperature of all the elements in the beam fluctuate uniformly, with spectral density $S_T(\omega)$ given by the incoherent sum of the two end sources,

$$S_T(\omega) = \frac{4}{\pi} \frac{k_B T^2/g}{1+\omega^2 \tau_T^2} \quad (\omega\tau_T \ll 1). \tag{55}$$

We have kept the frequency dependence of the thermal circuit in order to retain the high-frequency cutoff in the fluctuations.

The effect these temperature fluctuations have on the resonator behavior involves changes in the density and elastic modulus, which affect the frequency directly, and through changes in the overall resonator length. The density and elastic modulus determine the resonator frequency through the combination $\sqrt{E/\rho}$, which is the sound speed c_s; this quantity has the fractional temperature dependence $(1/c_s)\partial c_s/\partial T = -5\times10^{-5}/\mathrm{K}$ for pure Si.[24] The corresponding temperature dependence of the resonator frequency is given by

$$\frac{1}{\Omega_n}\frac{\partial\Omega_n}{\partial T}=\frac{1}{c_s}\frac{\partial c_s}{\partial T} \quad \text{(sound speed dependence)}. \tag{56}$$

The changes in resonator length generate longitudinal stress in the resonator, as the ends are assumed rigidly clamped. The resonator length L changes with temperature due to the thermal expansion of Si, with $(1/L)\partial L/\partial T=\alpha_T = 2.8\times10^{-6}/\mathrm{K}$. A temperature change ΔT therefore induces a longitudinal extensional stress $\tau=-E\alpha_T\Delta T$. This in turn causes a change in the nth resonator frequency $\Omega_n(\tau)$, which for small extensional stress τ is given by[15]

$$\Omega_n^2(\tau)=\Omega_n^2(0)+k_n^2\frac{\tau}{\rho}, \tag{57}$$

in terms of the beam eigenvectors k_n and eigenfrequencies $\Omega_n=\sqrt{EI/\rho A}k_n^2$. The fractional frequency dependence due to length change is therefore

$$\frac{1}{\Omega_n}\frac{\partial\Omega_n}{\partial T}=-\frac{1}{2}\frac{E}{\rho}\frac{k_n^2}{\Omega_n^2}\alpha_T \quad \text{(length dependence)}. \tag{58}$$

Hence, the spectral density of fractional frequency fluctuations $S_y(\omega)$ caused by the combined temperature dependence on sound speed and beam length is given by

$$\begin{aligned} S_y(\omega)&=\left(\frac{1}{\Omega}\frac{\partial\Omega}{\partial T}\right)^2 S_T(\omega)\\ &=\left(-\frac{c_s^2k_n^2}{\Omega_n^2}\alpha_T+\frac{2}{c_s}\frac{\partial c_s}{\partial T}\right)^2\frac{k_BT^2/\pi g}{1+\omega^2\tau_T^2}. \end{aligned} \tag{59}$$

For the fundamental mode, we have $k_1=4.73/L$, and inserting the model resonator parameters, we find

$$S_y(\omega)=(1.6\times10^{-8}/\mathrm{K}^2)\frac{k_BT^2/g}{1+\omega^2\tau_T^2}=\frac{2.7\times10^{-21}}{1+\omega^2\tau_T^2}\frac{1}{\text{rad/s}}. \tag{60}$$

From the fractional frequency noise, Eq. (60), we calculate the Allan variance:

$$\begin{aligned} \sigma_A(\tau_A)&=(2.25\times10^{-4}/\mathrm{K}^2)\sqrt{k_BT^2/g\tau_A}\\ &=9.3\times10^{-11}\frac{1}{\sqrt{\tau_A}}, \end{aligned} \tag{61}$$

in the limit $\tau_A\gg\tau_T$. The contribution of thermal fluctuations to the Allan variance for our model resonator is therefore of the same magnitude and dependence on averaging time τ_A as that due to mechanical dissipation for a resonator with Q of about 10^4, and is a significant source of fluctuation. Ways to reduce the size of this source of variance include the use of materials with larger thermal conductance, such as AlN (3.20 W/cm K)[25] and sapphire (4.50 W/cm K), or better temperature-compensated materials, such as quartz.

V. OTHER SOURCES OF NOISE

There are a number of other sources of noise that can affect resonator performance. We discuss here two such sources, one due to adsorption–desorption noise of residual gas molecules, and the other due to defect motion within the resonator structure.

A. Adsorption–desorption noise

Adsorption–desorption noise has been discussed in some detail by Vig and Kim[12] and Yong and Vig.[11] The resonator environment will always include a nonzero pressure of surface-contaminating molecules. These molecules, when they adsorb on a site on the resonator surface, mass load the resonator, and thereby change its resonance frequency. As the molecules adsorb and desorb due to their finite binding energy and nonzero temperature, the resulting changes in frequency translate to a source of phase or fractional frequency noise. As discussed herein, this type of noise does not fit into the Zener formalism, as the adsorption–desorption cycle is not intrinsically a dissipative one: As the arrival and departure times of the atoms are random, they do not on average change the energy of the resonator, but cause its frequency to change in a discontinuous fashion, leaving the quality factor unchanged. This type of parametric noise (where the overall resonator mass is fluctuating) is therefore not described by the lossy stress–strain relation developed by Zener.

The frequency change due to a single adsorbed molecule, $\Delta\Omega$, is proportional to the ratio of the molecule to resonator total mass, m/M; smaller mass resonators are more sensitive than larger ones. Furthermore, as the resonator size scale is reduced, the number of adsorption sites N_a on the resonator surface grows in proportion to the number of total number of resonator atoms: The surface-to-volume ratio grows inversely to the size scale. Hence, nanoscale resonators are more susceptible to adsorption–desorption noise than larger, bulk mechanical resonators.

We use a simple model to estimate the noise from this source. We assume a single molecular species with mass m, surface binding energy E_b, and pressure P. Expressions may be derived for the adsorption and desorption rates r_a and r_d at any given surface site;[11] with sticking coefficient s, the adsorption rate at any site is given by

$$r_a=\frac{2}{5}\frac{P}{\sqrt{mk_BT}}s. \tag{62}$$

The sticking coefficient is typically temperature dependent.[26] Once bound to the surface, a molecule desorbs at a rate

$$r_d = \nu_d \exp\left(-\frac{E_b}{k_B T}\right), \tag{63}$$

where ν_d is the desorption attempt frequency, typically of order 10^{13} Hz, and E_b is the desorption energy barrier. The average occupation f of a site is then $f = r_a/(r_a + r_d)$; the variance in the occupation probability is $\sigma_{\text{occ}}^2 = r_a r_d/(r_a + r_d)^2$.

An expression may then be derived for the phase noise $S_\phi(\omega)$ resulting from the statistics of the adsorption–desorption process:[11]

$$S_\phi(\omega) = \frac{2N_a\sigma_{\text{occ}}^2\tau_A/\pi}{1+\omega^2\tau_r^2}\frac{\Delta\Omega^2}{\omega^2}. \tag{64}$$

Here, τ_r is the correlation time for an adsorption–desorption cycle, $1/\tau_r = r_a + r_d$. A simple mass-loading formula may be assumed, $\Delta\Omega = (m/2M)\Omega_1$, where M is the resonator mass and Ω_1 is the fundamental frequency of the resonator. A corresponding expression for the fractional frequency noise is then given by

$$S_y(\omega) = \frac{N_a\sigma_{\text{occ}}^2\tau_r/2\pi}{1+\omega^2\tau_r^2}\left(\frac{m}{M}\right)^2. \tag{65}$$

We calculate the Allan variance,

$$\sigma_A(\tau_A) = \sqrt{\frac{N_a\tau_r}{2\tau_A}}\frac{\sigma_{\text{occ}}m}{M}, \tag{66}$$

in the limit $\tau_A \gg \tau_r$.

The occupation variance σ_{occ}^2, and therefore the noise, is maximum when the site occupation probability is $f = 0.5$, i.e., when the adsorption and desorption rates are equal. The noise is minimized when the occupation probability is either near zero or near unity. For typical packaged pressures, molecular sticking coefficients, and binding energies, occupation probabilities are quite small; we therefore try to minimize the occupation to reduce the fluctuation variance. The exponential dependence of the desorption rate r_d on temperature provides a useful approach; heating the resonator, using an on-chip heating element, causes significant increases in the desorption rate and therefore in the occupation variance σ_{occ}^2.

In Fig. 7, we plot the Allan variance for a 1 s averaging interval, as a function of package pressure, for two resonator temperatures, 300 and 500 K. We have chosen a contaminant molecule with an binding energy of $E_b = 10$ kcal/mol, with one adsorption site every 0.25 nm^2, and a sticking coefficient of 0.1, typical values for gas molecules adsorbing on metal surfaces.[11,26] Note that the sticking coefficient is typically temperature dependent,[26] but here we have taken it as constant. We show for comparison the overall Allan variance for the HP 10811D 10 MHz quartz oscillator, again for a 1 s averaging interval.

It is clear from Fig. 7 that this source of noise is extremely important. Great care must be taken to passivate the resonator surface, thus reducing the sticking coefficient, reduce the pressure, for instance by including getters in the package, and possibly raising the ambient temperature.

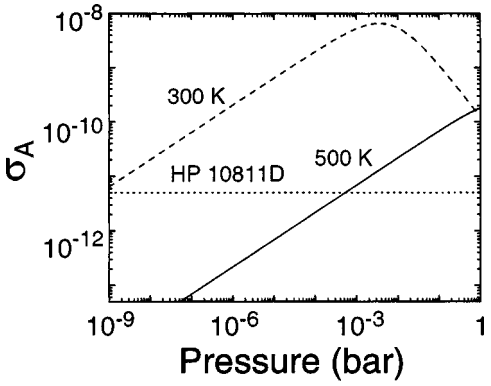

FIG. 7. Allan variance for a 1 s averaging interval as a function of package pressure for two resonator temperatures, 300 and 500 K. The contaminant molecule has a binding energy $E_b = 10$ kcal/mol, with one adsorption site every 0.25 nm^2, and a sticking coefficient of 0.1. Also shown is the fractional noise for the HP10811D 10 MHz quartz resonator, for a 1 s averaging interval.

B. Defect motion

The last source of noise we would like to consider is that caused by defect motion within the resonator volume. For the single-crystal resonators we have been considering, defect levels are very low in the base material. Statistically, there are of order 0 to 1 defects within the volume of the resonator. We therefore do not expect this to provide a serious source of noise in these resonators.

However, there has been extensive work on developing polycrystalline materials for resonators, especially using silicon nitride and poly-Si.[5,6] These materials include a large density of grain boundaries, point defects, and some voids, and the motion of these defects can cause phase and frequency noise in high-Q resonators. Amorphous Si created by implantation has defect densities of order 1%;[27] similar levels are expected for chemical vapor deposition-grown polysilicon. The quality factors of resonators fabricated from this material are comparable, at room temperature, to those made from single-crystal materials such Si and GaAs, but defect processes may still play a very important role.

Point defects in a solid can be treated as elastic dipoles, with symmetry different from that of the underlying crystal (see e.g., Nowick and Berry[13]). In the relaxed state, the defects are randomly oriented; reorientations occur due to thermally induced motion, at a rate $\Gamma_d = \nu_0 \exp(-\Delta g^*/k_B T)$, with an attempt frequency $\nu_0 \sim 10^{12}$ Hz and free energy barrier Δg^*, typically of order 0.1–1 eV. If we consider a defect with two possible orientations, with equal energies, the occupation probabilities are given by the Gibbs distribution and are each equal to 1/2; the variance in the mean occupation is equal to 1/4, with mean reorientation time $\tau_d = 1/\Gamma_d$. Defects in which the possible orientations have different energies will have smaller variances in the occupation, and there will be a range of reorientation times as well.

A single defect moving or reorienting itself can cause a change in the local Young's modulus E; if the defect has two possible configurations, $-$ and $+$, the corresponding local modulus changes from $E_s + E_-$ to $E_s + E_+$, where E_s is the

TABLE IV. Expressions for the various spectral noise densities worked out for different representations of the same noise, as well as for noise associated with different fundamental processes.

Type of noise	Symbol	Expression	Equation
Force noise, mode n	$S_{f_n}(\omega)$	$\frac{2k_BTM\Omega_n}{\pi QL^2}$	(23)
Amplitude noise, mode n	$S_{a_n}(\omega)$	$\frac{\Omega_n}{(\Omega_n^2-\omega^2)^2+(\Omega_n^2/Q)^2}\frac{2k_BT}{\pi ML^2Q}$	(24)
On-resonance amplitude noise, mode n	$S_{a_n}(\Omega_n)$	$\frac{2k_BTQ}{\pi ML^2\Omega_n}$	(24)
Off-resonance phase noise, mode $n=1$	$S_\phi(\omega)$	$\frac{k_BT}{8\pi P_cQ^2}\left(\frac{\Omega_1}{\omega}\right)^2$	(34)
Off-resonance fractional frequency noise, $n=1$	$S_y(\omega)$	$\frac{k_BT}{8\pi P_cQ^2}$	(42)
Allan variance, $n=1$	$\sigma_A(\tau_A)$	$\sqrt{\frac{k_BT}{8P_cQ^2\tau_A}}$	(49)
Temperature fluctuations	$S_T(\omega)$	$\frac{4}{\pi}\frac{k_BT^2/g}{1+\omega^2\tau_T^2}$	(55)
Allan variance, temperature fluctuations	$\sigma_A(\tau_A)$	$(2.25\times10^{-4}/\mathrm{K}^2)\sqrt{k_BT^2/g\tau_A}$	(61)
Allan variance, adsorption desorption	$\sigma_A(\tau_A)$	$\sqrt{\frac{2N_a\tau_r}{\tau_A}}\frac{\sigma_{\mathrm{occ}}m}{M}$	(66)
Allan variance, defect motion	$\sigma_A(\tau_A)$	$\sqrt{\frac{2\sigma_\omega^2}{\langle\Omega\rangle^2}}\sqrt{\frac{\tau_d}{\tau_A}}$	(68)

defect-free modulus. Typical values for $E_\pm$ are in the range $0.01-0.1E_s$. A mole fraction $C_d \ll 1$ of such defects, all simultaneously reorienting from $-$ to $+$, will cause the effective modulus to change[13] from $E_s+C_dE_-$ to $E_s+C_dE_+$. If we consider a total mole fraction of identical defects $C_0 \ll 1$, that reorient independently between configurations $-$ and $+$ with equal free energies, so that the two configurations are equally likely, the average elastic modulus for the solid will be $\langle E\rangle \approx E_s+C_0(E_-+E_+)/2$. The variance in the elastic modulus is given by the Poisson formula, $\sigma_E^2 \approx C_0(E_+-E_-)^2/4$. Additional noise sources can appear from the defect motion itself; the defect may resonate at a frequency near the resonator natural frequency, causing additional dissipation and additional noise terms. We ignore such effects here.

Applying this discussion to resonator frequency fluctuations, if we assume the defects all have equal impact on the resonator frequency Ω, the mean resonator frequency $\langle\Omega\rangle$ will be that calculated from Eq. (3) using the average modulus $\langle E\rangle$. The frequency will have a mean variance given by $\sigma_\Omega^2=(C_0/8)(\Omega_+-\Omega_-)^2$, where $\Omega_\pm$ are calculated from Eq. (3) using the moduli $E_s+C_0E_\pm$.

These fluctuations, occurring with a single reorientation time τ_d, will generate fractional frequency noise with the spectral density

$$S_y(\omega)=\frac{2}{\pi}\frac{\sigma_\Omega^2}{\langle\Omega\rangle^2}\frac{\tau_d}{1+\omega^2\tau_d^2}. \tag{67}$$

For this distribution, the corresponding Allan variance has a similar functional form to that shown in Fig. 3. The defect reconfiguration time τ_d can range from μs to minutes or hours at room temperature, with an exponential temperature dependence. For averaging times τ_A much larger than τ_d, the approximate form for the Allan variance is

$$\sigma_A(\tau_A)=\sqrt{\frac{2\sigma_\omega^2}{\langle\Omega\rangle^2}}\sqrt{\frac{\tau_d}{\tau_A}}. \tag{68}$$

If we assume a defect mole fraction $C_0=0.001$, and modulus changes $E_\pm=\pm0.1E_s$, the frequency variance is $\sigma_\Omega \approx 1\times10^{-6}\Omega$. For a defect reconfiguration time $\tau_d=1$ ms, we find an Allan variance at $\tau_A=1$ s of 5×10^{-8}, a quite large contribution compared to those we have been considering. Clearly, active defect concentrations C_0 of less than 1 part in 10^5 are needed to achieve Allan variances competitive with those of single-crystal resonators.

We note that a typical solid will include a range of reorientation times τ_d, which when superposed generically produce $1/f$ noise through the Dutta–Dimon–Horn model.[28] In that case, we can write

$$S_y(\omega)\approx A\frac{\omega_c}{\omega}k_BT\mathcal{D}(\bar{E}), \tag{69}$$

where $\mathcal{D}(\bar{E})$ is the density of defect states at energy $\bar{E}=-k_BT\log_e(\omega/\nu_0)$ and A is a scale factor. In this case the Allan variance works out to be [see Eq. (46)]

$$\sigma_A(\tau_A) \approx \sqrt{2\log_e 2A\omega_c}\sqrt{k_B T \mathcal{D}(\overline{E})}. \quad (70)$$

Here, we see the Allan variance independent of averaging time τ_A, but with a magnitude comparable to that of Eq. (68).

Such processes, which play an important role in single-crystal and polycrystalline metals, and for which much information in metals exists, need to be investigated in silicon nitride and poly-Si to determine whether these play an important role in limiting resonator performance.

VI. CONCLUSIONS

We have described a formalism for treating the resonance behavior, loss processes, and resulting frequency and phase noise in nanoscale resonators. We then applied this formalism to evaluate the role of a number of fundamental and material-dependent noise sources, and how these sources affect the frequency stability of a model 1 GHz nanomechanical resonator. For practical applications, the relevant comparison has been made with an industry standard, the oven-controlled high-precision quartz crystal. We find that the anticipated resonator noise is predominantly from thermomechanical noise, temperature fluctuations, and adsorption–desorption noise. The noise levels from these sources are comparable in magnitude to that of the quartz crystal, provided some care is taken to minimize certain important loss processes. In Table IV, we have tabulated the various expressions for the noise, from different treatments and from different noise sources.

The results we have calculated here are for a doubly clamped, flexural resonator. Any resonator whose basic equations of motion can be reduced to those of a linear simple harmonic oscillator, driven by a force term, will have results of the form shown here. The results for a cantilevered beam, a torsional resonator, and a longitudinal wave resonator will therefore all be identical to these, except that the resonance frequencies and the mode shapes are different, so that the numerical prefactors will be somewhat different.

For practical applications, nanoscale resonators can be fabricated on chip with electronics needed to provide precision frequency control. This would obviate the need for an externally packaged and controlled quartz crystal, and enable integrated fabrication.

Clearly, there are gaps in the available data for evaluating whether the noise performance calculated here can be achieved in fact. More systematic approaches, measuring the performance of high-Q resonators operated in phase-locked loops, with controlled variations in temperature, environment, and materials, need to be followed in order to determine whether the suggested applications are indeed viable. A better understanding of the role of defects and molecular adsorption and desorption is also needed to evaluate the effect these have on frequency stability.

ACKNOWLEDGMENTS

The authors acknowledge the financial support provided by the National Science Foundation XYZ-On-A-Chip Program, Contract No. ECS-9980734, by the Army Research Office, and by the Research Corporation through a Research Innovation Award.

[1] A. N. Cleland and M. L. Roukes, Appl. Phys. Lett. **69**, 2653 (1996).
[2] A. N. Cleland and M. L. Roukes, Nature (London) **320**, 160 (1998).
[3] Y. T. Yang, K. L. Ekinci, X. M. H. Huang, L. M. Schiavone, M. L. Roukes, C. A. Zorman, and M. Mehregany, Appl. Phys. Lett. **78**, 162 (2001).
[4] K. Yasumura, T. Stowe, E. Chow, T. Pfafman, T. Keeny, B. Stipe, and D. Rugar, J. Microelectromech. Syst. **9**, 117 (2000).
[5] C. Nguyen and R. Howe, Proc. IEEE Intl. Freq. Control Symp. **48**, 127 (1994).
[6] K. Wang, A. Wong, and C. Nguyen, J. Microelectromech. Syst. **9**, 347 (2000).
[7] R. Lifshitz and M. Roukes, Phys. Rev. B **61**, 5600 (2000).
[8] F. Walls and J. Vig, IEEE Trans. Ultrason. Ferroelectr. Freq. Control **42**, 576 (1995).
[9] T. Gabrielson, IEEE Trans. Electron Devices **40**, 903 (1993).
[10] L. Cutler and C. Searle, Proc. IEEE **54**, 136 (1966).
[11] Y. Yong and J. Vig, IEEE Trans. Ultrason. Ferroelectr. Freq. Control **36**, 452 (1989).
[12] J. Vig and Y. Kim, IEEE Trans. Ultrason. Ferroelectr. Freq. Control **46**, 1558 (1999).
[13] A. Nowick and B. Berry, *Anelastic Relaxation in Crystalline Solids* (Academic, New York, 1972).
[14] T. Albrecht, P. Grütter, D. Horne, and D. Rugar, J. Appl. Phys. **69**, 668 (1991).
[15] S. Timoshenko, D. Young, and J. W. Weaver, *Vibration Problems in Engineering* (Wiley, New York, 1974).
[16] X. Huang, K. Ekinci, Y. Yang, C. Zorman, and M. L. Roukes, (unpublished).
[17] A. N. Cleland and M. L. Roukes, Sens. Actuators A **72**, 256 (1999).
[18] W. Egan, IEEE Trans. Instrum. Meas. **37**, 240 (1988).
[19] W. Robins, *Phase Noise in Signal Sources* (Peter Peregrinus Ltd., London, 1982).
[20] D. Allan, Proc. IEEE **54**, 221 (1966).
[21] W. Egan, *Frequency Synthesis by Phase Lock* (Wiley, New York, 1981).
[22] Hewlett-Packard 10811D/E application note.
[23] L. Landau, E. Lifshitz, and L. Pitaevskii, *Statistical Physics*, 4th ed. (Pergamon, Oxford, 1980).
[24] W. Mason and T. Bateman, Phys. Rev. A **134**, 1387 (1964).
[25] G. S. *et al.*, J. Phys. Chem. Solids **48**, 641 (1987).
[26] A. Zangwill, *Physics at Surfaces* (Cambridge University Press, New York, 1988).
[27] S. Roorda, W. C. Sinke, J. M. Poate, D. C. Jacobson, D. Dierker, B. S. Dennis, D. J. Eaglesham, F. Spaepen and P. Fuoss, Phys. Rev. B **44**, 3702 (1991).
[28] P. Dutta, P. Dimon, and P. Horn, Phys. Rev. Lett. **43**, 646 (1979).

Thermal conductance of nanostructured phononic crystals

A. N. Cleland,* D. R. Schmidt, and C. S. Yung
Department of Physics and iQUEST, University of California at Santa Barbara, Santa Barbara, California 93106
(Received 30 May 2001; published 15 October 2001)

The thermal conductance of mechanically suspended nanostructures has recently received much attention, in part due to the recent prediction and observation of the quantum limit for thermal conductance, which is observed in long, thin insulating beams at very low temperatures [D. E. Angelescu, M. C. Cross, and M. L. Roukes, Superlattices Microstruct. **23**, 673 (1998); K. Schwab, E. A. Henriksen, J. M. Norlock, and M. L. Roukes, Nature **404**, 974 (2000); I. G. C. Rego and G. Kirczenow, Phys. Rev. Lett. **81**, 232 (1998); M. P. Blencowe, Phys. Rev. B **59**, 4992 (1999)]. In this brief report, we describe a model calculation where the simple beam used to calculate quantum conductance [L. G. C. Rego and G. Kirczenow, Phys. Rev. Lett. **81**, 232 (1998)] is replaced by a beam made from an artificial one-dimensional phononic crystal. We find that at the lowest temperatures and longest thermal-phonon wavelengths, the quantum limit is recovered, while for intermediate temperatures, where the dominant phonon wavelength is of the order of the phononic-crystal repeat distance, a significant suppression of the conductance is predicted. At higher temperatures the conductance returns to that of a simple beam.

DOI: 10.1103/PhysRevB.64.172301 PACS number(s): 65.40.−b, 65.80.+n, 62.25.+g

The ability to fabricate suspended nanoscale structures that include temperature-sensitive and electronically active devices has allowed the development of highly sensitive mechanical electrometers and calorimeters, and the recent observation of the quantum of thermal conductance.[2,5–7] In bolometric- and calorimetric-detector applications, the energy sensitivity of the detector is ultimately limited by the nanostructure heat capacity $\mathcal{C}$ and the thermal conductance $\mathcal{G}$ linking the capacitance to a temperature reservoir. In general, smaller size structures yield smaller heat capacities. The thermal links, which also act as mechanical supports for the suspended structure, give increased thermal isolation with smaller cross sections and larger length-to-diameter aspect ratios. An example of a nanoscale bolometer is shown in Fig. 1. The device consists of a small block of single-crystal GaAs, suspended by four thin beams from the bulk substrate. A pair of superconductor–insulator–normal-metal (Al-I-Cu) double-tunnel junctions have been patterned on the surface of the suspended block, and act as heaters and thermometers allowing the measurement of the thermal conductance of the supports; a more complete description of this device will appear in Ref. 8.

The thermal conductance in this structure is determined by the conductance of the four thin beams supporting the central block; these comprise a 0.2-μm-thick GaAs beam with an overlying 0.05-μm-thick superconducting Al electrode. Operated well below the superconducting transition temperature, the thermal conductance is that of an electrical insulator, dominated by the thermal conductance through the delocalized phonon modes connecting thermal reservoirs at either end of the beam. The thermal conductance $\mathcal{G}$ is given by the formula[1,3,4,9]

$$\mathcal{G}=\frac{\hbar^2}{k_B T^2}\sum_n \frac{1}{2\pi}\int_0^\infty \mathcal{T}_n(\omega)\frac{\omega^2 e^{\hbar\omega/k_B T}}{(e^{\hbar\omega/k_B T}-1)^2}\,d\omega. \qquad (1)$$

Here n runs over the delocalized phonon modes in the beam, and $\mathcal{T}_n(\omega)$ is the phonon transmissivity for that mode at frequency ω; each mode has a continuum of transmitting frequencies. Most of the modes in a beam have low-frequency cutoffs similar to those for electromagnetic waves in a waveguide; a simple beam has only four modes that do not have such cutoffs, one longitudinal, one torsional, and two flexural modes. At the lowest temperatures, therefore, only these four modes can conduct energy, and if each of these modes has transmissivity $\mathcal{T}\rightarrow 1$, the thermal conductance approaches a universal quantum limit: $\mathcal{G}_Q=N(\pi^2 k_B^2/3h)T$, with $N=4$ being the number of low-frequency modes. In this low-temperature limit, the thermal conductance is independent of the beam length and cross section, and is proportional to T. This prediction for the thermal conductance has recently

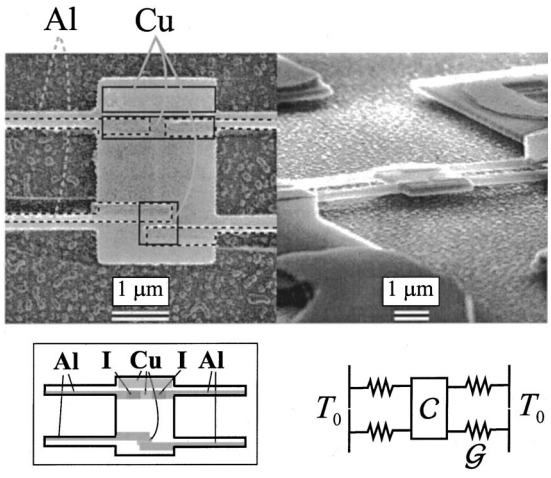

FIG. 1. Electron micrograph of a nanoscale bolometer, comprising a pair of Al-I-Cu-I-Al tunnel junctions fabricated on the surface of a $(2\times3\times0.2)$-μm^3 GaAs block, which is suspended by four $(0.2\times0.2\times4)$-μm^3 beams from the bulk substrate. Below is a sketch of the geometry including the tunnel junctions, and a highly simplified thermal model, indicating the heat capacitance $\mathcal{C}$ of the central block (dominated by that of the normal Cu metal), and thermal conductance $\mathcal{G}$ for each of the four beams.

been experimentally demonstrated by Schwab *et al.*[2]

The prediction for the low-temperature quantum limit $\mathcal{G}_Q$ appears to be quite robust. A recent calculation[9] includes the effect of surface roughness on the thermal conductance of a simple beam; the roughness causes elastic scattering between the allowed phonon modes, including scattering between forward-traveling and reverse-traveling phonons. The authors found that if the roughness has a correlation length Λ, then phonons with wavelengths much larger than or much smaller than Λ have a transmissivity approaching unity. The thermal conductance of a roughened beam is then given by the quantum limit for temperatures low enough that the characteristic phonon wavelength is larger than Λ, and returns to the dependence given by Eq. (1) for temperatures high enough that the dominant phonon wavelengths are much smaller than Λ. At temperatures between these limits, a moderate suppression of the conductance below $\mathcal{G}_Q$ is found, where the scattering is the strongest; this explains the corresponding suppression seen in the experiment[2] at intermediate temperatures.

In this paper, we investigate the thermal conductance for beams fabricated from beams made from artificial phononic crystals in the absence of scattering. Periodically modulated mechanical structures, which generate classical band structures, have been used for some time for applications in ultrasound and ultrasonic transducers;[10] a description of the current theoretical and experimental work appears in a review by Kushwaha.[11] The dispersion relation $\omega(k)$ for acoustic phonons traveling in a periodically modulated material is found to develop gaps in the transmission spectrum at wave vectors k associated with the modulation wave vector; these gaps should have an effect on the thermal conductance of a beam fabricated from such a material. We have calculated the dispersion relations for a periodically modulated, quasi-one-dimensional beam using two different acoustic models. We find that the resulting band structure, with gaps at frequencies that correspond to the phonons dominant at quite low temperatures, yields significant reductions in the thermal conductance from the quantum limit $\mathcal{G}_Q$ at moderate temperatures. However, the presence of delocalized Bloch states at the lowest phonon frequencies, below the gap, gives a thermal conductance that approaches $\mathcal{G}_Q$ at the lowest temperatures.

Our first model is for the longitudinal acoustic mode in a beam of variable cross section. x being the coordinate along the beam length, and $A(x)$ being the (position-dependent) cross-sectional area, the longitudinal displacement $u(x,t)$ satisfies the approximate one-dimensional equation[12,3]

$$\frac{1}{c_l^2}\frac{\partial^2 u}{\partial t^2}=\frac{\partial^2 u}{\partial x^2}+\frac{1}{A}\frac{\partial A}{\partial x}\frac{\partial u}{\partial x}, \tag{2}$$

where c_l is the longitudinal sound speed. We assume a periodic variation in the cross section A, of the form $\partial \ln A(x)/\partial x=\varepsilon G \sin Gx$, with amplitude ε and wave vector G (see inset to Fig. 2). The solutions to Eq. (2) can be expanded in the Bloch form with wave vector k and frequency ω,

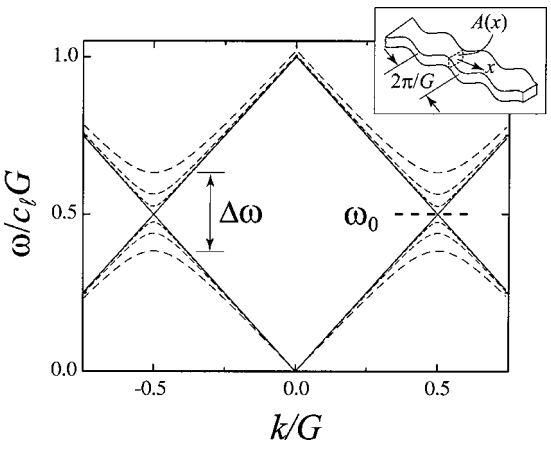

FIG. 2. Calculated dispersion relation for modulation strengths $\epsilon=0$, 0.1, 0.25, and 0.5 in the longitudinal acoustic model. The gap $\Delta\omega$ for $\varepsilon=0.5$ is indicated, as is the band-gap center frequency $\omega_0=c_lG/2$. Eleven bands were included in the calculation, the lowest two are shown here.

$$u(x,t)=\sum_{n=-\infty}^{\infty} U_n \exp[i(k+nG)x+i\omega t]. \tag{3}$$

In the limit $\varepsilon\to 0$, the terms in Eq. (2) with different n are decoupled and yield the dispersion relations $\omega^2=c_l^2(k+nG)^2$; these are drawn in Fig. 2 in a repeated-zone scheme. With nonzero ε, these terms become coupled, we numerically solve the eigenvalue equations Eq. (2).

We find that gaps $\Delta\omega$ open in the dispersion spectrum at the Brillouin-zone edges $k=\pm G/2$ corresponding to a frequency $\omega_0=c_lG/2$ in the center of the gap. In Fig. 2 we show the dispersion relations for the two lowest bands, for the unmodulated ($\varepsilon=0$) beam, and for a range of variational amplitudes ε. This structure therefore forms a one-dimensional phononic crystal, with a forbidden frequency band centered at ω_0, of magnitude $\Delta\omega/\omega_0\cong\varepsilon$.

As an example, a beam fabricated from Si with a thickness of 0.2 μm, can easily be patterned with a modulated width w varying from 0.1 to 0.5 μm with a periodicity of $2\pi/G=0.5\,\mu$m. The variational amplitude in Eq. (2) is then $\varepsilon=\frac{2}{3}$, and the corresponding bandgap is centered at $\omega_0=c_lG/2=33$ GHz. The calculation predicts a gap with bandwidth $\Delta\omega=22$ GHz, taking the sound speed $c_l=4300$ m/s.

In our second model we use a scalar phonon model of the type used by Santamore and Cross.[9] The scalar phonon displacement field $\Phi(\mathbf{r},t)$ satisfies the homogeneous wave equation with elastic modulus E and density ρ,

$$\rho\frac{\partial^2\Phi}{\partial t^2}=\boldsymbol{\nabla}\cdot(E\boldsymbol{\nabla}\Phi). \tag{4}$$

The beam is now fabricated as a composite structure with a periodic variation in the density and elastic modulus, so that $E=E(x)$ and $\rho=\rho(x)$, as sketched in Fig. 3. The beam has width w along the y axis and thickness t along z. We assume that the surfaces of the beam are stress-free, so that $\partial\Phi/\partial\hat{n}=0$ for a local surface normal $\hat{n}$ at $z=0,t$ and $y=0,w$.

The solutions to Eq. (4) are separable and have the form

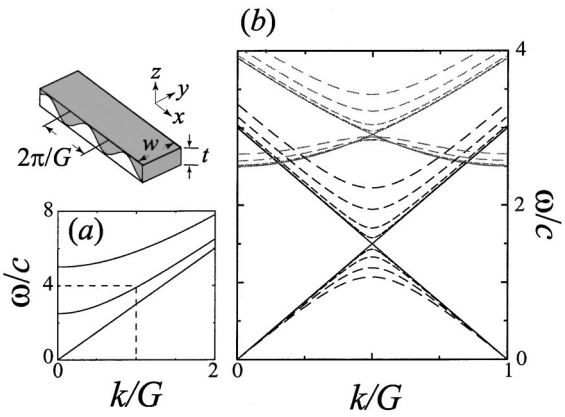

FIG. 3. (a) Dispersion relation for empty lattice, showing the three lowest modes for the scalar model, plotted in an extended-zone scheme. Dashed box shows the region plotted in detail in (b). (b) Dispersion relation including the structural modulation, plotted in the reduced-zone scheme. The calculation is for perturbation strengths $\delta=\epsilon=0.1$, 0.25, 0.5, and 0.75. Black solid and dashed lines are for the $(k_x,l,m)=(k_x,0,0)$ mode, and solid and dashed gray lines are for the $(k_x,1,0)$ mode. The geometric parameters were $w=2t$ and modulation wave vector $G=0.6\pi/t$. Inset shows the geometry for the structure.

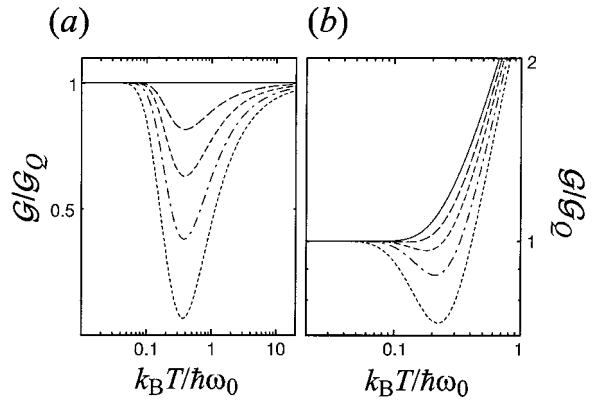

FIG. 4. (a) Calculated thermal conductance in units of the quantum of thermal conductance $\mathcal{G}_Q$ for one mode of a phononic crystal beam as a function of temperature normalized to the band-gap center ω_0. The solid line is for a simple beam showing the quantum value $\mathcal{G}/\mathcal{G}_Q=1$, and the dotted lines are for phononic crystal beams with band-gap widths $\Delta\omega/\omega_0=0.2$, 0.4, 0.6, and 1. The dotted line shows (b) Thermal conductance including the higher-order modes, for the simple beam (solid line) and for the same series of modulation widths $\Delta\omega/\omega_0$.

$$\Phi(\mathbf{r},t)=\phi(x)\cos k_{ly}\cos k_m z e^{i\omega t} \tag{5}$$

with transverse wave vectors $k_l=l\pi/w(l=0,1,2,...)$ and $k_m=m\pi/t(m=0,1,2,...)$. The function $\phi(x)$ satisfies

$$\frac{1}{\rho(x)}\left[E(x)k_l^2+E(x)k_m^2-\frac{\partial}{\partial x}E(x)\frac{\partial}{\partial x}\right]\phi=\omega^2\phi. \tag{6}$$

We assume that the elastic modulus has the spatial dependence $E(x)=E_0[1+\varepsilon\cos(Gx)]$ with a modulation amplitude ε and wave vector G; the inverse density has the same type of dependence, $1/\rho(x)=(1/\rho_0)[1+\delta\cos(Gx)]$, with amplitude δ. If ε and δ are taken to have the same sign, then an increase in elastic modulus is coupled with a decrease in density. The solutions to Eq. (6) have the same form as for our previous model with

$$\phi(x)=\sum_{n=-\infty}^{\infty}\phi_n e^{i(k_x+nG)x}. \tag{7}$$

Inserting this form into Eq. (6), we can calculate the eigenvalue solutions $\omega(k_x)$ for the modes (k_x,l,m). In the limit $\varepsilon,\delta\to 0$, the "empty-lattice" solutions $\omega^2=c_0^2(k_x^2+k_l^2+k_m^2)$ are found with wave velocity $c_0^2=E_0/\rho_0$. For nonzero ε and δ, we solve the coupled equations numerically; the solutions are plotted in Fig. 3 for the two lowest bands $(l,m)=(0,0)$ and $(l,m)=(1,0)$ as a function of longitudinal wave vector k_x. In the calculation we have retained terms of second order $\varepsilon\delta$, which mix wave vectors in band n with those in bands $n\pm 2$; dropping these does not significantly change the result shown in Fig. 3.

We again find that gaps open in the dispersion spectrum at the Brillouin-zone boundaries $k=\pm G/2$, with the magnitude for the gap between the lowest two bands approximately given by $\Delta\omega/\omega_0\cong\varepsilon$ for $\delta=\varepsilon$. If our composite structure consists of a 0.2-μm-thick beam of Si ($E=47$ GPa, $\rho=2330$ kg/m^3) combined with Pb ($E=16$ GPa, $\rho=11\,340$ kg/m^3), we have $\varepsilon\cong 0.5$ and $\delta\cong 0.65$, and we choose a periodicity $2\pi/G=0.5\,\mu$m. The calculation then yields a band center at $\omega_0=c_0G/2=14$ GHz with bandgap width $\Delta\omega=0.56\omega_0=8$ GHz.

These two approximate methods for calculating the dispersion relation of a one-dimensional phononic crystal yield rather similar results. We now consider what the implications are for the thermal transport through a beam fabricated with such a periodic structure. We assume that the beam is adiabatically coupled to thermal reservoirs at either end, using smooth, graduated increases in the cross-sectional area A to the bulk solid; we therefore avoid end-to-end phonon resonances,[3] and the acoustic mismatch from abrupt area transitions.[1,13] We calculate the temperature dependence of the thermal conductance for a single low-frequency Bloch mode with transmissivity $\mathcal{T}(\omega)$ equal to 1 for ω in the allowed bands, $0<\omega<\omega_0-\Delta\omega/2$ and $\omega>\omega_0+\Delta\omega/2$, and zero for ω in the forbidden gap region. The result of the calculation, using Eq. (1), is shown in Fig. 4(a), calculated for temperatures well below the cutoff temperature for the second mode [the mode $(k_x,1,0)$ in the scalar model, Eq. (4)]. In part (b) of that figure we display the temperature dependence including the higher-order modes.

At the lowest temperatures, such that the primary phonon frequency is much smaller than the lower band-gap edge $\omega_0-\Delta\omega/2$, the thermal conductance for the single mode is given by the quantum limit $\mathcal{G}_Q$. As the temperature is increased, the phonon distribution passes through the gap frequency ω_0, and the thermal conductance falls to a minimum at a temperature roughly given by $k_BT_{\min}\cong\hbar\omega_0/2.7$. Above this temperature, significant numbers of phonons populate the upper band; at high enough temperatures the result for a simple beam is recovered, with conduction occurring through a number of cutoff modes. This behavior is remark-

ably similar, although larger in magnitude, to that calculated for scattering due to imperfections in the surface of a simple beam, as shown by Santamore and Cross.[9] Here we can tune the amount by which the conductance is lowered at intermediate temperatures by increasing the width of the gap, and shift the point of minimum conductance by changing the crystal-repeat distance. However, at low enough temperatures the quantum of conductance will always be recovered.

For our two numerical examples cited above, the modulation of the cross-sectional width w of a Si beam from 0.1 to 0.5 μm yields a minimum in normalized thermal conductance at a temperature of 0.25 K, with a reduction by a factor of 0.7. For the composite modulated beam consisting of a modulated Si/Pb overlayer structure, the normalized conductance minimum is at 0.11 K, with a reduction factor of 0.57.

We have only considered the thermal conduction through effectively one of the four types of conducting modes in the beam. The other three modes will developed band gaps as well, at the same wave vectors $k_x = \pm G/2$, but at somewhat different center frequencies ω_0 due to the different acoustic sound speeds for these modes, and with different bandgaps $\Delta\omega$ due to the different coupling strengths. The total thermal conductance will consist of the superposed conductance associated with each mode and will therefore smear somewhat the features shown in Fig. 4. However, a significant feature should still be visible at intermediate temperatures.

In conclusion, we find that the quantum of conductance is quite robust, and for any given phononic crystal the thermal conductance at low enough temperatures will recover to the quantum limit. At moderate temperatures, however, the thermal conductance can be controllably reduced below the quantum limit, over a range of temperatures set by the fabrication parameters for the phononic crystal. This capability may prove useful in bolometric and calorimetric applications.

The authors thank Michael Geller for valuable discussions and a critical reading of the manuscript, and Robert Knobel for valuable conversations. We acknowledge the support provided by a NASA Explorer Award No. ECS-9980734, the Army Research Office under Contract No. DAAD-19-99-1-0226, and by a Research Corporation Research Innovation Award.

*Corresponding author. Email address: cleland@physics.ucsb.edu

[1] D. E. Angelescu, M. C. Cross, and M. L. Roukes, Superlattices Microstruct. **23**, 673 (1998).
[2] K. Schwab, E. A. Henriksen, J. M. Worlock, and M. L. Roukes, Nature (London) **404**, 974 (2000).
[3] L. G. C. Rego and G. Kirczenow, Phys. Rev. Lett. **81**, 232 (1998).
[4] M. P. Blencowe, Phys. Rev. B **59**, 4992 (1999).
[5] A. N. Cleland and M. L. Roukes, Nature (London) **320**, 160 (1998).
[6] M. L. Roukes, Physica B **263–264**, 1 (1999).
[7] P. Singha Deo, J. P. Pekola, and M. Manninen, Europhys. Lett. **50**, 649 (2000).
[8] C. S. Yung and A. N. Cleland (unpublished).
[9] D. H. Santamore and M. C. Cross, Phys. Rev. B **63**, 184306 (2001).
[10] M. Torres, F. R. Montero de Espinosa, and J. L. Aragón, Phys. Rev. Lett. **86**, 4282 (2001).
[11] M. S. Kushwaha, Int. J. Mod. Phys. B **10**, 977 (1996).
[12] Karl F. Graff, *Wave Motion in Elastic Solids* (Dover, New York, 1975).
[13] M. C. Cross and R. Lifshitz, cond-mat/0011501 (unpublished).

Single-crystal aluminum nitride nanomechanical resonators

A. N. Cleland[a)]
Department of Physics and The Institute for Quantum Engineering, Science and Technology, University of California at Santa Barbara, Santa Barbara, California 93106

M. Pophristic and I. Ferguson
Emcore Corporation, 145 Belmont Drive, Somerset, New Jersey 08873

(Received 21 May 2001; accepted for publication 3 July 2001)

Aluminum nitride is a light, stiff, piezoelectrically active material that can be epitaxially grown on single-crystal Si. AlN is beginning to play a role in the integration of semiconducting electronic and surface acoustic wave devices, and may prove useful for the integration of other types of mechanical devices as well. We describe the growth and subsequent electron-beam patterning and etching of epitaxial AlN-on-silicon films into nanomechanical flexural resonators. We have measured resonators with fundamental mechanical resonance frequencies above 80 MHz, and quality factors in excess of 20 000. © *2001 American Institute of Physics.* [DOI: 10.1063/1.1396633]

Aluminum nitride is proving to be a useful material in the semiconductor industry, as it can be grown epitaxially on ⟨111⟩ Si substrates, typically by metalorganic chemical vapor deposition (MOCVD), forming high quality, smooth films with the *c* axis oriented along the growth direction. AlN is a very light ($\rho = 3255\,\mathrm{kg/m^3}$), stiff material, with a Young's modulus of 345 GPa and a *c*-axis sound velocity of 11.4 km/s. The large piezoelectric constant $e_{33} = 1.5\,\mathrm{C/m^2}$ corresponds to an electromechanical coupling constant $k^2 = 6.5\%$.[1] Aluminum nitride is fracture resistant and chemically nonreactive, with negligible etching rates when exposed to most strong acids and bases.[2]

This material is a clear candidate for the integration of surface-acoustic wave devices on chip with silicon-based electronics. In addition, it can be used to fabricate submicron-scale cantilevers and flexural beams. Such suspended, mechanically active structures allow applications in force microscopy, optical couplers, and stable oscillators and filters. Other materials under development for these applications include Si, both single crystal and polycrystalline, polycrystalline silicon nitride, GaAs, and silicon carbide.[3–10] Mechanical actuation and sensing in most of these materials relies on electrostatic, optical, or magnetomotive techniques, which suffer from poor coupling and implementation difficulties. Aluminum nitride, by contrast, provides both the possibility for very high resonance frequencies and piezoelectric actuation.

We have developed a method to fabricate radio frequency flexural resonators from single-crystal AlN films. Here we describe the fabrication process, as well as measurements demonstrating fundamental resonance frequencies above 80 MHz and very high quality factors, in excess of 2×10^4.

The AlN films samples were grown on ⟨111⟩ Si wafers in a multiwafer, rotating disk MOCVD system under low-pressure conditions. Triethylaluminum (TEA) and ammonia (NH_3) were used as the Al and N precursors, with H_2 as the carrier gas. Low pressures were used to accommodate the low vapor pressure of TEA, and to minimize pre-reactions. Prior to buffer layer growth, the Si wafers were etched for 20 s in 10% hydrofluoric acid. The wafers were then heated for 10 min at 900 °C in a H_2 atmosphere, leaving an atomically clean surface for epitaxy. An AlN nucleation layer (25 nm thick) was then grown at an approximate surface temperature of 550 °C and TEA and NH_3 flows of 0.6 μmoles/min and 1.1 moles/min, respectively. The AlN epilayer was then grown at 1100 °C, with a TEA flow of 0.9 μmoles/min, establishing a V/III ratio of 12 000; a growth rate of 0.15 μm/h can thereby be achieved. Film thicknesses were measured by optical interferometry to be $t = 0.17\,\mu$m. A more detailed description of the growth system and process can be found elsewhere.[11]

Flexural resonators were fabricated using a combination of optical and electron beam lithographies. Optical lithography was used to define a liftoff pattern for large-scale wire-bond pads, which consisted of a 3 nm thick Ti adhesion layer followed by a 110 nm thick Au film. Electron-beam lithography was then used to define a liftoff pattern for a metal electrode that runs along the length of each resonator for magnetomotive excitation.[5] The electrode comprised a 3 nm Ti adhesion layer, a 35 nm Au film, and a 60 nm Ni film; the Ni served as an etch mask for the anisotropic reactive ion etch of the AlN. Beam lengths ranged from 3.6 to 5.9 μm, with 0.2 μm widths. The ends of the beams were defined by a step increase in the width to 2.4 μm.

The electrode pattern was transferred to the AlN film using anisotropic Cl_2-based reactive ion etching (RIE). Samples were placed in a parallel-plate load-locked RIE chamber, which was pumped to 5×10^{-7} Torr. Chlorine gas was admitted at 10 sccm, with a chamber pressure of 5 mTorr. A rf plasma was ignited with 200 W of rf power, yielding a substrate voltage of 400 V. The AlN etch rate was approximately 150 nm/min, with very vertical sidewalls. The etch rate for the Si substrate and the Ni mask was negligible in these conditions.

The Ni was then removed using a commercial Ni etchant,[12] and the structures released by etching the Si sub-

a)Author to whom correspondence should be addressed; electronic mail: cleland@physics.ucsb.edu

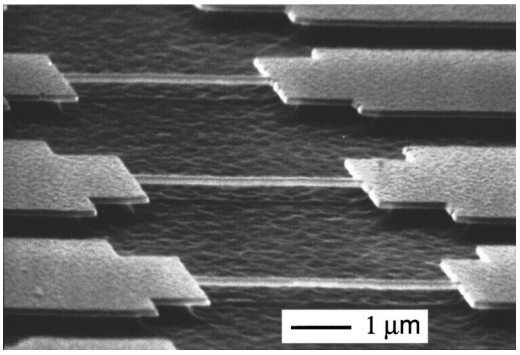

FIG. 1. Series of four AlN beams, with the undercut lengths ranging from 3.9 to 5.6 μm. The beams are 0.17 μm thick, and the widths are 0.2 μm, increasing to widths of 2.4 μm at either end.

strate with an isotropic wet etchant [5 parts ammonium fluoride:120 parts nitric acid:60 parts de-ionized (DI) water[13]]. A 15 s etch was sufficient to mechanically free the resonators; the structures were rinsed in methanol, and dried in air. Structures fabricated in this way did not in general collapse, obviating the need for CO_2 critical point drying. An electron micrograph of a set of completed beams in shown in Fig. 1. Note that the narrow part of the beams is completely undercut, while the wider steps are undercut to a depth of approximately 0.3 μm. We take the nominal length L of the beam to be the length measured from the edge of the undercut at either end; the lengths for the beams we describe here ranged from 3.9 to 5.6 μm.

Electrical contacts to the completed resonators were made with Au wire bonds, and the structures were placed in a vacuum can, which was evacuated and then submerged in liquid helium, in the bore of an 8 T magnet. A semirigid 50 Ω coaxial cable connected room-temperature electronics to each resonator. The center pin of the cable was connected to one end of each resonator, with the other end of the resonator grounded. The resonators were oriented with the plane of the sample parallel to the magnetic field, with the beam length perpendicular to the field B, allowing magnetomotive measurement of the beam resonance frequency Ω and quality factor Q.[5] A typical measurement is shown in Fig. 2 for a 3.3 μm long beam, displaying clear resonance at $\Omega/2\pi$

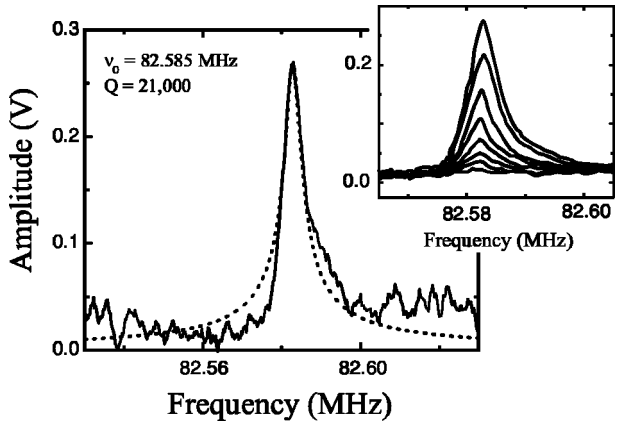

FIG. 2. Measured resonance of a 3.9 μm long beam, measured at 4.2 K in a transverse magnetic field of 8 T. The applied rf power was -85 dBm. Inset: Measured resonance for a constant rf power of -75 dBm, while varying the magnetic field through integer values from 1 T (smallest peak) to 8 T (largest peak).

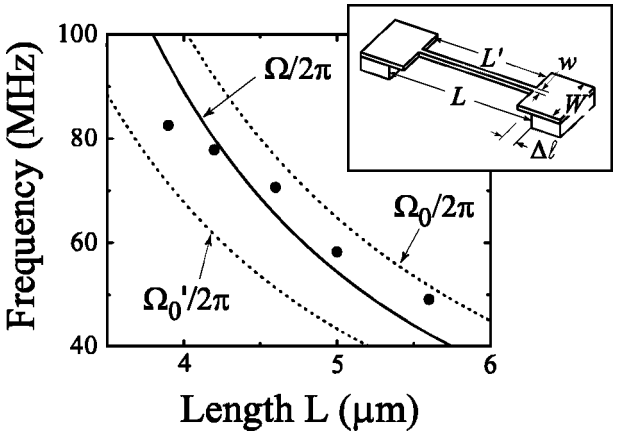

FIG. 3. Measured resonance frequencies for five beam lengths (closed points), with calculated resonance frequencies $\Omega_0(L)/2\pi$ using the nominal beam length L (dotted line), $\Omega_0'(L)/2\pi$ adjusted for Au mass loading (dashed line), and $\Omega/2\pi$ using the numerically calculated frequency accounting for the stepped beam width (solid line). Inset: Geometry defining the beam width $w=0.12$ μm, step width $W=2.4$ μm, nominal length L and effective length $L'=L-2\Delta\ell$.

$=82$ MHz with a quality factor $Q=2.1\times10^4$. Varying the magnetic field for a fixed rf drive power shows the expected quadratic dependence on magnetic field, shown in the inset in Fig. 2.

We measured a number of resonators with different beam lengths but fixed widths; the measured dependence of resonance frequency on nominal beam length L is shown in Fig. 3, along with three theoretical curves.

The resonance frequency Ω for a flexural beam of thickness t, width w and length L is given by solving the Euler–Bernoulli beam equation,

$$-\rho A\Omega^2 Y=\frac{\partial^2}{\partial x^2}EI\frac{\partial^2 Y}{\partial x^2}, \tag{1}$$

where $Y(x)$ is the displacement along the thickness axis, x is measured along the beam length, ρ and E are the density and elastic modulus, $A=wt$ the cross-sectional area, and $I=wt^3/12$ the bending moment of inertia; these parameters can be position dependent.

For a doubly clamped beam with uniform material and geometric parameters, Eq. (1) yields solutions with the natural resonance frequency $\Omega_0(L)$ given by

$$\frac{\Omega_0(L)}{2\pi}=1.027\sqrt{\frac{E}{\rho}}\frac{t}{L^2}. \tag{2}$$

The elastic modulus for an AlN beam with length along the $\langle1000\rangle$ crystal direction and flexure in the $\langle0001\rangle$ direction is given by $E=(c_{11}-c_{12})(c_{11}+2c_{12})/(c_{11}+c_{12})=280$ GPa.[1,10,14] This predicted curve is shown as a dotted line in Fig. 3.

The resonators include a thin Au film, with $\rho=19320$ kg/m^3 and $E=78$ GPa (the Ti wetting layer has a negligible effect). The main effect of the metal is to mass load the resonator, reducing its frequency from that given by Eq. (2). For the large ratio of AlN thickness t_1 to the metal thickness t_2, the resonance frequency for the composite structure is approximately[10]

$$\frac{\Omega_0'(L)}{2\pi} \approx 1.027 \frac{E_1}{\rho_1} \frac{1}{\sqrt{1+\rho_2 t_2/\rho_1 t_1}} \frac{t_1}{L^2}. \quad (3)$$

By evaluating Eq. (3) for our structures, we find a mass-loaded frequency $\Omega_0'(L) \approx 0.67\,\Omega_0(L)$, in terms of the bare resonance frequency $\Omega_0(L)$. This curve is plotted as a dashed line in Fig. 3.

A second correction involves the fact that the beams are not uniform in width along the suspended length, but comprise a 0.2 μm wide section of length L', followed by a short section with width 2.4 μm and undercut length $\Delta\ell = 0.3\,\mu$m at either end. The nominal length L is given by $L = L' + 2\Delta\ell$. One way to approximate the effect of the width increase is to take the effective length L' in Eqs. (2) and (3), assuming that the wider section of the beam is rigidly clamped. However, the increase in beam stiffness provided by the width increase is not equivalent to clamping the beam, so this does not yield an accurate result.

We therefore used a version of Stodola's iterative method,[15] in which the flexure equation, Eq. (1), is solved numerically for the actual beam geometry, yielding an excellent approximation to the actual mode shape $Y(x)$. The resonance frequency may then be evaluated using Rayleigh's method.[16] We have applied this technique to the beam geometry shown in the inset in Fig. 3. The resulting corrections are $\Omega(L)/\Omega_0'(L) = 1.26-1.41$; the correction varies with the proportion $\Delta\ell/L$. In Fig. 3 we show this calculated frequency as a solid line, showing a fairly good correspondence to the measured dependence, with no adjustable parameters.

In conclusion, we have described the fabrication and measurement of high frequency nanomechanical beams, fabricated from single-crystal AlN and measured using a magnetomotive technique. In addition, we find that we can fairly accurately account for the beam frequencies when adjusting for mass loading and for the specific beam geometry. Applications of these types of structures to piezoelectrically driven and detected beam resonances are presently underway.

The authors gratefully acknowledge the support provided by National Science Foundation XYZ-on-a-Chip award, Award No. ECS-9980734, the Army Research Office under Contract No. DAAD-19-99-1-0226, and by a Research Corporation Research Innovation Award.

[1] O. Ambacher, J. Phys. D **31**, 2653 (1998).
[2] J. R. Mileham, S. J. Pearton, C. R. Abernathy, J. D. Mackenzie, R. J. Shul, and S. P. Kilcoyne, J. Vac. Sci. Technol. A **14**, 836 (1995).
[3] Z. Zhang and N. MacDonald, J. Microelectromech. Syst. **2**, 66 (1993).
[4] N. MacDonald, Microelectron. Eng. **32**, 49 (1996).
[5] A. Cleland and M. Roukes, Appl. Phys. Lett. **69**, 2653 (1996).
[6] A. Cleland and M. Roukes, Nature (London) **320**, 160 (1998).
[7] C. Nguyen and R. Howe, Proc. IEEE **48**, 127 (1994).
[8] K. Wang, A. Wong, and C. Nguyen, J. Microelectromech. Syst. **9**, 347 (2000).
[9] R. Beck, M. A. Eriksson, M. A. Topinka, R. M. Westervelt, K. D. Maranowski, and A. C. Gossard, Appl. Phys. Lett. **73**, 1149 (1998).
[10] Y. T. Yang, K. L. Ekinci, X. M. H. Huang, L. M. Schiavone, M. L. Roukes, C. A. Zorman, and M. Mehregany, Appl. Phys. Lett. **78**, 162 (2001).
[11] C. Tran, R. Karlicek, Jr., M. Schurman, T. Salagaj, R. Cassidy, I. Ferguson, A. G. Thompson, R. A. Stall, and C.-Y. Hwang, J. Cryst. Growth **174**, 647 (1997).
[12] T. C. Inc.
[13] E. Williams and R. Muller, J. Microelectromech. Syst. **5**, 256 (1996).
[14] B. Auld, *Acoustic Fields and Waves in Solids* (Wiley, New York, 1973), Vol. I.
[15] J. D. Hartog, *Mechanical Vibrations* (Dover, New York, 1985).
[16] S. Timoshenko, D. Young, and J. W. Weaver, *Vibration Problems in Engineering* (Wiley, New York, 1974).

Nanoelectronic and nanomechanical systems

J.S. Aldridge, R. Knobel,
D.R. Schmidt, C.S. Yung and A.N. Cleland *
Department of Physics and iQUEST, University of California at Santa Barbara, Santa Barbara CA 93106
(Dated: September 20, 2001)

Nanomechanical systems, integrated with nanoelectronic transducers and sensors, are in an early stage of development. Research is focused on the development of radiofrequency mechanical resonators, sensitive electrometers and magnetometers, and potentially quantum-limited energy and motion sensors. This paper will review the current state of our efforts in this area, and will describe research in which the integration of mechanics and electronics will potentially allow the demonstration of macroscopic quantum effects in mechanical systems. We are particularly interested in observing and measuring quantum-limited systems, whose behavior is strongly affected by the measurement system; such systems may provide further insight into the quantum measurement process.

Keywords: Nanomechanics, nanoelectronics, single electron transistor, bolometer

We are developing a number of novel approaches for the integration of electrical systems with the mechanical degrees of freedom in nanometer-scale structures. Our central theme is to unify the very sensitive characteristics of tunnel junctions with mechanically suspended structures. Projects underway include the development of a nanoscale bolometer comprising a suspended structure with a very small heat capacity, weakly linked to the environment, mechanically suspended beams with an integrated two-dimensional electron gas, and flexural resonators electrically coupled to single electron transistors, which act as displacement sensors.

I. FLEXURAL RESONATORS

Flexural resonators, either in the form of cantilevers or doubly-clamped beams, form a basic element in nanomechanical structures. A doubly-clamped resonator with thickness t and length L has a fundamental flexural resonance frequency given by

$$\frac{\Omega_0}{2\pi} = 1.027\sqrt{\frac{E}{\rho}}\,\frac{t}{L^2}. \tag{1}$$

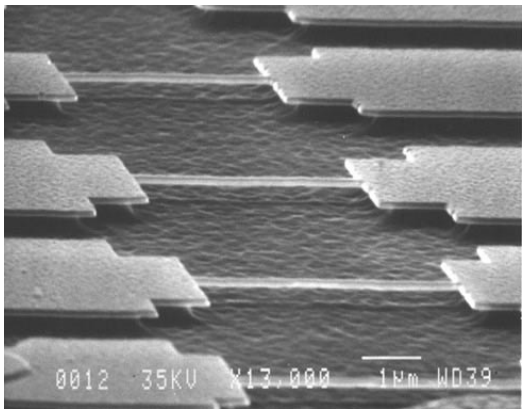

FIG. 1: Series of four AlN beams, with the undercut lengths ranging from 3.9 to 5.6 μm. The beams are 0.17 μm thick, and the widths are 0.2 μm, increasing to widths of 2.4 μm at either end.

* Corresponding author: E-mail: cleland@physics.ucsb.edu

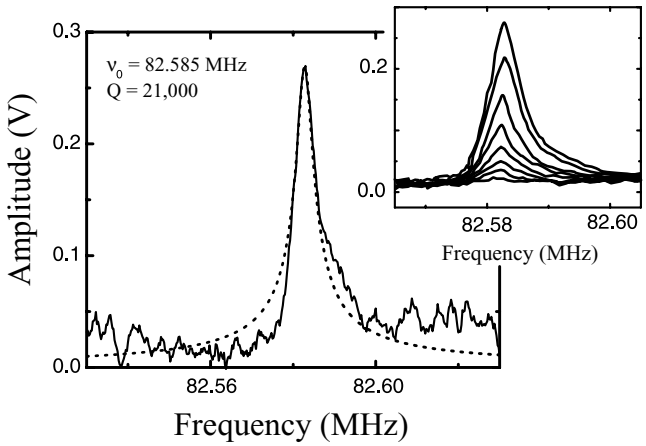

FIG. 2: Measured resonance of a 3.9 μm long beam, measured at 4.2 K in a transverse magnetic field of 8 T. Applied rf power was -85 dBm. *Inset:* Measured resonance for a constant rf power of -75 dBm, while varying the magnetic field through integer values from 1 T (smallest peak) to 8 T (largest peak).

A beam fabricated from Si with thickness $t = 0.2$ μm and a length of 100 μm has a resonance frequency of about 170 kHz; shortening the length to 10 μm increases the frequency to 17 MHz, and a further reduction to 1 μm brings the frequency up to 1.7 GHz. Quality factors for the fundamental resonance have been measured in excess of 20,000 [1, 2]. Such resonators form candidates as stable local oscillators for time-base and frequency standards applications [3, 4].

These structures are coupled to external electronic circuitry using a number of methods: through magnetomotive transduction, through electrostatic displacement sensing and actuation, and through the piezoelectric effect. The magnetomotive technique [1, 5] involves placing the mechanically active element in a transverse magnetic field, and passing a current through a metal film integrated with the mechanical structure. A Lorentz force develops as a result, generating a displacement; the displacement then generates an electromotive voltage, which can be sensed using external electronics.

In Fig. 1 we show a set of flexural beams fabricated from single-crystal aluminum nitride. We have been developing this material because of its low density, high elastic modulus, and relatively high fracture strength. This material can be grown as single crystal films on $\langle 111 \rangle$-orientation Si wafers using metal-organic chemical-vapor deposition. The films can subsequently be patterned using a combination of electron beam lithography and thin metal film deposition. The AlN can be anisotropically etched using Cl_2-based reactive ion etching, and the substrate Si selectively removed using an isotropic Si etch (ammonium fluoride, nitric acid and water). More fabrication details are discussed below.

The structures shown in Fig. 1 were measured using the magnetomotive technique; a series of resonance curves is shown in Fig. 2. Resonance frequencies have been measured [2] in the range of 40-80 MHz, with quality factors measured to be somewhat higher than 20,000.

The electrostatic approach involves the use of displaceable capacitors, where a voltage applied across the plates of a mechanically flexible capacitor causes one plate to displace with respect to the other. The displacement can be detected by monitoring the resulting change in capacitance [3]. An example of a nanoscale structure with electrostatic drive and sense, fabricated from single-crystal Si using a silicon-on-insulator substrate as the base material, is shown in Fig. 3.

II. SET-BASED DISPLACEMENT SENSING

We are attempting to develop a potentially quantum-limited displacement sensing approach, based on the single-electron transistor (SET). The structure we are fabricating comprises a doubly-clamped flexural beam, coupled through a capacitive, mechanically variable capacitor to the gate lead of the SET. A micrograph of a completed structure, with doubly-clamped beam and adjacent single-electron transistor, is shown in Fig. 4. The

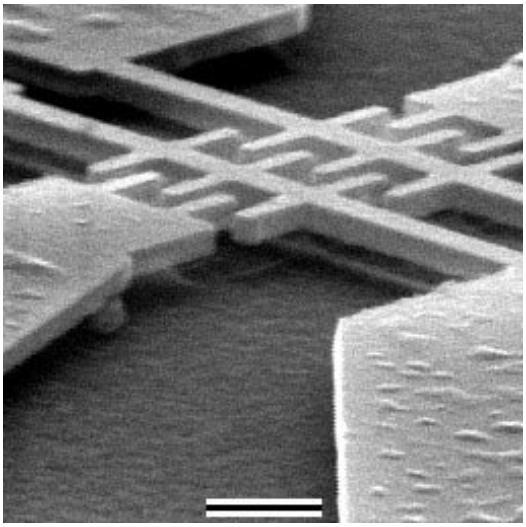

FIG. 3: Single-crystal silicon flexural resonators coupled by capacitive transducers, allowing both displacement actuation and sensing. The horizontal scale bar is 1 μm. The flexural resonance frequency of these structures is measured to be 68 MHz.

mechanical beam can be driven using an external signal, using magnetomotive displacement; it will also exhibit thermally-driven fluctuations due to its finite value of damping, parameterized by the quality factor Q. Further, as discussed below, we expect the beam to exhibit motion driven by the back-action measurement noise from the SET. The beam can be biased with a dc voltage V_0, which induces a coupling charge on the capacitor; motion of the beam changes the charge coupled to the single-electron transistor, modulating the drain-source current in the transistor.

In a recent innovation [6], the SET can be used as a radio-frequency electrometer, for which the input charge noise has been measured to be about $2\times10^{-5}\ e/\sqrt{\text{Hz}}$. There has been a proposal to use the SET as a displacement sensor [7], estimating the displacement sensitivity when it is coupled to a radiofrequency resonator, and a recent estimate of the magnitude of the electrical back action generated by the SET on the resonator [8].

The displacement of the resonator is sensed by changes in the coupling capacitance C_c and the corresponding coupled charge. The sensitivity of the SET as a displacement sensor is determined by its charge sensitivity, by the sensitivity of the coupling capacitance on the resonator displacement, and by the magnitude of the SET back-action on the mechanical resonator. The back-action is caused by the force exerted on the resonator when the voltage on the center island of the SET fluctuates. This can be evaluated as follows: The electrostatic charging energy of the coupling capacitance is $\varepsilon = C_c V_c^2/2$, where $C_c(x)$ is the position-dependent capacitance, and x is the displacement at the midpoint of the resonator; the voltage V_c is the voltage across the coupling capacitor. This voltage consists of the externally-imposed voltage V_0 and a noise voltage δV, which fluctuates due to the stochastic nature of electron flow through the SET.

The electrostatic force generated by V_c is given by $F = d\varepsilon/dx = (V_c^2/2)dC_c/dx$. A fluctuation δV in the voltage V_c gives rise to a fluctuation δF in the force through

$$\delta F = V_0 \frac{dC_c}{dx}\ \delta V, \tag{2}$$

where V_0 is the constant value of V_c.

Following Schwab [8], the noise voltage δV can be evaluated using the amplifier noise model developed for the SET by Devoret and Schoelkopf [9]. It has a spectral density due to the SET input current noise $S_I(\omega)$ driving the coupling capacitance C_c, given by $S_I(\omega)/\omega^2 C_c^2$. The spectral noise density $S_F(\omega)$ of the force on the resonator is then given by

$$S_F(\omega) = \left(V_0 \frac{dC_c}{dx}\right)^2 \frac{S_I(\omega)}{\omega^2 C_c^2(x)}, \tag{3}$$

An optimized SET, with both tunnel junction resistances equal to the quantum of resistance $h/e^2 \approx 25$ kΩ, has a current noise that at low frequencies is approximately given by

$$S_I(\omega) = \frac{5}{9} \frac{C_c^2(x)}{C_\Sigma} h\omega^2, \tag{4}$$

where C_Σ is the total capacitance of the SET island.

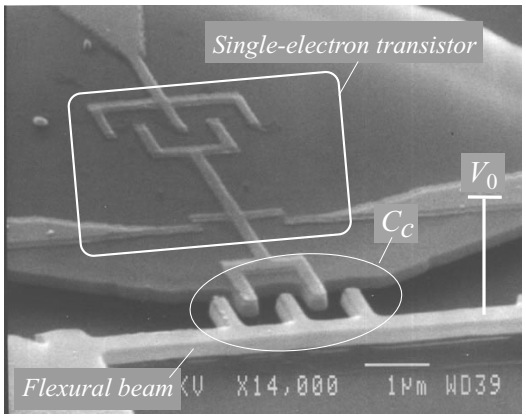

FIG. 4: Electron micrograph of a doubly-clamped beam coupled to a single-electron transistor. The resonating beam includes an interdigitated capacitor $C_c(x)$ coupled to the gate of the single-electron transistor; the displacement x of the beam center point changes the coupled charge, and modulates the current through the transistor. The beam can be biased with a dc voltage V_0.

The displacement spectral density $S_x(\omega)$ may then be evaluated using the response function of the resonator; for a resonator with mass M, resonance frequency Ω_0 and quality factor Q, this is related to the force spectral density $S_F(\omega)$ by

$$S_x(\omega) = \frac{1}{(\Omega_0^2 - \omega^2)^2 + (\omega_0^2/Q)^2} \frac{S_F(\omega)}{M^2\Omega_0^4}. \tag{5}$$

For a high quality factor resonator, with $Q \gg 1$, the response (5) is very narrow-band, so the spectral density of the force (3) may be taken to be frequency-independent, with $S_I(\omega)$ evaluated at $\omega = \Omega_0$.

The back-action noise of the SET can now be re-stated as an effective noise temperature: The dissipation associated with a finite value of the quality factor Q generates a fluctuating force of magnitude [4]

$$S_F(\omega) = \frac{2k_B T_{\rm eff} M\Omega_0}{\pi Q}, \tag{6}$$

where $T_{\rm eff}$ is the temperature; this relation is determined by the fluctuation-dissipation theorem. For the SET, we therefore can define an effective noise temperature

$$T_{\rm eff} = \frac{5\pi}{18k_B} \frac{QV_0^2}{M\Omega_0} \left(\frac{dC_c}{dx}\right)^2 \frac{h}{C_\Sigma}. \tag{7}$$

In addition to the SET-driven noise, the resonator has a physical temperature T, so in the classical limit $k_B T \gg \hbar\Omega_0$, the total noise amplitude of motion corresponds to a temperature $T + T_{\rm eff}$.

This motion is sensed by the SET, with a displacement sensitivity determined by the coupling of the resonator to the SET and the SET input voltage noise $S_V(\omega)$. The voltage noise for an optimized SET is given by

$$S_V(\omega) = \frac{65hC_\Sigma}{288C_c^2(x)}, \tag{8}$$

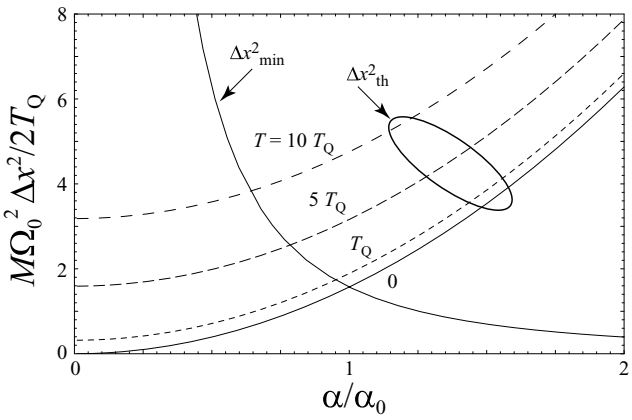

FIG. 5: Displacement noise energy as a function of coupling strength α/α_0, for different resonator temperatures in units of the temperature quantum $T_Q = \hbar\Omega_0$. The optimal coupling is achieved when the minimum displacement energy is equal to the thermal energy.

and is approximately white. Referring the voltage noise as a effective displacement noise $S_{x\,\rm eff}$, we have

$$\begin{aligned} S_{x\,\rm eff}(\omega) &= \left(\frac{C_c(x)}{V_0}\frac{1}{dC_c/dx}\right)^2 S_V(\omega) \\ &\approx \frac{hC_\Sigma}{4V_0^2(dC_c/dx)^2}. \end{aligned} \tag{9}$$

The thermally-driven displacement has a frequency spectrum concentrated in the band centered on Ω_0 with a width $\Delta\Omega = 2\Omega_0/Q$; integrating the noise power over this band, we find a mean square noise

$$\Delta x^2_{\rm th} = \int_{\Delta\Omega} S_x(\omega)d\omega \approx 1.11\frac{2k_B(T+T_{\rm eff})}{\pi M\Omega_0^2}. \tag{10}$$

The input displacement noise of the SET integrated over the same band gives a minimum detectable square displacement

$$\Delta x^2_{\rm min} = S_{x\,\rm eff}\,\Delta\Omega = \frac{h\Omega_0 C_\Sigma}{2QV_0^2(dC_c/dx)^2}. \tag{11}$$

The coupling strength $\alpha = V_0 dC_c/dx$ can be tuned by adjusting the dc voltage V_0; increasing the voltage reduces the minimum detectable displacement $\Delta x_{\rm min}$, but also increases the effective temperature $T_{\rm eff}$. At zero resonator physical temperature $T = 0$, the optimum coupling α_0 is achieved when $\Delta x_{\rm th} = \Delta x_{\rm min}$, or when

$$\alpha_0 = V_0\frac{dC_c}{dx} = \sqrt{\frac{M\Omega_0^2 C_\Sigma}{Q}}. \tag{12}$$

At this optimal bias point, the minimum displacement noise is $\Delta x^2_{\rm min} = h/2M\Omega_0$, close to that given by the standard quantum limit of $\hbar/2M\Omega_0$. Taking a model resonator of $\Omega_0 = 2\pi\times 10^8$ Hz, mass $M = 3\times 10^{-16}$ kg, the rms displacement noise is 4×10^{-14} m.

At non-zero resonator temperatures, the optimal coupling value α decreases. In Fig. 5 we show the dependence of the thermal and back action-driven displacement energy $M\Omega_0^2\Delta x^2_{\rm th}/2$, and the corresponding detectable energy $M\Omega_0^2\Delta x^2_{\rm min}/2$, as a function of coupling strength. The thermal energy is calculated for a number of resonator temperatures, in units of the quantum temperature $T_Q = \hbar\Omega_0/k_B$. The optimal bias voltage V_0 is determined by the point at which the minimum detectable energy intersect the thermally-driven motion.

III. NANOSCALE BOLOMETER

A second major project is aimed at the development of nanoscale bolometers, with the potential for substantially increased sensitivity to infrared light in the frequency range of 0.1-10 THz. A bolometer consists of a volume whose temperature is changed by absorbing infrared light, and a thermistor element that detects the changes in temperature. The volume has a heat capacity $\mathcal{C}$, a thermal conductance to the temperature bath $\mathcal{G}$, and a corresponding thermal time constant $\tau = \mathcal{C}/G$. The minimum detectable radiated power, called the noise equivalent power (NEP) is set by thermal fluctuations through the thermal conductance, and is equal to $NEP = \sqrt{4k_B T^2 \mathcal{G}}$. Operating at lower temperatures with smaller thermal conductances leads to smaller values of the NEP.

There is a however a quantum limit to the minimum achievable thermal conductance, first predicted theoretically [10–13] and later verified experimentally [14]. For a thermal conductance formed by a nanoscale wire, this quantum limit is achieved at low temperatures and is given by

$$\mathcal{G}_Q = \frac{4\pi^2 k_B^2 T}{3h}, \tag{13}$$

where h is Planck's constant. The corresponding limit to the noise equivalent power is given by

$$NEP = \left(\frac{16\pi^2 k_B^3 T^3}{3h}\right)^{1/2}. \tag{14}$$

At a temperature of 100 mK, this corresponds to 5×10^{-19} W/Hz$^{1/2}$; at 20 mK this is 4×10^{-20} W/Hz$^{1/2}$, values that are 10-100 times smaller than is presently achievable.

Even smaller values should be achievable by engineering the thermal link that provides the conductance $\mathcal{G}$. The quantum limit (13) is achieved for a straight wire with unity phonon transmissivity; conductances smaller than this can be achieved by engineering the phonon dispersion relation for transmission through the conductance. We have completed calculations that indicate that a periodically modulated structure, forming a phononic bandgap, can for a range of temperatures achieve a thermal conductance significantly less than the quantum limit [15]. An example of such a structure and its dispersion relation is shown in Fig. 6.

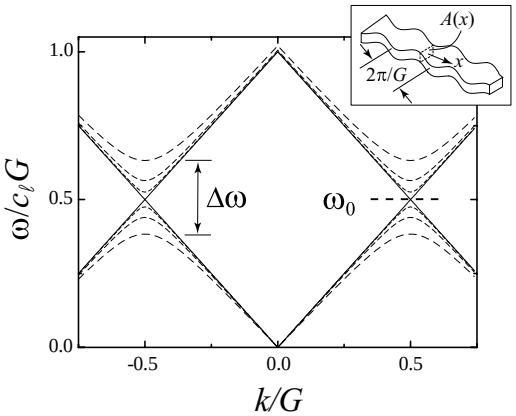

FIG. 6: Calculated dispersion relation for different modulation strengths, using a longitudinal acoustic model. The gap $\Delta\omega$ is indicated, as is the bandgap center frequency ω_0.

The corresponding calculation for the thermal conductance, in units of the quantum of thermal conductance, is shown in Fig. 7.

Structures such as these may prove useful in tuning and adjusting the thermal conductance of nanoscale structures.

We are presently fabricating and characterizing a nanometer-scale bolometer, for which we use a mechanically suspended volume of semi-insulating GaAs, which is patterned using electron-beam lithography to define a

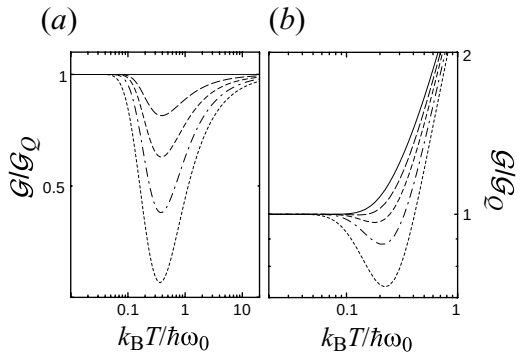

FIG. 7: (a) Calculated thermal conductance in units of the quantum of thermal conductance $\mathcal{G}_Q$, for one mode of a phononic crystal beam, as a function of temperature normalized to the bandgap center ω_0. The solid line is for a simple beam, showing the quantum value $\mathcal{G}/G_Q = 1$, and the dotted lines are for phononic crystal beams with bandgap widths $\Delta\omega/\omega_0 = 0.2$, 0.4, 0.6 and 1. (b) Thermal conductance including the higher order modes, for the simple beam (solid line) and for the same series of modulation widths $\Delta\omega/\omega_0$.

volume, $2 \times 3 \times 0.2$ μm^3, suspended by thin, $4 \times 0.2 \times 0.2$ μm^3 legs from the bulk substrate. The thermistor element is a aluminum-aluminum oxide-copper-aluminum oxide-aluminum tunnel (SINIS) junction, fabricated on the surface of the GaAs. The volume of copper normal metal is $3 \times 0.3 \times 0.04$ μm^3, and the tunnel characteristics of the junction are sensitive to the temperature of the electrons in this normal metal. A electron micrograph and sketch of the structure appears in Fig. 8. This structure has a heat capacity approximately 10^4 times smaller than micromachined bolometers, and we anticipate bolometric sensitivity of order 100 times higher than in these other bolometer designs [16–18].

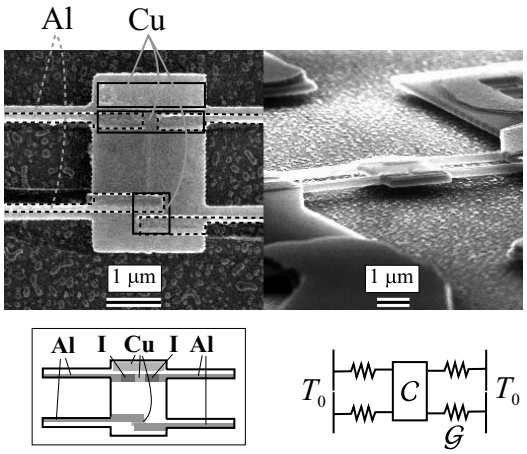

FIG. 8: Electron micrograph of a nanoscale bolometer, comprising a pair of Al-I-Cu-I-Al (SINIS) tunnel junctions fabricated on the surface of a $2 \times 3 \times 0.2$ μm^3 GaAs block, which is suspended by four $0.2 \times 0.2 \times 4$ μm^3 beams from the bulk substrate. Below is a sketch of the geometry including the tunnel junctions, and a highly simplified thermal model, indicating the heat capacitance $\mathcal{C}$ of the central block (dominated by that of the normal Cu metal), and thermal conductance $\mathcal{G}$ for each of the four beams.

A set of low temperature differential conductance curves as a function of bias voltage are shown for one of the SINIS tunnel junctions, showing the very strong temperature dependence of the zero-bias conductance, and at the lowest temperature a fairly well-defined superconducting gap $\Delta = 180$ μV per junction. In tunnel junctions with large volumes of normal metal, the gap structure is defined by large peaks in the conductance at $\pm\Delta$, which are missing here; we believe this is due to very weak electron-phonon coupling in these structures, which causes excessive heating of the normal metal electrons at non-zero bias; this question is still under investigation.

However, the zero-bias conductance is found to be well described by the conventional BCS theory for NIS tunnel junctions (see e.g. Solymar [19]). The non-equilibrium situation at non-zero bias can be phenomenologically explained using a hot-electron model, where the electrons in the normal metal are thermally decoupled from the phonons; this effect is fairly well understood in fully three dimensional phonon systems, i.e. in bulk insulating substrates, but the situation when the substrate has a strongly reduced geometry as here is less clear. Calculations indicate that for phonons in a fully three dimensional system, the effective electron-phonon thermal conductance scales as the fifth power of the electron temperature T_{el}^5, while in an effectively one-dimensional phonon system, such as applies here at the lowest temperatures, the electron-phonon conductance should scale as T_{el}^4.

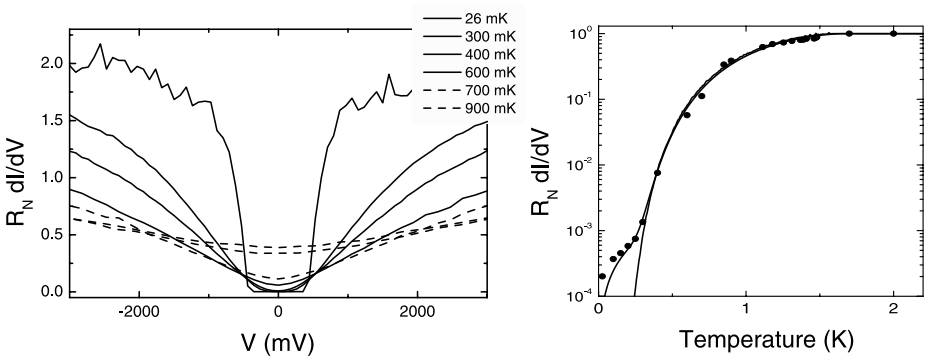

FIG. 9: (*left*) Conductance as a function of bias voltage for a suspended SINIS tunnel junction, measured at a series of temperatures from 25 mK to 900 mK. (*right*) Zero-bias conductance as a function of temperature, showing a good match to the predictions of classical BCS theory.

Measurements of the electrical readout noise of the SINIS thermistor elements yields a temperature sensitivity of 6 $\mu\mathrm{K}/\sqrt{\mathrm{Hz}}$ at an operating temperature of 100 mK; we estimate the thermal time constant τ to be 4 μsec. The corresponding estimate for the electrical noise-limited NEP is 2×10^{-18} W/Hz$^{1/2}$ at 100 mK, within about a factor of 5 of what we expect. This bolometer should be able to detect single 1 THz photons with a signal-to-noise of unity; we are presently attempting to couple signals optically to verify whether this is the case.

IV. FABRICATION TECHNIQUES

Our integrated structures are fabricated through a combination of electron-beam lithography, metal deposition, anisotropic reactive ion-beam etching, and isotropic wet etching. In Fig. 10 we display the major steps associated with a GaAs-based structure definition. We start with heterostructure substrate, comprising a bulk, semi-insulating GaAs substrate, a sacrificial AlGaAs layer 0.4 μm thick, and a top semi-insulating GaAs structural layer 0.2 μm thick. This heterostructure is grown on a bulk GaAs substrate using molecular beam epitaxy (MBE), and can be designed with different layer sequences, thicknesses, and so on.

We then begin patterning the structure. We use conventional electron beam lithography to pattern a poly-methyl methacrylate bilayer (PMMA), comprising a 495 KD molecular weight bottom layer and a 960 KD weight top layer, the PMMA dissolved in an anisole solvent. Each layer is spun on at 3 kprm for 45 seconds and baked for 10 minutes at 180°C. The pattern is exposed with a scanning electron microscope configured for lithography; the electron beam dosage is about 350 μC/cm^2, with a beam voltage of 35 kV. After exposure, we develop the pattern in a 1:3 methyl isobutyl-ketone:isopropyl alcohol (MIBK:IPA) developer, and rinse in IPA. The use of the PMMA bilayer, with a lower resolution underlayer and higher-resolution top layer, yields a undercut resist profile which gives a high-yield metal and insulator liftoff. We then thermally evaporate a layer of SrF_2 (strontium fluoride), an insulating material that has a fairly low sublimation point, lifts off well, and is partially water-soluble. The SrF_2 layer ranges from 10-100 nm in thickness, depending on subsequent steps. Following the evaporation, the unwanted SrF_2 is lifted off with the PMMA by soaking for several minutes in acetone.

The SrF_2 provides an excellent mechanical mask for the subsequent anisotropic reactive-ion etching of the GaAs and AlGaAs substrate material. We use a commercial parallel-plate reactive ion etcher, and flow pure Cl_2 gas at a pressure of 5 mtorr and a flow rate of 10 sccm. An rf power of 150 W generates a self-biased plasma

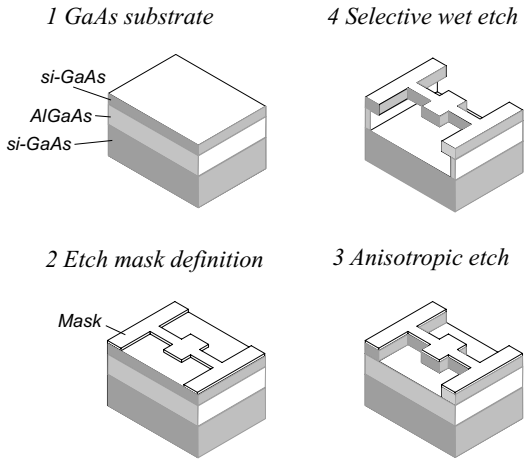

FIG. 10: Suspended heterostructure definition, starting (1) with a GaAs heterostruture substrate, (2) patterning an etch mask, (3) anisotropic etch of the GaAs and AlGaAs layers and (4) sacrificial wet etch, suspending the final structure.

voltage of about 350 V, and yields a GaAs and AlGaAs etch rate of about 0.1 μm/min. The etch is carried out to a depth corresponding to complete etching of the exposed GaAs and AlGaAs layers, typically 0.6 μm, ending on the bottom, bulk GaAs layer. The SrF_2 mask is not noticeably etched by this process, and the SrF_2 can then be removed by soaking in distilled water for 2-3 minutes.

Following this step, the exposed AlGaAs can be removed using either concentrated hydrochloric acid or a dilute (10%) solution of hydrofluoric acid; these acids do not noticeably etch GaAs, leaving the structural layer intact. The etch time varies with the size of the desired, final suspended structure. For the structure we use for the bolometer design above, etch times of order 1-2 minutes are appropriate.

The nanoscale tunnel junctions are patterned on the surface of the suspended structure. These tunnel junctions can comprise either aluminum-aluminum oxide-aluminum tunnel junctions, which below the superconducting transition temperature of Al (about 1.5 K for thin-film aluminum) forms a superconductor-insulator-superconductor (SIS) tunnel junction, or copper-aluminum oxide-aluminum tunnel junctions which are normal metal-insulator-superconductor (NIS) junctions below 1.5 K. Aluminum is an excellent material for fabrication of such structures on the deep sub-micron scale, because it forms finely-grained thin films that are fairly stable in air, and its oxide is thermally and mechanically stable, providing a high-voltage tunnel barrier for tunnel junctions. The challenge in fabricating nanoscale tunnel junctions is that the trilayer (metal-metal oxide-metal) structure must be defined in a single vacuum cycle in order to achieve high reliability structures. This can be achieved either by unpatterned, bulk trilayer deposition of the two metal films and intermediate oxide layer, which is subsequently patterned to form the tunnel junction structures, or by using a suspended resist bridge technique to pattern the films as they are deposited, and using different evaporation angles to achieve he geometric differentiation. We have followed the latter approach, which is sketched out in Fig. 11.

We spin-coat the substrate with a bottom layer of the copolymer methyl methacrylate and a top layer of 960 KD molecular weight PMMA, the first spun at 2 krpm for 45 seconds followed by a 10 minute 180°C bake, the second at 3 kprm for 45 seconds followed by the same 180°C bake. Exposure is done by electron-beam lithography at 35 kV with a 350 μC/cm^2 dosage; develop is in 1:3 MIBK:IPA with an IPA rinse. The co-polymer is extremely sensitive to the electron beam dosage, and overdevelops approximately 0.3-0.5 μm laterally beyond the edge of the exposed pattern. This significantly undercuts the top PMMA layer and allows us to use the directional nature of thermal evaporation to define the tunnel junctions, as shown in Fig. 11.

Once the suspended bridge pattern has been defined, we fabricate the tunnel junction by placing the structure in a thermal evaporator, and pumping the chamber out to a few times 10^{-7} torr. The substrate is then tilted by an angle of 20-25◦ with respect to the line of sight to the evaporation crucible, and a thin film (30-100 nm) of Al is evaporated from a W crucible. The Al film is then oxidized by admitting a small pressure (∼10 mtorr) of pure oxygen to the chamber, and waiting from 10-100 seconds to achieve the correct oxide thickness. The substrate is then tilted to $-20°$ to $-25°$ with respect to the line of sight, and a second metal film (either aluminum for an SIS tunnel junction, or copper for a NIS tunnel junction) is evaporated. The completed structure is then

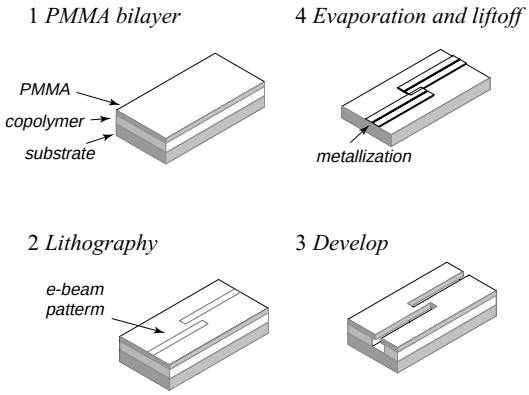

FIG. 11: Fabrication sequence for angled metal tunnel junctions; in step (1), a bilayer resist is spun and baked on the substrate, in (2) the electron beam lithography pattern is written, in (3) the pattern developed out, and in (4) metal evaporations are carried out at two angles, defining the tunnel junction in the center of the pattern.

removed from the evaporator and liftoff completed in acetone. Tunnel junction areas can range from 0.01-0.3 μm^2, depending on the particular pattern and the tilt angles, and tunnel junction resistances range from 100 Ω to 10 MΩ, depending on the junction area and oxidation time. Areas are highly repeatable, and junction resistances tend to reproduce to within a factor of two, other factors being the same.

We are also pursuing a quite different, parallel approach to integrated electromechanical devices. This approach uses GaAs substrates that include a buried two-dimensional electron gas in the top structural layer; the two-dimensional electron gas can be contacted through diffused ohmic contacts to measure transport characteristics, and can be gated using lithographically patterned electrostatic top gates that allow the lateral definition of the electron gas in the two-dimensional sheet. This approach has been used to define single quantum dots in the electron gas as well as double quantum dots, the latter allowing extremely sensitive spectroscopic probing of the electrons' electrical environment (see e.g. [20]). We have been pursuing the development of such structures to allow probing of the vibrational environment, by embedding a double quantum dot structure in a mechanically suspended structure. An example of the types of structures we are fabricating is shown in Fig. 12.

The authors acknowledge the support provided by a NASA Explorer Award No. ECS-9980734, the Army Research Office under Contract No. DAAD-19-99-1-0226, the National Science Foundation under the XYZ-On-A-Chip program, and by a Research Corporation Research Innovation Award.

[1] A.N. Cleland and M.L. Roukes. Fabrication of high frequency nanometer scale mechanical resonators from bulk Si crystals. *Appl. Phys. Lett.*, 69:2653–2656, 1996.
[2] A.N. Cleland, M. Pophristic, and I. Ferguson. Single-crystal aluminum nitride nanomechanical resonators. *Applied Physics Letters*, in press, 2001.
[3] K. Wang, A.C. Wong, and C.T. Nguyen. VHF free-free beam high-Q micromechanical resonators. *J. Microelectromechanical Systems*, 9:347–360, 2000.
[4] A.N. Cleland and M.L. Roukes. Noise processes in nanomechanical resonators. *submitted to Phys. Rev. B*, 2001.
[5] A.N. Cleland and M.L. Roukes. Nanometer scale mechanical electrometry. *Nature*, 320:160–161, 1998.
[6] R. Schoelkopf, P. Wahlgren, A.A. Kozhevnikov, P. Delsing, and D.E. Prober. The radio-frequency single-electron transistor (rf-set): A fast and ultrasensitive electrometer. *Science*, 280:1238–1242, 1998.
[7] M.P. Blencowe and M.N. Wybourne. Sensitivity of a micromechanical displacement detector based on the radio-frequency single electron transistor. *App. Phys. Lett.*, 77:3845–3847, 2000.
[8] K. Schwab. Quantum measurement with nanomechanical systems. *Proceedings of the International Conference on Quantum Computation, Sydney, Australia*, 2001.
[9] M. Devoret and R. Schoelkopf. Amplifying quantum signals with the single-electron transistor. *Nature*, 406:1039–1046, 2000.
[10] D.E. Angelescu, M.C. Cross, and M.L. Roukes. *Superlattices and Microstruct.*, 23:673, 1998.
[11] L.G.C. Rego and G. Kirczenow. Quantized thermal conductance of dielectric quantum wires. *Phys. Rev. Lett.*,

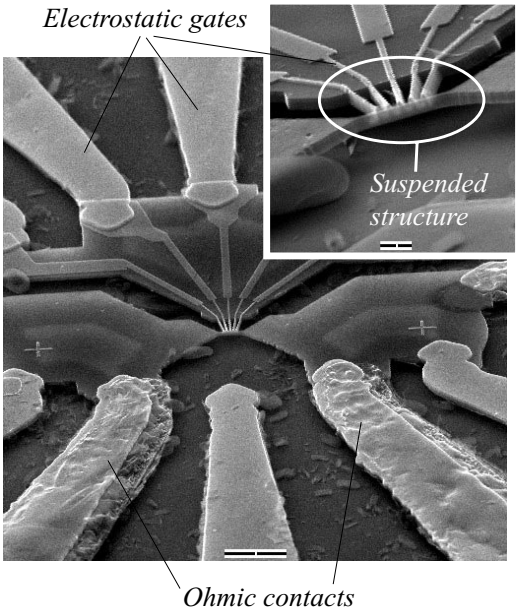

FIG. 12: GaAs structure including an embedded two-dimensional electron gas. Drain-source leads and electrostatic gates are shown in the large scale picture, and the inset shows a higher- magnification view of the suspended structure with integrated gates.

81:232–235, 1998.

[12] M.P. Blencowe. Quantum energy flow in mesoscopic dielectric structures. *Phys. Rev. B*, 59:4992–4998, 1999.

[13] D.H. Santamore and M.C. Cross. Effect of surface roughness on the universal thermal conductance. *Phys. Rev. B*, 63:184306, 2001.

[14] K. Schwab, E.A. Henriksen, J.M. Worlock, and M.L. Roukes. Measurement of the quantum of thermal conductance. *Nature*, 404:974–977, 2000.

[15] A.N. Cleland, D.R. Schmidt, and C.S. Yung. Thermal conductance of nanostructured phononic crystals. *to be published in Phys. Rev. B*, 2001.

[16] P.M. Downey, A.D. Jeffries, and S.S. Meyer et al. *Appl. Opt.*, 23:910, 1984.

[17] J.W. Zhou, K. Farooqui, P.T. Timbie, G.W. Wilson, C.A. Allen, S.H. Moseley, and D.B. Mott. Fabrication of submicron high-aspect ratio GaAs resonators. *Proc. 1995 IEEE MTT-S Intl. Microwave Symp. (Orlando FL)*, pages 1347–1350, 1995.

[18] P.D. Mauskopf, J.J. Bock, H. Del Castillo, W.L. Holzapfel, and A.E. Lange. *Appl. Opt.*, 36:765, 1997.

[19] L. Solymar. *Superconductive Tunnelling and Applications*. Wiley-Interscience, New York, 1972.

[20] T.H. Oosterkamp, L.P. Kouwenhoven, A.E.A. Koolen, N.C. van der Vaart, and C.J.P.M. Harmans. Photon sidebands of the ground state and first excited state of a quantum dot. *Phys. Rev. Lett.*, 78:1536, 1997.

Direct temporal measurement of hot-electron relaxation in a phonon-cooled metal island

D. R. Schmidt, C. S. Yung, and A. N. Cleland*
Department of Physics and iQUEST, University of California at Santa Barbara, Santa Barbara, CA 93106
(Dated: April 24, 2003)

We report temporal measurements of the electronic temperature and the electron-phonon thermal relaxation rate in a micron-scale metal island, with a heat capacity of order 1 fJ/K ($C \sim 10^7\ k_B$) . We employed a superconductor-insulator-normal metal tunnel junction, embedded in a radio-frequency resonator, as a fast ($\sim$ 20 MHz) thermometer. A resistive heater coupled to the island allowed us to drive the electronic temperature well above the phonon temperature. Using this device, we have directly measured the thermal relaxation of the hot electron population, with a measured rate consistent with the theory for dynamic electron-phonon cooling.

PACS numbers: 65.90.+i, 63.20.Kr, 65.40.Ba

Measurement of the heat capacity C of a thermodynamic system, in contact with a thermal reservoir through a thermal conductance G, necessitates the measurement of temperature over time scales shorter than the characteristic thermal relaxation time $\tau = C/G$. For mesoscopic devices, this time scale becomes exceedingly short, as both the electron and phonon heat capacities scale with device volume V. Furthermore, it is difficult to thermally isolate a phonon system from its environment, as even a very weak mechanical suspension is limited at low temperatures by the scale-independent quantum of phonon thermal conductance [1–4]. Electrons in a metal however naturally decouple from their phonon environment at low temperatures, with an electron-phonon thermal conductance $G_{e-p} \propto VT^4$. As the electron heat capacity scales as $C_e \propto VT$, the electron-phonon thermal relaxation time $\tau_{e-p} = C_e/G_{e-p}$ is independent of volume, and scales as T^{-3}. At 1 K, τ_{e-p} is of order 10 nanoseconds, a time scale that is accessible using a radio-frequency superconductor-insulator-normal metal (rf-SIN) tunnel junction thermometer [5].

In this letter, we present large-bandwidth measurements of the electronic temperature of a micron-scale metal island. Our measurement has ample bandwidth with which to directly measure τ_{e-p} at temperatures up to 1 K. This system therefore allows us to probe the thermodynamic behavior of electrons in very small metal volumes, potentially with heat capacities as small as $10\ k_B$. Such small metal volumes are prime candidates for energy absorbers in far-infrared photon-counting bolometers [3], and would allow unprecedented calorimetric sensitivity in the mesoscopic regime. Measurements over time scales shorter than τ_{e-p} are also critical for developing a complete understanding of the thermodynamics of mesoscopic systems.

The thermal decoupling of electrons and phonons at low temperatures was first described theoretically by Little [6], with a more general discussion provided by Gantmakher [7]. For a bulk metal with volume V, the power flow P_{e-p} from the electron gas at temperature T_e to the phonon gas at T_p is given by

$$P_{e-p} = \Sigma V(T_e^n - T_p^n), \tag{1}$$

where Σ is a material-dependent parameter. For a spherical Fermi surface and a Debye phonon gas, $n = 5$.

A number of researchers have verified that Eq. (1) applies to the static heating of thin-film metals, albeit with n slightly lower than 5 (fit values for n fall in the range from 4.5 to 4.9, with values for Σ in the range $1 - 2 \times 10^9$ W/m^3-K^5 [8, 9]). These measurements were made using a dc superconducting quantum interference device (dc-SQUID) to measure the Johnson-Nyquist noise in the metal film, and thus extract the electronic temperature.

A second approach to measuring the electron temperature in thin metal films was presented by Nahum *et al.* [10]: using a SIN tunnel junction as an electronic thermometer. These authors suggested that such a structure could form the heart of a bolometric detector. Measurements of the static energy distribution of electrons in a normal metal under voltage bias were made by Pothier *et al.* using a similar SIN-based thermometer [11]. Yung *et al.* [3] also demonstrated a SIN thermometer in contact with a normal metal island, the whole fabricated on a micron-scale suspended GaAs substrate.

Here we study the *dynamic* temperature response of a small metal island using a SIN tunnel junction thermometer. Well below the superconducting transition temperature T_C, the tunnel junction's small-signal resistance at zero bias, $R_0 \equiv dV/dI(0)$, is exponentially dependent on the ratio of temperature T to the superconducting energy gap Δ, $R_0 \propto e^{\Delta/k_B T}$. A sub-micron scale SIN tunnel junction therefore has a low-temperature resistance that can easily exceed $10^6\ \Omega$, limiting conventional time-domain measurements to bandwidths of order 1 kHz. In order to monitor changes in this resistance at sub-microsecond time scales, we circumvent the unavoidable stray capacitance in the measurement circuit by embedding the junction in a LC resonant circuit, as shown in Fig. 1 [12]. We then measure the resistance of the SIN junction, and thus the normal metal electron temperature, by measuring the power reflected from the circuit at the LC resonance frequency. A change of the junction resistance R_0, induced by heating the electrons, in turn changes the amplitude of the reflected radio frequency signal. In this technique, the stray cable capacitance C is in resonance with the inductor L, the resonator also serving to impedance-match the resistance of the tunnel junction to the measurement system. This readout scheme is analogous to that employed in the radio-frequency

single electron transistor (rf-SET) [13].

Our device is fabricated on a 4×4×0.5 mm^3 single-crystal GaAs chip using four lithography steps. A 85 nm thick Au center island and wire-bond pads were first deposited on the GaAs substrate; an intermediate Au pad was also deposited in this layer. We then deposited a 100 nm thick NiCr film, designed to have a 50 Ω resistance, matching the characteristic cable impedance Z_0. The ground leads and heater contact were evaporated in the third layer, using superconducting Al to ensure thermal isolation below 1 K [14]. The NiCr contacts the Al *via* the intermediate Au pad, to ensure low interfacial resistivity. The tunnel junction thermometer was deposited in the fourth lithography step. We used a standard suspended resist bridge, double-angle evaporation method to define the tunnel junction [15]: A 90 nm thick Al electrode was evaporated, and the Al then oxidized in 200 mTorr of pure O_2 for 90 s. The junction was completed by evaporating a 90 nm thick Cu counterelectrode, which also contacted the center Au island.

The device is shown in Fig. 1(a). Note that the Au center island is electrically grounded, so that heating signals applied to the NiCr resistor do not couple directly to the SIN junction, but instead affect it by changing the temperature of the Au island. The heating signals are in principle therefore limited by diffusion time from the NiCr through the Au island and then along the Cu electrode to the SIN tunnel junction; we estimate this time to be less than 10 ns.

We mounted the chip containing the device on a printed circuit board, which was enclosed in a brass box. Gold wire bonds (25 μm diameter) were made between the Au bond pads on the chip and Cu coplanar striplines on the circuit board. A chip inductor with $L = 390$ nH was placed in series with the SIN junction. The resonance capacitance C was from the geometric capacitance of the stripline and Au bond pads, with $C = 0.5$ pF. The expected LC resonance frequency is $f_{res} = 1/2\pi(LC)^{1/2} \cong 350$ MHz, the tuned circuit quality factor is $Q = \sqrt{L/CZ_0^2} \cong 20$, and the measurement bandwidth is $\Delta f = f_{res}/Q \cong 20$ MHz. The measurement circuit is shown in Fig. 1(b). The tunnel junction is configured for simultaneous dc and rf measurements *via* a bias tee, not shown in Fig. 1.

We have described the technical aspects of rf-SIN thermometry elsewhere [5]. Here we will describe the salient aspects as they pertain to these measurements. We determined the resonance frequency of the LC circuit to be 345 MHz. A carrier signal source was connected through a directional coupler to a coaxial line, which was in turn connected to the LC resonant circuit. The carrier frequency was set close to the LC resonant frequency [16]. The signal reflected from the LC resonator was high-pass filtered and amplified using a low-noise amplifier. This amplified signal was then mixed with a local oscillator (lo), provided by a second rf signal source phase-locked to the carrier source. The intermediate frequency (if) output from the mixer was low-pass filtered, amplified, and the resulting time-dependent signal captured by a sampling oscilloscope. The NiCr resistor was heated using either a dc or an rf pulsed source: A pulse sent to the resistor heats the NiCr, the Au island and the Cu electrode, changing the electron temperature, and therefore changing the amplitude of the carrier signal reflected from the tuned LC circuit, as shown in Fig. 1(d).

In order to characterize the response of the system, we first heated the NiCr resistor using a $f_0 = 25$ kHz sinusoidal drive signal. Figure 2 shows the response for various drive powers. The if signal was low-pass filtered ($f < 2$ MHz), and each curve is the result of averaging 256 drive periods. The left axis is the mixer if voltage, and the labels on the right axis indicate the electron temperature inferred from the change in reflected signal. The instantaneous power dissipated in the resistor is proportional to the square of the voltage applied the heater ($P(t) = V^2(t)/R_{NiCr}$); this causes the reflected signal to be modulated at twice the heater signal, $2f_0 = 50$ kHz. At low powers P, contributions at 25 kHz were also present, due to a small dc offset on the heater voltage $V(t)$, $V(t) = V_{dc} + V_0 \sin 2\pi f_0 t$. At the highest powers, the reflected signal is clipped near the Al superconducting transition temperature: The junction resistance is temperature-independent above T_C.

The measured signal depends on the proper adjustment of the detection mixer's local oscillator (lo) phase. In order to correctly adjust this phase, we first applied a heater signal sufficient to get a clipped response. The phase of the lo was then adjusted to achieve maximum differential response between the lowest (≅ 300 mK) and highest (≅ 1400 mK) electron temperatures. The SIN junction ranges from 105 kΩ to 6 kΩ over this temperature range, and passes through the value of R_0 where optimal matching with the cable impedance occurs [17]. In the parlance of radio-frequency electronics, the carrier signal is over-modulated, so the absolute value of the reflected power is a non-monotonic function of temperature. However, as we are sensitive to the phase of the carrier, the proper quadrature of the mixer if voltage does have a monotonic response. Finally, the reflected if signal as a function of cryostat temperature, for no heater voltage applied, was used to construct the temperature calibration, $V_{if}(T)$.

We measured the *quasi-static* relation between the electron-phonon power flow P_{e-p} and the electron and phonon temperatures, T_e and T_p, as given by Eq. (1). We applied a series of 3 μs pulses while varying the peak heating power, and monitored the resulting time-dependent electron temperature. The substrate temperature was kept at 300 mK. The signal was filtered with a 2 MHz low-pass filter, and the result of 256 averages is shown in Fig. 2. This is equivalent to a dc heating measurement with a key difference, namely that as the heating pulses were delivered to the device at a 1 kHz repetition rate, the duty cycle was only 0.3%, so that the substrate phonons did not have sufficient time to heat. The equivalent measurement in a dc heating experiment requires 300 times as much power, with significant phonon heating a likely outcome. We find a fit relation matching that of Eq. (1), with n = 4.7 and Σ = 2.1×10^9 W/m^3-K$^{4.7}$, in good agreement with previously measured values [3, 8, 9].

We finally performed measurements of *dynamic* electron-

phonon cooling, by monitoring the detailed time-dependent behavior of the electron temperature at the end of a heating pulse. Figure 3 shows the measured response to a heater pulse (2560 averages, using a 50 MHz low-pass filter). The heating voltage pulse was configured to have 1.6 ns leading and trailing edge widths. The initial temperature rise is at least as fast as the time resolution of the measurement, with an expected rate $\dot{T} = P/C_e \cong 140$ mK/nsec, as we are directly heating the electron population. The rapid onset also indicates that electron diffusion in the composite metal structure is not a rate-limiting factor. At the end of the pulse, the heating power drops to zero, leaving a non-equilibrium hot electron population that relaxes by phonon emission. Initially this relaxation is seen to be quite rapid, but it slows markedly as the electron temperature nears the phonon temperature.

The shape of the relaxation curve shown in Fig. 4 can be understood by examining the dynamics of the electron temperature. The electron heat capacity is $C_e = \gamma V T_e$, where γ is the Sommerfeld constant. The power flow to the phonons is given by Eq. (1). The time rate of change of the electron temperature $\dot{T}_e$ is then

$$\dot{T}_e = -\frac{\Sigma}{\gamma}(T_e^{n-1} - \frac{T_p^n}{T_e}). \tag{2}$$

Using the normalized temperature $\theta \equiv T_e/T_p$, this is

$$\dot{\theta} = -\frac{1}{n}\frac{1}{\tau_{e-p}(T_p)}(\theta^{n-1} - 1/\theta), \tag{3}$$

in terms of the small signal thermal relaxation rate $\tau_{e-p}^{-1} = n\Sigma T_p^{n-2}/\gamma$ for electrons near the phonon temperature [18]. We fit our measured response to Eq. (3) using this rate as the only adjustable parameter, finding the value $\tau_{e-p} = 1.6\ \mu$s [19]. This is in agreement with the measured value of Σ, and a composite γ which takes into account the relative metal volumes in the device. We can thus determine the the heat capacity of the metal island, $C_e \sim 1$ fJ/K $\cong 10^7\ k_B$ at 300 mK.

There are some extremely interesting opportunities for electronic calorimetry in this temperature and size regime. Intriguing theoretical results have been presented for the thermodynamic response of mesoscopic superconducting disks [20], and giant moment electronic paramagnets such as PdMn [21] and PdFe [22] offer a means of probing the thermodynamics of a mesoscopic phonon-electron-spin-coupled system.

We are far from the ultimate calorimetric limits for this technique. Devices with active metal volumes that are smaller by a factor of $10^4 - 10^5$ can be fabricated, yielding a total heat capacity of order $\sim 10 - 100\ k_B$ at 30 mK. Changes in the heat capacity of less than 10% are easily detected, yielding a sensitivity of order 1 k_B, i.e. that associated with a single degree of freedom.

In summary, we have performed sub-μs timescale measurements of the electron temperature of a micron scale metal island, cooled dynamically by phonon emission. The ability to apply and measure the response to fast heat pulses has permitted us to directly measure the electron-phonon thermal relaxation, and thus extract the heat capacity of the metal island. This, to our knowledge, is the smallest measured heat capacity to date. The device that we have fabricated is a major step forward for mesoscopic thermodynamics, provides a platform for sub-aJ/K calorimetry, and can potentially play an important role in future single photon and phonon bolometers.

We acknowledge financial support provided by the NASA Office of Space Science under grants NAG5-8669 and NAG5-11426, the Army Research Office under Award DAAD-19-99-1-0226, and the Center for Nanoscience Innovation for Defense. We thank Bob Hill for processing support.

* cleland@physics.ucsb.edu

[1] L. G. C. Rego and G. Kirczenow, Phys. Rev. Lett. **81**, 232 (1998).
[2] K. Schwab, E. A. Henriksen, J. M. Worlock, and M. L. Roukes, Nature **404**, 974 (2000).
[3] C. S. Yung, D. R. Schmidt, and A. N. Cleland, Appl. Phys. Lett. **81**, 31 (2002).
[4] A. N. Cleland, D. R. Schmidt, and C. S. Yung, Phys. Rev. B **64**, 172301 (2001).
[5] D. R. Schmidt and C. S. Yung and A. N. Cleland, submitted to Appl. Phys. Lett.
[6] W. A. Little, Can. J. Phys. **37**, 334 (1959).
[7] V. F. Gantmakher, Rep. Prog. Phys. **37**, 317 (1974).
[8] M. L. Roukes, M. R. Freeman, R. S. Germain, R. C. Richardson, and M. B. Ketchen, Phys. Rev. Lett. **55**, 422 (1985).
[9] F. C. Wellstood, C. Urbina, and J. Clarke, Phys. Rev. B **49**, 5942 (1994).
[10] M. Nahum and J. M. Martinis, Appl. Phys. Lett. **63**, 3075 (1993).
[11] H. Pothier, S. Guéron, N. O. Birge, D. Esteve, and M. H. Devoret, Phys. Rev. Lett. **79**, 3490 (1997).
[12] The intrinsic electrical bandwidth of a tunnel junction is set by the product of the tunnel resistance R_0 and the junction capacitance C_J, $f_{3\ \mathrm{dB}} = 1/2\pi R_0 C_J$. For a fixed tunnel barrier thickness, this product is independent of the junction area A. With typical values of $R_0 A \sim 10^3\ \Omega - \mu\mathrm{m}^2$ and $C_J/A \sim 10^{-13}$ F/μm^2, this corresponds to $f_{3\ \mathrm{dB}} \sim 2$ GHz.
[13] R. J. Schoelkopf, P. Wahlgren, A. A. Kozhevniv, P. Delsing, and D. E. Prober, Science **280**, 1238 (1998).
[14] The thermal conductivity of superconducting Al is exponentially supressed below T_C.
[15] T. A. Fulton and G. J. Dolan, Phys. Rev. Lett. **59**, 109 (1987).
[16] Typically -100 dB (100 fW), the rf-SET of Ref [13] can tolerate much higher power than the rf-SIN.
[17] The calculated value is at $R_0 = L/CZ_0 \sim 11\ \mathrm{k}\Omega$.
[18] To recover the small signal response for $n = 5$, rewrite Eq. (2) in terms of the reduced temperature $\epsilon \equiv (T_e - T_p)/T_p = \theta - 1$ and retain terms $O(\epsilon)$, $\dot{\epsilon} = 5(\Sigma/\gamma)T_p^{n-2}\epsilon$.
[19] For simplicity, we used $n = 5$ for the fit.
[20] P. S. Deo, J. P. Pekola, and M. Manninen, Europhys. Lett. **50**, 649 (2000).
[21] G. J. Nieuwenhuys, Adv. Phys. **24**, 515 (1975).
[22] R. P. Peters, C. Buchal, M. Kubota, R. M. Mueller, and F. Pobell, Rev. Rev. Lett. **53**, 1108 (1984).

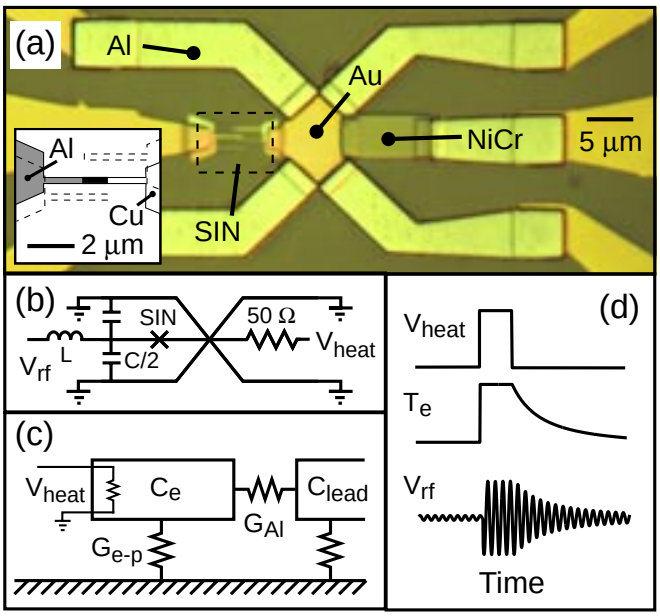

FIG. 1: (Color Online)(a) Optical micrograph of the electron calorimeter. The center Au island is contacted on the left by a rf-SIN thermometer, and on the right by a NiCr resistor. The outer ground leads and the contact right of the resistor are superconducting Al. *inset*: Detail drawing of the SIN junction, Al shown in gray, Cu in white, and overlap junction area in black. The dotted outlines are fabrication artifacts. (b) Electrical circuit. The SIN thermometer is embedded in an LC resonator formed by a discrete inductor and the stray lead capacitance. The junction resistance is monitored using the power reflected from the LC resonator at its resonance frequency. (c) Thermal schematic. The calorimeter electron gas C_e is thermally isolated by the superconducting Al contacts (G_{Al}); the dominant thermal link is thus through the substrate phonons (G_{e-p}). The NiCr resistor directly heats the electron gas. (d) Timing diagram. The voltage pulse applied to the heater causes the temperature to rise, saturate, and then decay. The envelope of the reflected power from the LC resonator is directly related to the temperature.

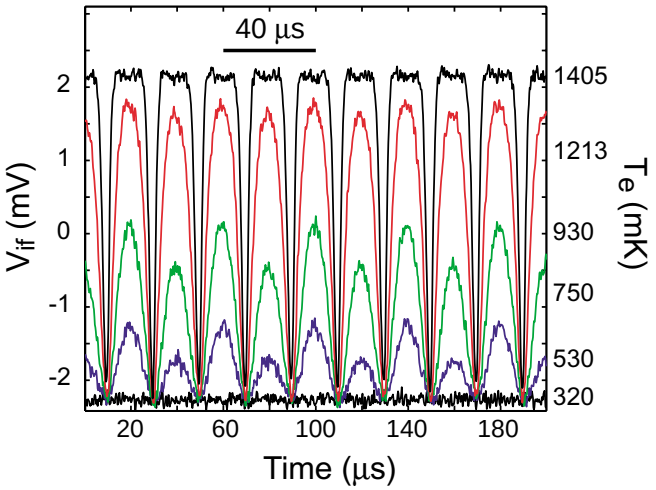

FIG. 2: (Color Online) Response to a 25 kHz heater drive (*left axis*: Mixer if voltage, *right axis*: Electronic temperature). The thermometer response is at 50 kHz as discussed in the text. Each trace is the result of 256 averages with a 2 MHz low-pass filter. The baseline signal is for zero heater power, with power ranging from 300 pW to 100 nW. At the highest power the signal clips at $T = T_C \approx 1400$ mK. The 25 kHz components at low power are due to a dc offset in the heater signal.

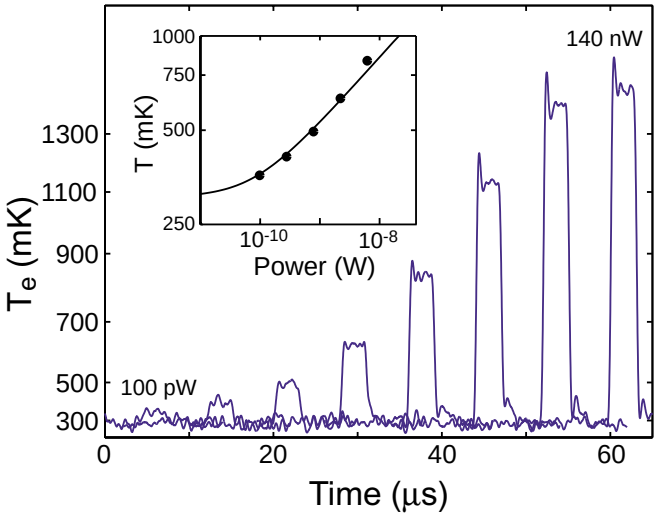

FIG. 3: Composite response to pulsed heating signals, with pulses 3.0 μs long with peak power 0.1, 0.3, 0.8, 2.2, 6.2, 17.6, 49.0, and 140 nW. The resulting electronic temperature for each pulse is used to determine the relation $P(T_e, T_p)$. *Inset:* The solid line is a fit to $P(T_e, T_p) = V\Sigma(T_e^n - T_p^n)$, with $T_p = 300$ mK, $n = 4.7$, $V = 10$ μm^3, and $\Sigma = 2.1\times10^9$ W/m^3-K$^{4.7}$.

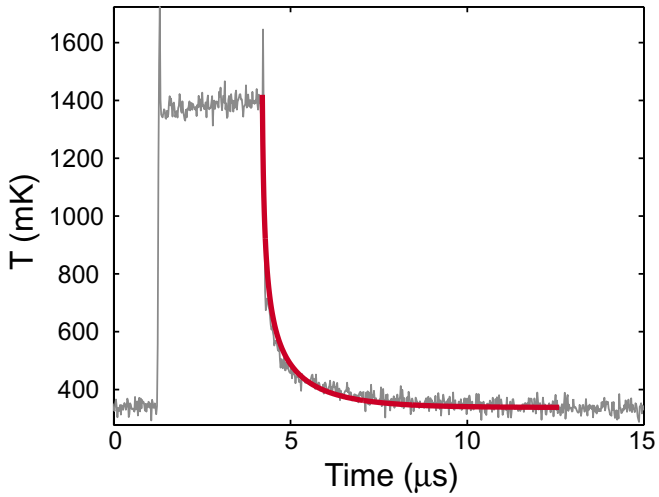

FIG. 4: (Color Online) Response to a 3.0 μs pulse with peak power 140 nW applied to the heater. The electronic temperature quickly rises to $\approx$ 1400 mK at the start of the pulse. The trailing edge of the response decays with a temperature-dependent relaxation time. The solid line is a fit to the thermal model discussed in the text. The ringing is due to the if amplifier circuit.

Superconducting qubit storage and entanglement with nanomechanical resonators

A. N. Cleland[1] and M. R. Geller[2]
[1] *Department of Physics, University of California, Santa Barbara, California 93106*
[2] *Department of Physics and Astronomy, University of Georgia, Athens, Georgia 30602-2451*
(Dated: August 19, 2003)

We describe a quantum-information-processing architecture based on the integration of ultrahigh-frequency nanomechanical resonators with Josephson-junction-based qubit circuits, which can be used to implement the single- and multi-qubit operations critical to quantum computation. The qubits are eigenstates of large-area, current-biased Josephson junctions, manipulated and measured using strobed external circuitry. Two or more of these "phase qubits" are coupled to a high-quality-factor piezoelectric mechanical resonator, which forms the backbone of our architecture, enabling coherent manipulation of the qubits. The integrated system is analogous to one or more few-level atoms (the Josephson junction qubits) in a tunable electromagnetic cavity (the nanomechanical resonator). Our architecture combines the best features of solid-state and cavity-QED approaches, and may make possible multi-qubit information processing in a scalable, solid-state environment.

PACS numbers: 03.67.Lx, 85.25.Cp, 85.85.+j

The lack of scalable qubit architectures, with sufficiently long quantum-coherence lifetimes and a suitably controllable entanglement scheme, remains the principal roadblock to building a large-scale quantum computer. Superconducting devices exhibit robust macroscopic quantum behavior [1]. Recently, there have been exciting demonstrations of long-lived Rabi oscillations in current-biased Josephson junctions [2, 3], subsequently combined with a two-qubit coupling scheme [4], and in parallel, demonstrations of Rabi oscillations and Ramsey fringes in a Cooper-pair box [5–7]. These accomplishments have generated significant interest in the potential for Josephson-junction-based quantum computation [8]. Coherence times τ_φ up to $5\,\mu$s have been reported in the current-biased devices [2], with corresponding quality factors $Q_\varphi \equiv \tau_\varphi\,\Delta E/h$ of the order of 10^5, yielding sufficient coherence time to perform many logical operations. Here ΔE is the qubit energy level spacing.

In this paper, we describe an architecture in which ultrahigh-frequency resonators coherently couple two or more current-biased Josephson junctions, where the superconducting "phase qubits" are formed from the energy eigenstates of the junctions. We show that the system is analogous to one or more few-level atoms (the Josephson junctions) in a tunable electromagnetic cavity (the resonator), except that here we can individually tune the energy level spacing of each atom, and control the electromagnetic interaction strength.

Other investigators have proposed the use of electromagnetic [9–16] or superconducting[17, 18] resonators to couple two or more Josephson junctions together. The use of nanomechanical resonators to mediate multi-qubit operations has not to our knowledge been described previously, although an approach to create entangled states of a single nanomechanical resonator has been proposed [19]. The use of mechanical as opposed to electromagnetic resonators has the advantage that potentially much higher quality factors can be achieved [20], with significantly smaller physical dimensions, enabling a truly scalable approach.

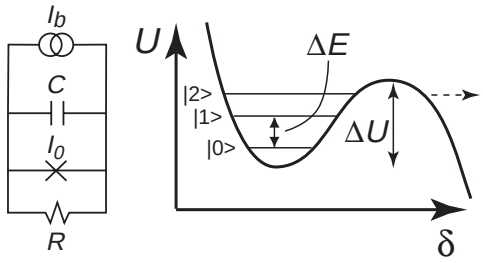

FIG. 1: *Left:* Equivalent-circuit model for a current-biased Josephson junction. A capacitance C and resistance R in parallel with an ideal Josephson element with critical current I_0, all with a bias current I_b. *Right:* Metastable potential well in the cubic potential limit, showing the barrier height ΔU that separates the metastable states from the continuum. Here there are three quasi-bound states $|0\rangle$, $|1\rangle$, and $|2\rangle$, the lower two separated in energy by ΔE.

Our implementation uses large-area current-biased Josephson junctions, with capacitance C and critical current I_0; a circuit model is shown in Fig. 1. The largest relevant energy is the Josephson energy $E_{\rm J} \equiv \hbar I_0/2e$, with a charging energy $E_{\rm c} \equiv (2e)^2/2C \ll E_{\rm J}$. The dynamics of the Josephson phase difference δ is that of a particle of mass $M = \hbar^2 C/4e^2$ moving in an effective potential $U(\delta) \equiv -E_{\rm J}(\cos\delta + s\,\delta)$, for bias current $s = I_{\rm b}/I_0$ [21, 22]. For bias currents $s < 1$, the potential $U(\delta)$ has metastable minima, separated from the continuum by a barrier $\Delta U \equiv U(\delta_{\rm max}) - U(\delta_{\rm min}) \rightarrow (4\sqrt{2}/3)E_{\rm J}(1-s)^{3/2}$ for $s \rightarrow 1^-$, as shown in Fig. 1. The curvature $U''(\delta)$ defines the small-amplitude plasma frequency $\omega_{\rm p} \equiv \sqrt{U''(\delta_{\rm min})/M} = \omega_{\rm p0}(1-s^2)^{1/4}$, with $\omega_{\rm p0} = \sqrt{2eI_0/\hbar C} = \sqrt{2E_{\rm c}E_{\rm J}}/\hbar$. The Hamiltonian for the junction phase difference is $H_{\rm J} = P^2/2M + U(\delta)$, with $P = -i\hbar d/d\delta$ the momentum operator. The junc-

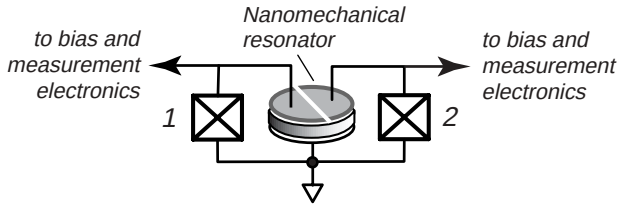

FIG. 2: Proposed architecture for achieving two-qubit entanglement with the use of a nanomechanical resonator. The qubits are the two Josephson junctions, coupled to a resonator, shown as a disc with a split gate.

tion's zero-voltage state corresponds to the phase "particle" trapped in one of the metastable minima.

The lowest two quasi-bound states in a local minimum, $|0\rangle$ and $|1\rangle$, define the phase qubit. State preparation is typically carried out with s just below unity, in the range $s = 0.95 - 0.99$, where the effective potential $U(\delta)$ is strongly anharmonic, and for which there are only a few quasibound states [3, 4]. The anharmonicity allows state preparation from a classical radiofrequency (rf) field, as then the frequency of the classical field can be set to couple to only the lowest two states. In our information processing scheme, by contrast, single quanta are exchanged between the junction and the resonator, so anharmonicity is not necessary; we find it convenient to work with s between 0.5 and 0.9.

We will focus here on coupling a single resonator to two Josephson qubits; the extension to larger numbers of resonators and junctions will be considered in later work. The architecture for the two-junction circuit is shown in Fig. 2. The disk-shaped element in the center of the figure is the nanomechanical resonator, consisting of a single-crystal piezoelectric disc sandwiched between two metal plates, and the Josephson junctions are the crossed boxes on either side of the resonator. We assume the use of high-impedance measurement and bias circuits for the junctions, such as those developed by Martinis *et al.* [3].

The phase qubit state $|0\rangle_{\rm J}$ of a single junction is prepared by waiting for any excited component to decay. The pure state $|1\rangle_{\rm J}$, or a superposition state $\alpha|0\rangle_{\rm J}+\beta|1\rangle_{\rm J}$, is prepared by adding a classical rf current $I_{\rm rf}$ to the bias, $I_{\phi 1}(t) = I_{\rm dc} + I_{\rm rf}\,\cos(\omega_{\rm rf}t)$. Both $I_{\rm dc}$ and $I_{\rm rf}$ vary slowly compared to $\hbar/\Delta E$. When $\omega_{\rm rf}$ is near resonance with the level spacing $\Delta E/\hbar$, the qubit will undergo Rabi oscillations, allowing the controlled preparation of linear combinations of $|0\rangle_{\rm J}$ and $|1\rangle_{\rm J}$.

The nanomechanical resonator is designed with a fundamental thickness resonance frequency $\omega_0/2\pi \sim 1 - 10\,{\rm GHz}$, with a quality factor $Q \sim 10^5 - 10^6$. Piezoelectric dilatational resonators with thickness resonance frequencies in this range, and quality factors of order of 10^3 at room temperature, have been fabricated from sputtered AlN [23, 24]. Single-crystal AlN can also be grown by chemical vapor deposition [25]. Our simulations are based on such a resonator, with a diameter and thickness of $1\times 0.5\ \mu m^2$ [26]. Such resonators can be used to coherently store a qubit state prepared in a current-biased Josephson junction, return it to that junction, or transfer it to another junction, as well as entangle two or more junctions. These operations are performed by tuning the energy level spacing ΔE into resonance with $\hbar\omega_0$, generating electromechanical Rabi oscillations.

Referring to Fig. 2, the total bias current of junction 1 is $I_{\rm dc1} + I_{\rm res}$, where $I_{\rm res}$ is the current through the resonator from that junction. A simple model for the resonator [27] allows us to write $I_{\rm res} = C_{\rm res}(\dot{V} + h_{33}\dot{U})$, where $C_{\rm res}$ is the resonator geometric capacitance, h_{33} the relevant piezoelectric coupling constant, $\dot{V}$ the rate of voltage change, and $\dot{U}$ the rate of change of the mechanical displacement. The current $I_{\rm res}$ is partly due to the capacitance $C_{\rm res}$ and partly due to the piezoelectrically-coupled displacement U. $C_{\rm res}$, in parallel with the junction capacitance C, renormalizes the phase mass M to $\tilde{M} = \hbar^2\tilde{C}/4e^2$, where $\tilde{C} = C + C_{\rm res}$.

With the resonator coupled to the superconducting phase through the voltage V, the Hamiltonian for the combined junction-resonator system is $H = H_{\rm J} + H_{\rm res} + \delta H$. Here $H_{\rm res} = \hbar\omega_0 a^\dagger a$ is the Hamiltonian of the isolated resonator, where we have quantized the resonator displacement field with creation (destruction) operators $a^\dagger$ (a), and only included the fundamental dilatational mode. δH is the phase-resonator interaction,

$$\delta H = -(\hbar\, C_{\rm res} h_{33}/2e)\dot{U}\,\delta = ig(a - a^\dagger)\delta, \qquad (1)$$

where the coupling constant g is

$$g = \frac{\sqrt{3}\,\hbar^{3/2}\,C_{\rm res}h_{33}\,\sqrt{\omega_0}}{2\sqrt{2}\,e\,\sqrt{\rho \mathbb{V}}}. \qquad (2)$$

For our model resonator $g \approx 0.820\ \mu$eV.

In the junction eigenstate basis, the junction Hamiltonian is $H_{\rm J} = \sum_m \epsilon_m c_m^\dagger c_m$, with creation (destruction) operators $c_m^\dagger$ (c_m) acting on the phase qubit state. The interaction Hamiltonian is

$$\delta H = ig \sum_{mm'} \langle m|\delta|m'\rangle\, c_m^\dagger c_{m'}(a - a^\dagger). \qquad (3)$$

The eigenstates of the noninteracting Hamiltonian $H_0 = H_{\rm J} + H_{\rm res}$ are $|mn\rangle \equiv |m\rangle_{\rm J} \otimes |n\rangle_{\rm res}$, with energies $E_{mn} = \epsilon_m + \hbar\omega_0\, n$, where n is the resonator occupation number. An arbitrary state can be expanded as $|\Psi(t)\rangle = \sum_{mn} c_{mn}(t)|mn\rangle \exp(-iE_{mn}t/\hbar)$ with amplitudes $c_{mn}(t)$.

The full Hamiltonian is equivalent to that of a few-level atom in an electromagnetic cavity. The cavity "photons" here are phonons, which interact with the "atoms" (here the Josephson junctions) via the piezoelectric effect. This analogy will allow us to adapt quantum-information processing protocols developed for cavity-QED to our solid-state architecture.

We first show that we can coherently transfer a qubit state from a junction to a resonator, using the adiabatic approximation combined with the rotating-wave approximation (RWA) of quantum optics [28]. We assume that the bias current s changes slowly on the time scale $\hbar/\Delta E$, and work at temperature $T = 0$. The RWA is valid when ΔE and $\hbar\omega_0$ are close on the scale of $\hbar\omega_0/Q_{\rm res}$, and when the interaction strength $g \ll \Delta E$. At time $t = 0$, we prepare the resonator in the state $|0\rangle_{\rm res}$. In the RWA, neglecting relaxation, we obtain the amplitude evolution

$$\begin{aligned} i\hbar\,\partial_t c_{0n} &= -ig\,\sqrt{n}\,\langle 0|\delta|1\rangle\, e^{i\omega_{\rm d}t}\, c_{1,n-1} \\ i\hbar\,\partial_t c_{1n} &= ig\,\sqrt{n+1}\,\langle 1|\delta|0\rangle\, e^{-i\omega_{\rm d}t}\, c_{0,n+1}, \end{aligned} \qquad (4)$$

where $\omega_{\rm d} \equiv \omega_0 - \Delta E/\hbar$ is the resonator–qubit detuning. We integrate to find the reduced density matrices $\rho_{\rm J}(t)$ (in the qubit subspace) and $\rho_{\rm res}(t)$ (in the zero- and one-phonon resonator subspace). The junction phase is initially prepared in the pure state $\alpha|0\rangle_{\rm J} + \beta|1\rangle_{\rm J}$, corresponding to the reduced density matrix

$$\rho_{\rm J}(0) = \begin{bmatrix} |\alpha|^2 & \alpha\beta^* \\ \alpha^*\beta & |\beta|^2 \end{bmatrix}. \qquad (5)$$

We allow the junction and resonator to interact for a time $\Delta t = \pi/\Omega_d$, where the Rabi frequency is $\Omega_d = (\Omega_0^2 + \omega_{\rm d}^2)^{1/2}$, in terms of the tuned (resonant) value $\Omega_0 = 2g|\langle 0|\delta|1\rangle|/\hbar$. After the interaction interval Δt, the *resonator* is then found to be in the same pure state,

$$\rho_{\rm res}(\pi/\Omega_d) = \begin{bmatrix} |\alpha|^2 & -\alpha\beta^* e^{i\pi\omega_0/\Omega_d} \\ -\alpha^*\beta\, e^{-i\pi\omega_0/\Omega_d} & |\beta|^2 \end{bmatrix}, \qquad (6)$$

apart from expected phase factors. The phase qubit state has been swapped with that of the resonator. The cavity-QED analog of this operation has been demonstrated experimentally in Ref. [29].

To assess the limitations of the RWA, we have simulated this process by numerically integrating the exact amplitude equations

$$i\hbar\,\dot{c}_{mn} = \sum_{m'n'} \langle mn|\delta H|m'n'\rangle e^{i(E_{mn}-E_{m'n'})t/\hbar}\, c_{m'n'}. \qquad (7)$$

The Josephson junction had parameters corresponding Ref. [3], $E_{\rm J} = 43.05\,$meV and $E_{\rm c} = 53.33\,$neV. We used a 4th-order Runge-Kutta method with a time step of 10 fs. Our main result is shown in Fig. 3. The qubit transfer depends sensitively on the *shape* of the profile $s(t)$, which starts at $s = 0.50$, and is then adiabatically changed to the resonant value $s = 0.928$. We find that the time during which s changes should be at least exponentially localized. This can be understood by recalling that the RWA requires the qubit to be exactly in resonance with the resonator (in the $Q \to \infty$ limit). Therefore one must bring the system into resonance as quickly as possible without violating adiabaticity. The power-law tails associated with an arctangent function, for example, lead to deviations from the desired behavior, shown in Fig. 3(b). The result in Fig. 3(a) was obtained using Gaussian profiles with a cross-over time of 1 ns. All quasibound states were included in the calculation, and convergence with the resonator's Hilbert space dimension was obtained. The junction is held in resonance for half a Rabi period π/Ω_d, during which energy is exchanged at the Rabi frequency. The systems are then brought out of resonance. The final state amplitudes are given in Table I, and are quite close to the RWA results.

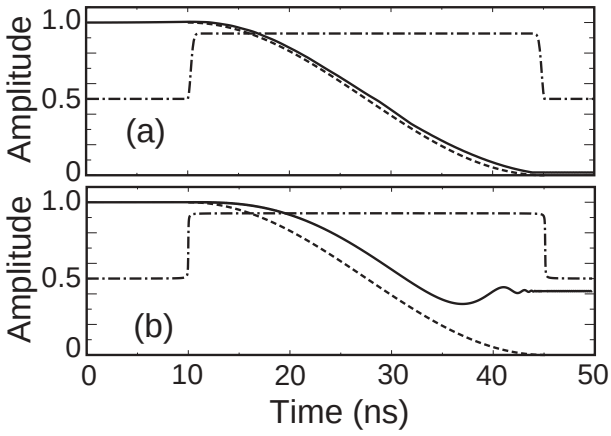

FIG. 3: (a) Phase qubit storage. Solid curve is $|c_{10}(t)|^2$, dashed curve is analytic RWA calculation, dash-dotted curve is $s(t)$. (b) Qubit storage with arctangent bias-current profile. All other parameters are the same as in (a). Solid curve is numerical result for $|c_{10}(t)|^2$.

TABLE I: Final state amplitudes $c_{mn}(\pi/\Omega_{\rm d})$ for phase-qubit coupled to nanomechanical resonator.

probability amplitude	$\mathrm{Re}\, c_{mn}$	$\mathrm{Im}\, c_{mn}$	$\lvert c_{mn}\rvert^2$
c_{00}	−0.009	−0.006	0.000
c_{01}	−0.252	−0.972	1.007
c_{10}	0.018	0.090	0.008
c_{11}	−0.010	0.003	0.000

To pass a qubit state $\alpha|0\rangle + \beta|1\rangle$ from junction 1 to junction 2, the state is loaded into the first junction and the bias current changed to bring the junction into resonance with the resonator for half a Rabi period. This writes the state $\alpha|0\rangle + \beta|1\rangle$ into the resonator. After the first junction is taken out of resonance, the second junction is brought into resonance for half a Rabi period, passing the state to the second junction. We have simulated this operation numerically, assuming two identical junctions coupled to the resonator described above. The results are shown in Fig. 4 and Table I, where $c_{m_1m_2n}$ is the probability amplitude (in the interaction representation) to find the system in the state $|m_1m_2n\rangle$, with m_1 and m_2 labelling the states of the two junctions.

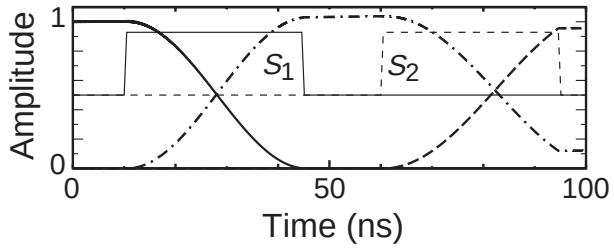

FIG. 4: Qubit transfer between two junctions. Solid curve is $|c_{100}(t)|^2$, dashed-dotted curve is $|c_{001}(t)|^2$, dashed curve is $|c_{010}(t)|^2$. Thin solid and dotted curves show $s_1(t)$ and $s_2(t)$.

TABLE II: Final amplitudes $c_{m_1m_2n}$ for state transfer.

probability amplitude	$\mathrm{Re}\, c_{m_1m_2n}$	$\mathrm{Im}\, c_{m_1m_2n}$	$\lvert c_{m_1m_2n}\rvert^2$
c_{100}	0.038	−0.013	0.002
c_{001}	−0.314	0.152	0.121
c_{010}	−0.882	0.422	0.956

We can prepare an entangled state of two junctions by bringing the first junction into resonance with the resonator for one *quarter* of a Rabi period [30], which, according to our RWA analysis, produces the state $(|100\rangle - |001\rangle)/\sqrt{2}$. After bringing the second junction into resonance for a half of a Rabi period, the state of the resonator and second junction are swapped, leaving the system in the state $(|100\rangle - |010\rangle)/\sqrt{2}$ with a probability of 0.987, where the resonator is in the ground state and the junctions are entangled. Using the cavity-QED analogy, it will be possible to transfer the methodology developed for the standard two-qubit operations, in particular controlled-NOT logic, to the electromechanical system, using mostly existing technology and demonstrated techniques.

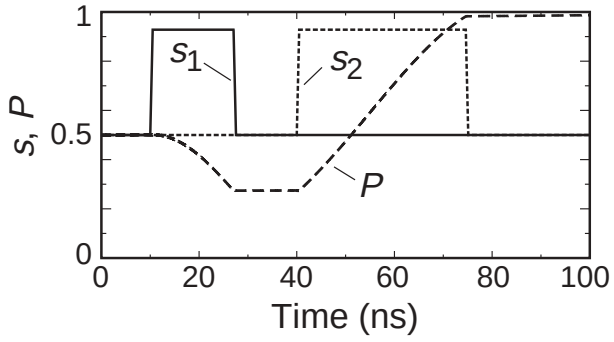

FIG. 5: Preparation of entangled Josephson junctions. The solid and dotted lines are $s_1(t)$ and $s_2(t)$, respectively, and the dashed curve indicates the probability for the system to be found in the state $(|100\rangle - |010\rangle)/\sqrt{2}$.

Acknowledgements. ANC and MRG were supported by the Research Corporation, and MRG was supported by the NSF under CAREER Grant No. DMR-0093217.

[1] Y. Makhlin, G. Schön, and A. Shnirman, Rev. Mod. Phys. **73**, 357 (2001).
[2] Y. Yu, S. Han, X. Chu, S.-I. Chu, and Z. Wang, Science **296**, 889 (2002).
[3] J. M. Martinis, S. Nam, J. Aumentado, and C. Urbina, Phys. Rev. Lett. **89**, 117901 (2002).
[4] A. J. Berkley, H. Xu, R. C. Ramos, M. A. Gubrud, F. W. Strauch, P. R. Johnson, J. R. Anderson, A. J. Dragt, C. J. Lobb, and F. C. Wellstood, Science **300**, 1548 (1998).
[5] Y. Nakamura, Y. Pashkin, and J. Tsai, Nature **398**, 786 (1999).
[6] Y. Nakamura, Y. Pashkin, and J. Tsai, Phys. Rev. Lett. **88**, 047901 (2002).
[7] D. Vion, A. Aassime, A. Cottet, P. Joyez, H. Pothier, C. Urbina, D. Esteve, and M. H. Devoret, Science **296**, 886 (2002).
[8] A. J. Leggett, Science **296**, 861 (2002).
[9] A. Shnirman, G. Schön, and Z. Hermon, Phys. Rev. Lett. **79**, 2371 (1997).
[10] Y. Makhlin, G. Schön, and A. Shnirman, Nature **398**, 305 (1999).
[11] J. E. Mooij, T. P. Orlando, L. S. Levitov, L. Tian, C. H. van der Wal, and S. Lloyd, Science **285**, 1036 (1999).
[12] Y. Makhlin, G. Schön, and A. Shnirman, J. Low. Temp. Phys. **118**, 751 (2000).
[13] J. Q. You, J. S. Tsai, and F. Nori, Phys. Rev. Lett. **89**, 197902 (2002).
[14] F. Plastina and G. Falci, Phys. Rev. B **67** (2002).
[15] A. Blais, A. M. van den Brink, and A. M. Zagoskin, Phys. Rev. Lett. **90**, 127901 (2003).
[16] A. Y. Smirnov and A. M. Zagoskin, cond-mat/0207214 (unpublished).
[17] O. Buisson and F. W. J. Hekking, in *Macroscopic Quantum Coherence and Quantum Computing*, edited by D. V. Averin, B. Ruggiero, and P. Silvestrini (Kluwer, New York, 2001), p. 137.
[18] F. Marquardt and C. Bruder, Phys. Rev. B **63**, 54514 (2001).
[19] A. D. Armour, M. P. Blencowe, and K. Schwab, Phys. Rev. Lett. **88**, 148301 (2002).
[20] J. Yang, T. Ono, and M. Esashi, Appl. Phys. Lett. **77**, 3860 (2000).
[21] A. Barone and G. Paterno, *Physics and Applications of the Josephson Effect* (Wiley, New York, 1982).
[22] T. A. Fulton and L. N. Dunkleberger, Phys. Rev. B **9**, 4760 (1974).
[23] R. Ruby and P. Merchant, IEEE Intl. Freq. Control Symposium p. 135 (1994).
[24] R. Ruby, P. Bradley, J. Larson, Y. Oshmyansky, and D. Figueredo, Technical Digest of the 2001 IEEE International Solid-State Circuits Conference pp. 120–121 (2001).
[25] A. N. Cleland, M. Pophristic, and I. Ferguson, Appl. Phys. Lett. **79**, 2070 (2001).
[26] AlN has a density $\rho = 3.26$ g/cm^3, piezoelectric modulus

$e_{33} = 1.46$ C/m^2, and dielectric constant $\epsilon = 10.7\ \epsilon_0$. The resonator has a geometric capacitance $C_{\rm res} = 0.59$ fF and a resonance frequency $\omega_0 = 10$ GHz.

[27] B. Auld, *Acoustic Fields and Waves in Solids* (Wiley and Sons, New York, 1990), 2nd ed.

[28] M. O. Scully and M. S. Zubairy, *Quantum Optics* (Cambridge University Press, Cambridge, 1997).

[29] X. Maître, E. Hagley, G. Nogues, C. Wunderlich, P. Goy, M. Brune, J. M. Raimond, and S. Haroche, Phys. Rev. Lett. **79**, 769 (1997).

[30] E. Hagley, X. Maitre, G. Nogues, C. Wunderlich, M. Brune, J. M. Raimond, and S. Haroche, Phys. Rev. Lett. **79**, 1 (1997).